

**Dry Extraction of Nickel from Mixed-Hydroxide Precipitates via Reduction and
Carbonylation**

by

Param Dave

A thesis

presented to the University of Waterloo

in fulfillment of the

thesis requirement for the degree of

Master of Applied Science

in

Chemical Engineering

Waterloo, Ontario, Canada, 2025

©Param Dave 2025

Author's Declaration

I hereby declare that I am the sole author of this thesis. This is a true copy of the thesis, including any required final revisions, as accepted by my examiners.

I understand that my thesis may be made electronically available to the public.

Abstract

The global transition towards electric vehicles (EVs) has prompted significant research into the sustainable and efficient production of battery-grade materials. Among the critical components of rechargeable batteries, nickel (Ni) is of particular importance due to its central role in cathode materials, specifically for Nickel Manganese Cobalt (NMC) and Nickel Cobalt Aluminum (NCA) batteries. Ni is conventionally extracted from primary sources such as laterite ores (containing 2-3% Ni by mass) through hydrometallurgy (with acid-intensive processing) or pyrometallurgy (with high-temperature, energy-intensive processing). Hydrometallurgical extraction produces an intermediate product called mixed-hydroxide precipitate (MHP), which can contain up to 50% Ni by mass on a dry basis, but still requires further processing to obtain high-purity nickel. This study explores an alternative, sustainable and selective extraction pathway for nickel from MHPs derived from laterite ores and spent battery materials (black mass). The explored vapour metallurgical approach is a two-step, dry process: 1) hydrogen reduction of nickel hydroxides with the MHP to metallic nickel at temperatures between 400°C to 500°C, and 2) selective nickel extraction via carbonylation and conditions of 100°C to 120°C and 150 psig to 450 psig. The carbonylation of metallic Ni using carbon monoxide (CO) produces a volatile molecule called nickel tetracarbonyl ($\text{Ni}(\text{CO})_4$), which selectively extracts Ni into the vapour phase. Rigorous safety protocols were employed in this research study to handle the toxic nature of the produced $\text{Ni}(\text{CO})_4$ molecules, including CO detectors to identify leaks, and an in-situ decomposition furnace downstream of the reactor to thermally decompose the carbonyls. Reduction and subsequent carbonylation experiments were conducted in a pressurized thermogravimetric analyzer (PTGA), allowing for real-time monitoring of mass changes associated with the reactions. Characterization techniques, including Fourier Transform Infrared (FTIR) spectroscopy, inductively coupled plasma–optical emission spectroscopy (ICP-OES), and Brunauer-Emmett-Teller (BET) analysis, were used to quantify Ni extraction, evaluate morphological changes from fresh samples to reaction residue, and confirm the formation of $\text{Ni}(\text{CO})_4$. Significant results demonstrated that the Ni extraction via carbonylation is strongly dependent on the precursor’s structural properties, specifically requiring high surface areas, adequate pore sizes, and minimal cobalt content to enhance transport of CO and $\text{Ni}(\text{CO})_4$. Optimal reduction conditions were identified at 450°C, producing residues with a balanced surface area and average pore size, favourable for the carbonylation reaction. Increased carbonylation pressure, at 450 psig, improved Ni extraction efficiency to 95% for a black mass-based MHP.

Acknowledgements

First and foremost, I would like to express my sincere gratitude to my academic supervisor, Dr. Eric Croiset, for his continuous support, insightful guidance and mentorship throughout my research. Your expertise and encouragement have been instrumental in the completion of this thesis.

I would like to extend my deep appreciation to my examining committee members, Dr. Aiping Yu and Dr. Maxime van Der Heijden, for dedicating their time and providing valuable insights that enriched this work.

Thank you to the Carbonyl Research Group at the University of Waterloo. In particular, I am thankful to Vahid Barahimi, who was the initial researcher to set up and optimize our flow system, provided essential day-to-day support during experiments, and guided me through various characterization techniques. Your dedicated efforts greatly facilitated my progress.

Special thanks to Dr. Vladimir Paserin, also a part of the Carbonyl Research Group, whose extensive knowledge and profound expertise in carbonyl chemistry consistently provided clarity, direction, and crucial technical insights into my studies.

I am thankful to Dr. Dmitri Terekhov for providing ongoing technical support and securing funding for our research group through the Mitacs Accelerate Program. I would also like to thank Westwin Elements for generously supplying various MHP samples used in this study.

To my colleagues at the University of Waterloo, Rithu, Joe, Mojtaba, and Fernando, thank you for creating a lively and supportive environment, especially during foosball matches.

I extend my deepest gratitude to my parents, Dimple and Ravin, for their unconditional support and encouragement throughout my academic journey.

Special recognition to my dog, Beedoo, whose boundless excitement has consistently brought me joy at the end of each day.

Lastly, a special thank you to my girlfriend, Naisu, for her unwavering support and patience during my research.

Table of Contents

| | |
|---|------|
| Author's Declaration | ii |
| Abstract..... | iii |
| Acknowledgements..... | iv |
| List of Figures..... | viii |
| List of Tables | xi |
| List of Abbreviations | xii |
| Chapter 1 Introduction..... | 1 |
| 1.1 Problem Statement and Motivation | 1 |
| 1.2 Project Objectives..... | 1 |
| 1.3 Thesis Outline..... | 2 |
| Chapter 2 Background and Literature Review | 3 |
| 2.1 Nickel Deposits and Production Landscape | 3 |
| 2.2 Processes for Nickel Extraction..... | 6 |
| 2.2.1 Extraction through Pyrometallurgy | 6 |
| 2.2.2 Extraction through Hydrometallurgy..... | 8 |
| 2.3 Significance of Mixed-Hydroxide Precipitates | 12 |
| 2.4 The Mond Process - Extractive Metallurgy..... | 16 |
| 2.5 Industrial Application of the Mond Process | 19 |
| 2.6 Reduction of Ni(OH) ₂ by Hydrogen..... | 23 |
| 2.6.1 Thermal decomposition of Ni(OH) ₂ to NiO | 23 |
| 2.6.2 Reduction of NiO to Metallic Ni | 24 |
| 2.6.3 Role of Oxygen Vacancies | 25 |
| 2.6.4 Kinetic Models and Mechanisms..... | 26 |

| | |
|--|----|
| 2.7 Carbonylation of Nickel | 31 |
| 2.7.1 Reaction Kinetics..... | 31 |
| 2.7.2 Mechanistic Models..... | 34 |
| Chapter 3 Experimental and Methodology..... | 37 |
| 3.1 Materials | 37 |
| 3.2 Sample Preparation..... | 39 |
| 3.3 Flow System Setup and Procedures..... | 39 |
| 3.3.1 Reduction Experiments..... | 43 |
| 3.3.2 Carbonylation Experiments | 44 |
| 3.4 Characterization Techniques and Data Analysis | 46 |
| 3.4.1 PTGA | 46 |
| 3.4.2 FTIR..... | 50 |
| 3.4.3 ICP | 52 |
| 3.4.4 BET..... | 53 |
| Chapter 4 Results and Discussion..... | 55 |
| 4.1 MHP Reduction | 55 |
| 4.1.1 Effect of MHP Reduction Temperature..... | 55 |
| 4.1.2 BET Surface Area and Pore Diameter Results for Reduction Residues..... | 59 |
| 4.1.3 Kinetic Modelling of MHP Reduction at Different Temperatures | 62 |
| 4.2 MHP Carbonylation..... | 67 |
| 4.2.1 Effect of MHP Reduction Temperature on Nickel Carbonylation | 67 |
| 4.2.2 Effect of Carbonylation Temperature | 69 |
| 4.2.3 Effect of Carbonylation Pressure..... | 70 |
| Chapter 5 Conclusions and Recommendations | 76 |

| | |
|--|----|
| 5.1 Conclusions..... | 76 |
| 5.2 Recommendations..... | 77 |
| Letters of Copyright Permission..... | 79 |
| References..... | 92 |
| Appendix A Raw Data and Sample Calculations..... | 98 |

List of Figures

| | |
|---|----|
| Figure 2-1: World mine production of nickel from 2013-2022. Reproduced with permission [3]. Copyright 2025, Natural Resources Canada..... | 3 |
| Figure 2-2: World distribution of significant sulfide and laterite nickel deposits. Reproduced with permission [4]. Copyright 2006, Elsevier..... | 4 |
| Figure 2-3: General laterite ore processing paths (CCD refers to counter-current decantation). Reproduced with permission [9]. Copyright 2011, Elsevier..... | 6 |
| Figure 2-4: General HPAL process for a laterite ore feed leached in sulfuric acid. Reproduced with permission [13]. Copyright 2011, Elsevier..... | 9 |
| Figure 2-5: Simplified process flow diagram of chloride-assisted sulfuric acid pressure oxidation, solvent extraction (SX) and electrowinning (EW) of nickel concentrate at Vale's Long Harbour operation. Reproduced under terms of the CC-BY license [18]. Copyright 2022, Taylor and Francis Group, LLC... | 11 |
| Figure 2-6: An MHP precipitation circuit from laterite ore undergoing heap leaching. Adapted from Willis, B., 2007 [22]. Unpublished..... | 14 |
| Figure 2-7: The 2023 Production and 2028 Target for Major Indonesian Nickel Companies [23]. | 15 |
| Figure 2-8: The atmospheric carbonylation process at the INCO, Clydach nickel refinery. Reproduced under terms of the CC-BY license [5]. Copyright 2015, UNSW Sydney..... | 20 |
| Figure 2-9: A 4-layer slab view of NiO surfaces before hydrogen introduction (left) and after (right) where nickel atoms are black spheres and oxygen atoms are grey. Reproduced with permission [45]. Copyright 2002, American Chemical Society. | 26 |
| Figure 2-10: SEM micrographs of: (a) feed Ni(OH) ₂ . (b) Partially converted PTGA product after 2-hour isothermal hold at 200°C. (c) Nearly fully converted PTGA product after 2-hour isothermal hold at 250°C. Reproduced with permission [40]. Copyright 2015, Elsevier. | 28 |
| Figure 2-11: Measured carbonylation of nickel at 80, 90, and 100°C and CO pressure up to 54 atm gauge pressure. Reproduced under terms of the CC-BY license [5]. Copyright 2015, UNSW Sydney. | 31 |

| | |
|---|----|
| Figure 2-12: Fitting of the modified first-order rate expression for nickel carbonyl formation to experimental data by Goldberger and Othmer to obtain nickel activity at 1 atm, 2 atm, and 4 atm. Reproduced with permission [51]. Copyright 1963, American Chemical Society. | 33 |
| Figure 2-13: A generic crystalline arrangement highlighting a) terrace, kink, and stepped edge sites and b) a Ni(211) surface, composed of (111) terrace sites and (100) stepped sites (right). Reproduced with permission [56]. Copyright 2021, Elsevier. | 35 |
| Figure 3-1: Flow diagram of the laboratory-scaled system within a fume hood, used for reduction and carbonylation experiments. | 42 |
| Figure 3-2: Typical temperature profile of reduction experiments. | 43 |
| Figure 3-3: Typical temperature profile of carbonylation experiments. | 44 |
| Figure 3-4: a) A reduction curve for B1-MHP at 450°C showing mass loss and temperature profile against time, and b) normalized fraction converted and temperature profile against time. | 47 |
| Figure 3-5: a) The carbonylation curve for B1-MHP at 110°C and 450 psig showing mass loss and temperature profile against time and b) Normalized Mass (%) for the same experiment against time. | 49 |
| Figure 3-6: Results of a) IR spectrum of pure CO gas at a pressure of 450 psig and a flow rate of 200 ml/min, b) IR spectrum of overlapping CO and Ni(CO) ₄ absorption bands during carbonylation production, and c) Saturated Ni(CO) ₄ peak at 2057 cm ⁻¹ wavenumber without overlap of CO absorption band when using a background spectrum with CO. | 51 |
| Figure 4-1: Fractional conversion during reduction under H ₂ atmosphere at 6 psig and temperatures of 400°C, 450°C, and 500°C of a) L1-MHP, b) L2-MHP, c) B1-MHP, and d) B2-MHP. | 56 |
| Figure 4-2: Kinetic model fitting to experimental reduction conversion for a) L1-MHP at 400°C, b) B1-MHP at 400°C, c) L1-MHP at 450°C, d) B1-MHP at 450°C, e) L1-MHP at 500°C, and f) B1-MHP at 500°C. | 64 |
| Figure 4-3: Normalized mass for carbonylation at conditions of 450 psig and 110°C for B1-MHP reduced at temperatures of 400°C, 450°C, and 500°C. | 67 |
| Figure 4-4: Normalized carbonylation mass at conditions of 450 psig, and varying temperatures of 100°C, 110°C, and 120°C for B1-MHP (reduced at 450°C). | 69 |

Figure 4-5: Normalized mass for carbonylation at conditions of 150 psig and 450 psig, 110°C (reduced at 450°C) for a) L1-MHP, b) L2-MHP, c) B1-MHP, and d) B2-MHP.71

Figure 4-6: Ni extraction efficiency (%) at carbonylation conditions of 450 psig, 110°C for the four MHP samples against the BET surface area of the respective sample after a 450°C reduction75

Figure A - 1: Mass profile during reduction under H₂ atmosphere at 6 psig and temperatures of 400°C, 450°C, and 500°C of a) L1-MHP, b) L2-MHP, c) B1-MHP, and d) B2-MHP.....98

List of Tables

| | |
|--|----|
| Table 2-1: A comparison of the commercial-scale carbonyl refining processes. | 22 |
| Table 3-1: Gases and reagents used in experiments. | 37 |
| Table 3-2: Samples used for reduction and carbonylation experiments. | 38 |
| Table 3-3: Composition of the MHP samples used in reduction and carbonylation tests (wt.%)..... | 39 |
| Table 3-4: Description and application of flowmeters within the system. | 41 |
| Table 3-5: Description and application of gas detectors within the system. | 41 |
| Table 3-6: Input parameters for the Varian 640-IR instrument software. | 52 |
| Table 3-7: Input parameters to the ASAP 2020 software during the degas and analysis steps. | 54 |
| Table 4-1: Mass loss fractions during the reduction of the four MHP samples at 400, 450, and 500°C. ... | 57 |
| Table 4-2: BET surface area and average pore diameter results for fresh MHP pellets and residues after reduction at 400, 450, 500°C. | 60 |
| Table 4-3: Ni and Co extraction efficiency from ICP analysis at carbonylation conditions of 150 psig and 450 psig, 110°C (reduced at 450°C) for L1-MHP, L2-MHP, B1-MHP, and B2-MHP. | 72 |

List of Abbreviations

| | |
|---------|--|
| AL | Atmospheric Leaching |
| BET | Brunauer-Emmett-Teller |
| BJH | Barrett-Joyner-Halenda |
| BPR | Back-Pressure Regulator |
| CCD | Counter-Current Decantation |
| DFT | Density Functional Theory |
| EDX | Energy-Dispersive X-ray |
| EV | Electric Vehicle |
| FC | Flow Controller |
| FG | Furnace Gas |
| FTIR | Fourier Transform Infrared |
| GD | Gas Detector |
| HPAL | High-Pressure Acid Leach |
| ICP-OES | Inductively Coupled Plasma - Optical Emission Spectroscopy |
| LPM | Liters Per Minute |
| MHP | Mixed-Hydroxide Precipitate |
| NCA | Nickel Cobalt Aluminum |
| NMC | Nickel Manganese Cobalt |
| PG | Purge Gas |
| PLS | Pregnant Leach Solution |
| PPB | Parts-Per-Billion |
| PTGA | Pressurized Thermogravimetric Analyzer |
| RG | Reaction Gas |
| SEM | Scanning Electron Microscopy |
| TLV | Threshold Limit Value |
| TRL | Technology Readiness Level |

Chapter 1

Introduction

1.1 Problem Statement and Motivation

The current shift towards EVs has increased the demand for critical materials used for rechargeable battery production. High-purity Ni is one of the critical metals used in cathode manufacturing, but it is also used for applications in specialized coatings, alloys, electronics, stainless steel manufacturing, and powder metallurgy. There lies a significant gap between global nickel demand and production capabilities, specifically for class 1 nickel (which is 99.8% pure). The expected demand for class 1 Ni is 6.4 million metric tonnes by 2040, but only 2.5 million metric tonnes were mined and produced in 2020 [1]. This gap is projected to continue growing, along with the requirement for a sustainable process to extract and refine nickel from primary (such as deposits) and secondary sources (such as MHPs). Conventionally, Ni is sourced from primary deposits (either laterite ores or sulfidic ores) through hydrometallurgical or pyrometallurgical processing. Hydrometallurgy involves the usage of high volumes of concentrated acid for leaching purposes, generating excessive liquid waste, which can be expensive to dispose of and poses many environmental concerns. On the other hand, pyrometallurgy unit operations are energy-intensive due to high temperature requirements for reactions such as roasting, calcination, and smelting. This highlights an evident technology gap; there is a need for further research into the dry-processing capabilities of selectively extracting Ni while avoiding the environmental and economic concerns related to conventional technologies. The carbonylation of Ni involves the selective vapour-phase extraction of solid Ni into volatile $\text{Ni}(\text{CO})_4$. This method has already been successfully implemented on a commercial scale by various companies globally. However, there is limited academic literature focusing on Ni extraction from MHPs via carbonylation. A few studies have explored the carbonylation of laterite ores, but less attention has been given to secondary source materials (such as black mass) and MHPs.

1.2 Project Objectives

This research study aims to explore and maximize nickel extraction from MHPs in a PTGA through the hydrogen reduction of the metallic hydroxides and the carbonylation of nickel through reaction with CO. The specific objectives are:

1. To analyze how varying the temperature during the reduction reaction influences nickel hydroxide conversion, reaction kinetics, structural characteristics of the reduced samples, and the subsequent carbonylation reaction.

2. Investigate the impact of carbonylation parameters, including the carbon monoxide pressure and temperature, on reaction kinetics and overall Ni extraction.
3. To assess how different MHP feedstock sources (i.e. laterite-based MHP and black mass-based MHP) and their distinct chemical composition and morphologies impact Ni extraction.

1.3 Thesis Outline

Chapter 1: Introduction

Establishes the broader context of Ni extraction, outlines the main motivation for this project, and identifies the gap in academic research and industry regarding the proposed technology.

Chapter 2: Literature Review

Provides an in-depth review of the conventional processes for nickel extraction, and the significance of MHPs within the context of metallurgy, introduces the reactions associated with the Mond process (which is the basis for vapour metallurgical reactions), and examines prior research studies focusing on the kinetics and mechanisms of the reduction of nickel hydroxides, and carbonylation of nickel.

Chapter 3: Experimental and Methodology

Provides a detailed outline of the flow system used for experiments, centered around a PTGA. Provides a background on the characterization techniques used, including PTGA, ICP-OES, BET surface area analysis, and FTIR spectroscopy.

Chapter 4: Results and Discussion

Presents and analyzes the experimental results of the effect of reduction temperature, carbonylation temperature, and carbonylation pressure on the structural changes of the samples, overall Ni extraction, and kinetics of the reactions.

Chapter 5: Conclusions and Recommendations

Summarizes the key findings of the research study, relates the findings back to the project objectives, and highlights the research limitations. Provides recommendations for future investigation into Ni extraction, regarding further experimental plans and potential for process scale-up.

Chapter 2

Background and Literature Review

2.1 Nickel Deposits and Production Landscape

Metallic nickel is a versatile material with numerous research and development and industrial use cases. With its addition to alloys, nickel can produce compounds with consistent properties across a wide temperature range such as hardness, strength, and corrosion resistance [2]. The metallic nickel market has a wide variety of products and applications and as a result, there is a demand for nickel at different chemical purities. Class I nickel products are greater than 99.8% pure, and examples of such include electrolytic cathodes, carbonyl-refined powder, pellets, and foam [2]. Class II products are less than 99.8% pure and are mainly used in steel manufacturing and include ferronickel and nickel oxide.

The global mined nickel production in 2022 was 3.3 million tonnes, showing an increase of 20% from 2021. Indonesia was the leading producer, at 1.6 million tonnes, followed by the Philippines at 0.33 million tonnes, Russia at 0.22 million tonnes, New Caledonia at 0.19 million tonnes, Australia at 0.16 million tonnes, and Canada at 0.14 million tonnes [3]. Since 2017, there has been a general increasing trend of global mined nickel production, as seen by Figure 2-1 [3].

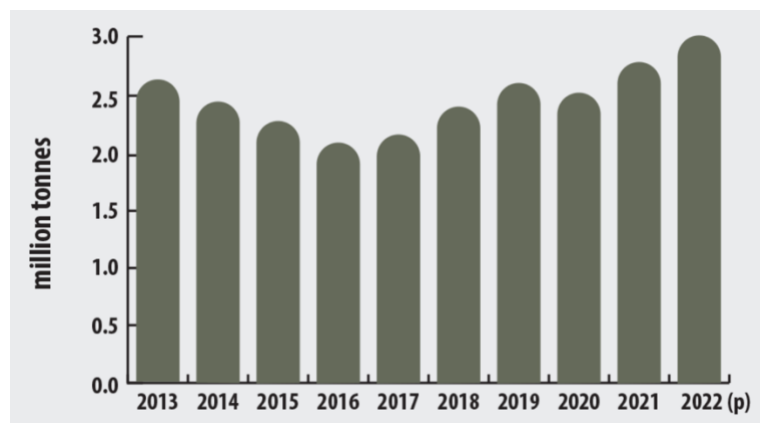


Figure 2-1: World mine production of nickel from 2013-2022. Reproduced with permission [3].

Copyright 2025, Natural Resources Canada.

According to the US. Geological Survey, the current global nickel resources are estimated to be 300 million tonnes, of which 60% are lateritic deposits and 40% are magmatic sulfide deposits [3]. These reserves are heavily concentrated in the countries that lead in nickel production, with Indonesia and Australia each

representing 21% of the total reserves, followed by Brazil at 16% [3]. Canada represents 2% of the global reserves and ranks seventh.

Nickel is primarily extracted from two types of ore: sulfidic and lateritic ores. Sulfidic ores come in various forms, a few being Pentlandite ($(\text{Ni,Fe})_9\text{S}_8$), Millerite (NiS), and Heazlewoodite (Ni_3S_2). These ores are formed through magmatic processes wherein molten rock cools and segregates into the lower parts of the magma chambers. Nickel sulfide deposits are found across most of the continents, but the major ones lie in Russia, Australia, Canada and southern Africa, as shown in Figure 2-2 [4]. Sulfide ores are concentrated first through flotation, gravity or magnetic separation and then smelted in a furnace to produce nickel matte and further refined through a hydrometallurgical or pyrometallurgical processing route [5]. Sulfide ores contain 1-2% Ni along with copper, cobalt, and iron sulfides. The metal extraction processes, including physical beneficiations, are able to produce high-grade concentrates. The refining processes are more mature and have higher technology readiness levels (TRLs). Concentrated sulfides after metallurgical processing can contain anywhere between 6-20 % Cu-Ni alloys [6].

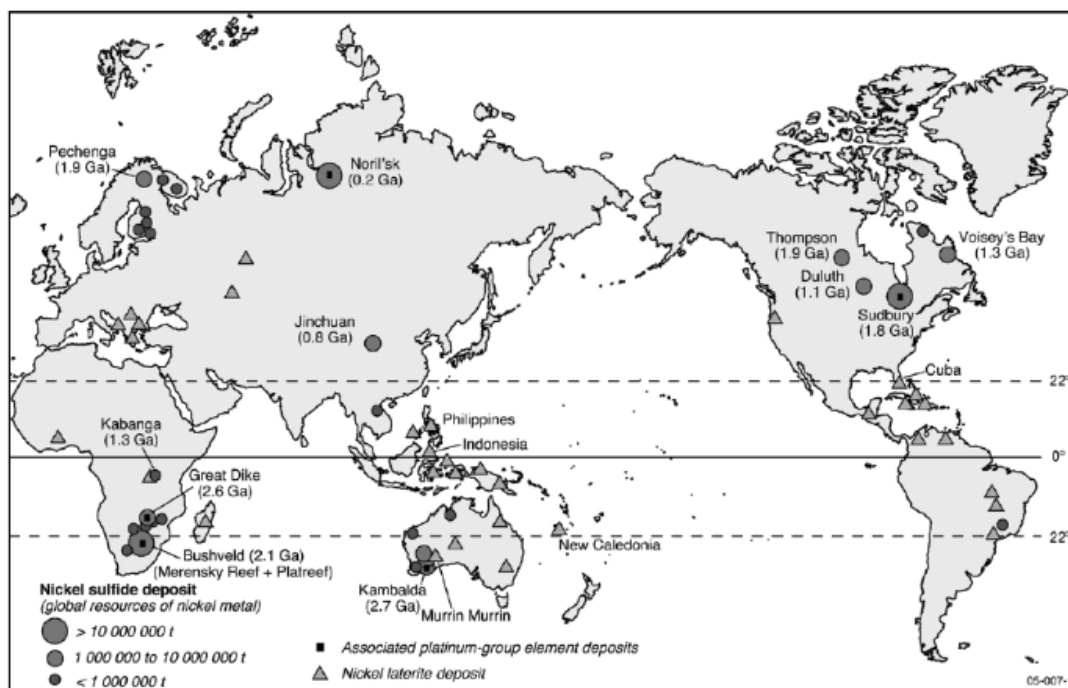


Figure 2-2: World distribution of significant sulfide and laterite nickel deposits. Reproduced with permission [4]. Copyright 2006, Elsevier.

The formation of laterite ores occurs through the weathering of ultramafic rocks (igneous, metamorphic rocks defined by their low silica, high iron and magnesium content). The mineralogy of the laterites is dependent on the location, climate and depth of the deposit. Nickel oxide is the main source of the metal within laterites, and the concentration of nickel ranges from 1-3% in the crude material, along with some cobalt and 30-45% moisture in the form of bonded hydroxides [6]. Nickel-containing laterites are divided into limonites and saprolites. Limonites are surface-level oxidized deposits, abundant in iron oxides and hydroxides (with >1.5% nickel content) and conventionally require high-pressure acid leaching (HPAL) hydrometallurgical processing to extract nickel [5]. Saprolites are found in the lower layers of laterite deposits, inherently more difficult to mine than the surface layer material, but contain up to 3% nickel content [5]. The extraction of nickel from saprolites is conventionally achieved through pyrometallurgical processes, such as smelting. The major sites for laterite deposits are in Australia, Cuba, Indonesia, New Caledonia and the Philippines [7]. Li et al. [8] reported in 2010 that the nickel proportion extracted from laterite ores has increased from 15% to 50% from 1950 to 2010. Since sulfide ores are not as easily mined as laterites, and considering the depletion of sulfide deposits, the extraction of nickel from laterites and laterite ore concentrates such as mixed hydroxide precipitates becomes of high importance.

2.2 Processes for Nickel Extraction

In the industry, there are various routes for nickel extraction from laterite and sulfide ores. The conventional methods include hydrometallurgical processes, pyrometallurgical processes and ones based on the Caron process. The type of processing route and conditions are dependent on the ore type and composition. Even between extraction from limonites and saprolites, the extraction technologies vary based on the composition of the components of interest (i.e. Ni, Co, Fe, MgO, Cr₂O₃). A study from Norgate et al. [9] presents high-level processes for three different extraction methods from a feed source of saprolite and limonite ore, as seen in Figure 2-3.

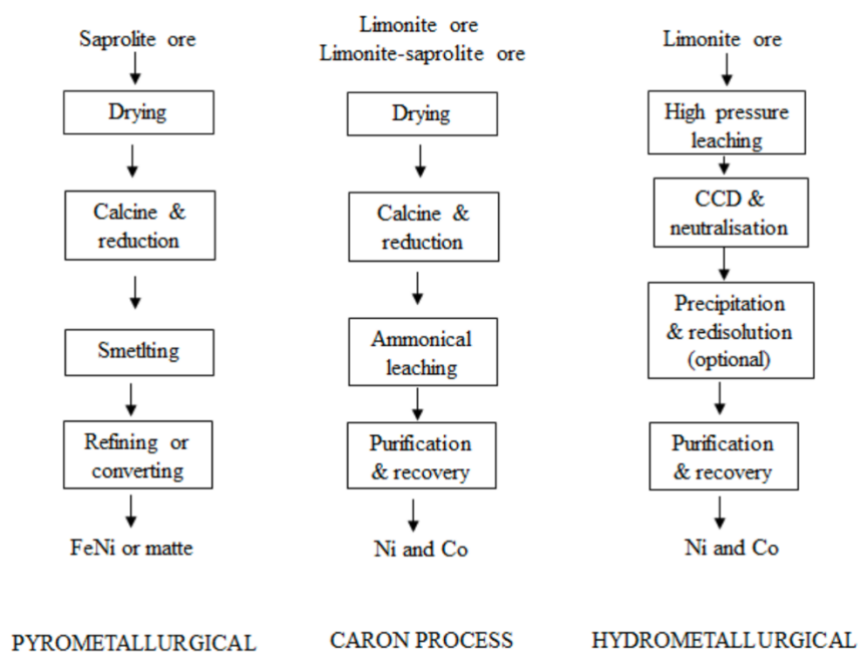


Figure 2-3: General laterite ore processing paths (CCD refers to counter-current decantation).

Reproduced with permission [9]. Copyright 2011, Elsevier.

2.2.1 Extraction through Pyrometallurgy

Pyrometallurgy involves high-temperature processes such as drying, calcination/reduction, roasting, and smelting to extract and refine valuable metals from deposited material [6]. The intermediate products of most pyrometallurgical processes involving nickel are ferronickel metal (Fe-Ni), or a nickel sulfide matte, which are intermediate products of the extraction and not fully refined, pure products.

The first step in the pyrometallurgical processing of laterites is drying, where all the water content is removed. The dried material is then calcined (high-temperature heating below the melting point of the ore in the absence of air) in a rotary kiln. This step is necessary for the removal of chemically bound water and decomposition of carbonates, hydroxides and sulfates into oxides. During the next phase of smelting, the calcined ore is further reduced to form metallic nickel or ferronickel. A fluxing material is introduced at temperatures of approximately 1600°C, which combines with impurities within the ore (generally silica and magnesia) to form a slag [10]. This slag then has to be physically separated and recycled back [6]. After final converting and refining steps, ferronickel alloy or nickel matte is produced. In a process of this type, each unit process is very energy-intensive because of the high temperature requirements of calcination, smelting and slag formation, calling for high usage of hydrocarbon fuels and electric power [6].

Since nickel production from oxide ores through pyrometallurgy consumes two to three times as much energy as production from sulfide ores, pyrometallurgy is more suited for the latter feed source [6]. The sulfide ores are first crushed and then often refined through froth flotation or magnetic separation to produce a nickel sulfide concentrate ([5], [6]). The concentrate is roasted in the presence of air to oxidize iron and sulfur selectively. Nickel sulfide in the presence of excess oxygen is converted to nickel oxide and sulfur dioxide gas. Iron oxides are fluxed through reaction with silica, and the resulting slag also removes any non-sulfide gangue in the concentrate [11]. The roasted ore is sent to a smelting operation to reduce the nickel oxides and produce a nickel matte. The composition of this molten nickel sulfide phase (matte) ranges from 15-40% Ni, 20-40% Fe, 20-25% S, Cu, Co and platinum group metals [12]. In a rotary converter process, air or pure oxygen is blown from the top, through the molten matte, to oxidize the remaining iron and sulfur. The iron oxides are removed from the matte in the form of slag once again, and the converted matte contains 40-70% Ni, 0.5-4% Fe, 21-24% S, and small quantities of Cu and Co [12]. Although the pyrometallurgical processing of sulfide ores requires substantially less energy than laterites, several drawbacks follow. The main challenge that must be addressed is capturing and fixing sulfur dioxide (SO₂) gas released during the roasting step. There is high capital cost associated with capturing SO₂ gas and converting it to sulfuric acid (which proves to be an easier storage method for sulfur). Without coupling off-gas treatment via acid plants, the release of SO₂ in the atmosphere would pose many environmental concerns. Furthermore, excess sulfur present in the roasted ore degrades the nickel matte; to control the sulfur concentration, it becomes important to separate the iron sulfides before the pyrometallurgical stages [6].

2.2.2 Extraction through Hydrometallurgy

With increasing energy costs, hydrometallurgical processes pose a more practical and economical alternative to pyrometallurgy, specifically for extracting nickel from lateritic ores containing 0.95-1% nickel. Since oxide ores can contain up to 50% moisture, components with significantly high melting points, and higher iron content, pyrometallurgical processing routes would require high energy consumption and may not be feasible from an economic standpoint. Additionally, performing pyrometallurgical techniques on nickeliferous laterites presents challenges in slag melting and inadequate metal-slag separation and poses environmental concerns related to SO₂ emissions [6]. Through laterite hydrometallurgy, 100,000 tonnes per year of high-purity nickel was produced (as of 2011), making it more dominant than extraction from sulfide ores through pyrometallurgy [13]. However, similar extraction principles are used in the industry for the extraction of nickel from both feed sources. Common hydrometallurgical processes include atmospheric leaching and high-pressure acid leaching with sulfuric acid, hydrochloric acid, or nitric acid. Processes involving a combination of hydrometallurgy and pyrometallurgy treatments are also employed in the industry, posing more economical routes.

2.2.2.1 High-Pressure Acid Leaching

Among the hydrometallurgical processes for laterites, HPAL is emerging as the most effective technology for extracting nickel and cobalt. Sulfuric acid is used to leach Ni and Co at temperatures and pressures ranging from 240°C-270°C and 20-40 atm, respectively, in an autoclave. Under these high-temperature and pressure conditions, the leaching process achieves greater than 95% recovery of nickel within 30 to 120 minutes, as the rate of chemical reactions is accelerated. In an acidic solution with a pH ranging from 2 to 3 and temperatures beyond 200°C, iron precipitates out of the solution, thereby allowing nickel to be isolated and extracted without ferric impurities ([14], [15]). The main leaching reactions of nickel oxide are shown in Equation 2-1 and Equation 2-2. The protons in these equations are present in the solution from the dissociation of sulfuric acid.



After the laterite ore is leached, the slurry is cooled to approximately 100°C across several flash tanks and then enters a counter-current decantation circuit. In this circuit, washing water is introduced and solid/liquid separation occurs. Impurities, including Al, Cr, Cu, Fe, Mg, Mn, and Zn, are removed by a neutralization stage (the pH is adjusted accordingly to precipitate these metals out of solution while keeping Ni in the aqueous phase) in the presence of H₂S gas. Nickel and cobalt are then precipitated out of the solution by adjusting the pH level to 3, yielding a nickel-cobalt sulfide precipitate that is 55% Ni, 5% Co, 40% S. The precipitate is then sent to a downstream refinery to yield pure Ni and Co. This flowsheet is depicted in Figure 2-4 [13].

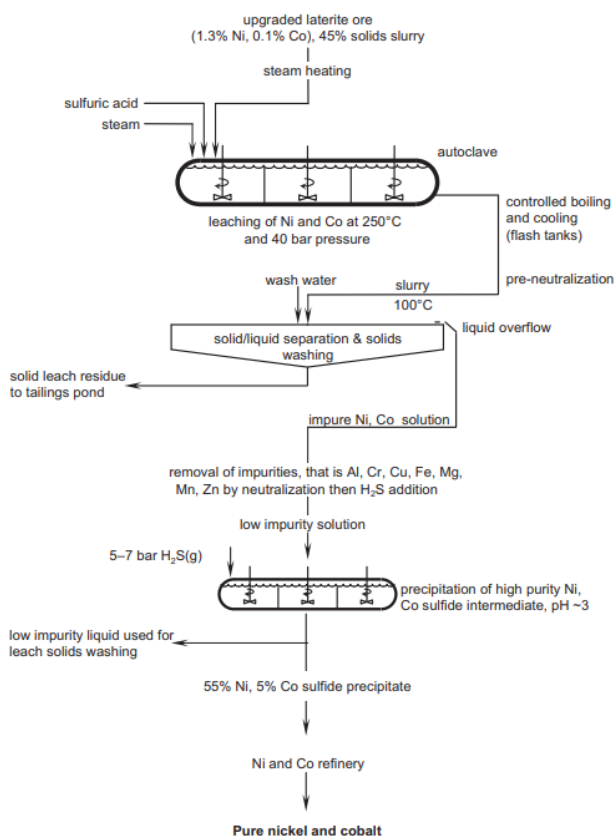
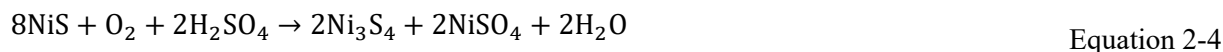
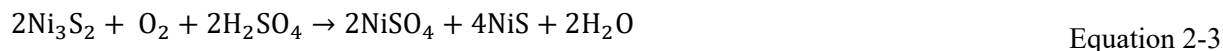


Figure 2-4: General HPAL process for a laterite ore feed leached in sulfuric acid. Reproduced with permission [13]. Copyright 2011, Elsevier.

The first commercial-scale HPAL plant was commissioned in 1959 in Moa Bay, Cuba and is still currently in operation. It operates between 245°C-270°C and pressures up to 200 atm to achieve 99.7% Ni recovery [5]. In the Philippines, limonite ore is leached in sulfuric acid for 30 minutes, and the recovery is 97.5%. The first disadvantage of the HPAL process is the high capital costs associated with the specialized

equipment needed for high-temperature and high-pressure operation. The capital costs of titanium-lined autoclaves and flash tanks, along with regular maintenance to prevent corrosion and abrasive effects of concentrated acid at high temperatures, could render this process as economically unfeasible [6]. The second disadvantage of this process is the high acid consumption, ranging from 350-500 kg per tonne of ore processed [16].

Although HPAL is a technology used in the industry for laterite ore processing, similar processes have been employed for sulfide ores. Vale's chloride-assisted sulfuric acid pressure oxidation facility in Long Harbour, Canada, is a facility that leaches nickel sulphide concentrate to produce pure nickel metal. However, it is important to note that the concentrates fed into the sulfuric acid pressure oxidation process are beneficiated through pyrometallurgical steps prior. The main reactions for nickel sulfide leaching are shown in Equation 2-3 and Equation 2-4. Oxygen oxidizes sulfur to sulfate, and sulfuric acid is used as the leaching agent. The conditions can be controlled to maximize the leaching rate of Ni and Co to 85% while inhibiting the leaching of Cu and other heavy metals [17]. Equation 2-3 shows the partial leaching of Ni_3S_2 , where NiSO_4 is the soluble form of nickel and remains in solution for later recovery. NiS remains as a solid residue in the leach and has to undergo further leaching, as shown in Equation 2-4. In the second reaction, the desired NiSO_4 is also produced, but a more complex nickel sulfide in the form of Ni_3S_4 would require further leaching and oxidation steps for full recovery.



The block flow diagram of Vale's Long Harbour process is presented below in Figure 2-5 [18].

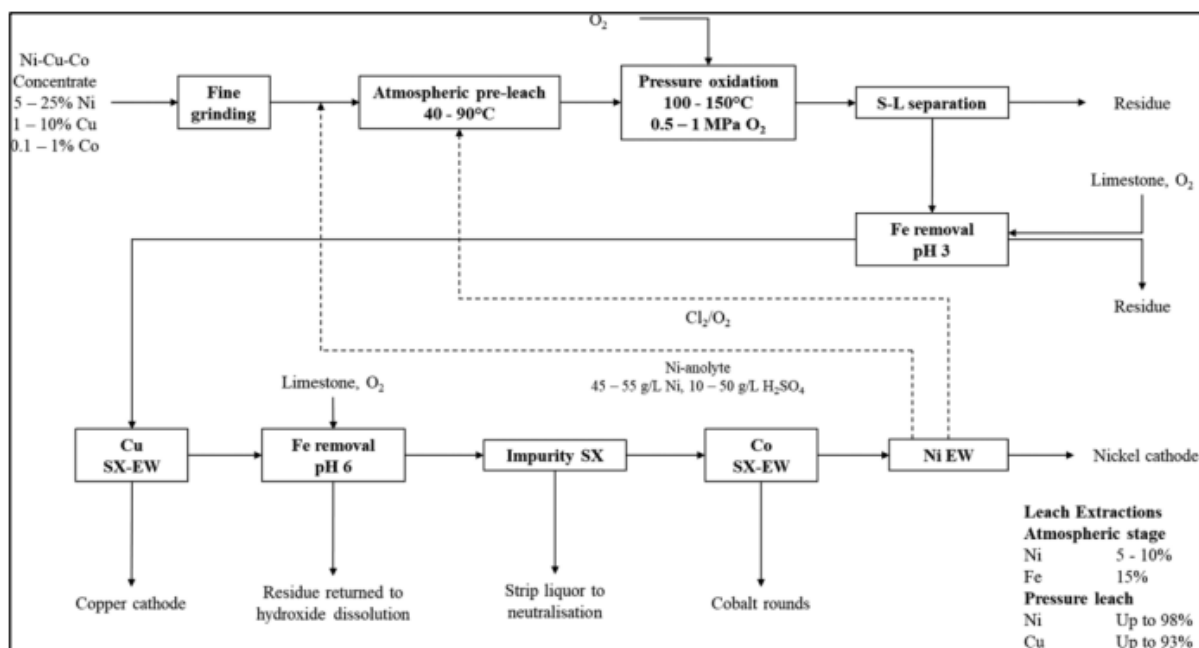


Figure 2-5: Simplified process flow diagram of chloride-assisted sulfuric acid pressure oxidation, solvent extraction (SX) and electrowinning (EW) of nickel concentrate at Vale's Long Harbour operation. Reproduced under terms of the CC-BY license [18]. Copyright 2022, Taylor and Francis Group, LLC.

2.2.2.2 Atmospheric Leaching/Heap Leaching

Atmospheric leaching (AL) is an alternative to HPAL that is conducted at low temperatures and requires only open vessels or heaps. It is a low-energy consumption, simple process that avoids the need for expensive equipment like autoclaves and flash units. Two main types of AL include heap leaching and agitation leaching, all of which are accomplished by acid contact (organic or inorganic) at atmospheric pressure and temperatures up to 105°C [6].

Heap leaching is a very flexible process that can be applied to a variety of laterite deposits. Raw ore is stacked into heaps, typically 4 to 5 meters in height. A leaching solution containing diluted sulfuric acid is applied to the top of the heap, allowing it to percolate downwards through the ore. As the solution moves through the heap, the desired metals are leached into the aqueous phase. The effluent, known as the pregnant leach solution (PLS), is gathered in a pond located at the base of the heap. Acid and water are then replenished in the pond as needed to maintain the leaching process [6]. Factors that can affect the

performance of the leaching include the granulometric and mineralogical composition of the ore, the concentration of the solvent, and the duration of leaching. Studies on heap sulfuric acid leaching have shown that up to 85% Ni recovery is possible and is achieved within a 40-day period with iron concentration in the solvent less than 5%. Sulfuric acid is consumed at a rate of 10 to 25 kg per kg of Ni recovered. However, as mentioned earlier, depending on the conditions of the leaching and type of ore, this process could take several months at ambient temperatures to achieve Ni recoveries comparable to HPAL [16].

Agitation leaching occurs in stirred tank reactors, and it is often used for low-grade nickel laterite ores (less than 1.5% Ni content by mass). The ore is crushed into a fine powder to increase surface area, and it then disperses into a leaching solution containing sulfuric acid through mechanical agitation. A patent has found that limonite and saprolite slurries should contain 25-30% solids for optimal leach rates [19]. The operating temperature of around 100°C and a 2 M sulfuric acid solvent allow the Ni leaching process to achieve greater than 90% recovery within 12 hours. The tradeoff of this process, as compared to HPAL, is the higher acid consumption, at 500-700 kg per tonne of ore processed [16].

2.3 Significance of Mixed-Hydroxide Precipitates

As per a commercially funded study, approximately 200,000 tonnes of nickel was used in the manufacturing of battery precursors in 2020, with an expectation (at that time) to reach 300,000 tonnes by the following year. The expected amount was already close to the amount of class I nickel, in the form of powder and briquettes, that was available in the market [20]. With the rapid growth of electric vehicles and demand for nickel-rich batteries, and depletion of high-grade sulfide ores, there has been a shift towards hydrometallurgical processing of laterites that efficiently produce MHPs. MHPs are quickly becoming one of the primary precursors supplying nickel to the battery sector; technological advancements in HPAL plants, particularly in Indonesia, Australia, and Turkey, are enabling large-scale MHP production, which is generally more cost and energy-efficient in comparison to traditional refining methods.

Direct nickel extraction through the hydrometallurgical route generally involves HPAL or atmospheric leaching of laterite ores, followed by a cooling step, then a counter-current decantation process, washing stage and then precipitation to yield and nickel-cobalt-sulfide precipitate. This product is then sent to a downstream nickel or cobalt refinery for further treatment to yield class 1 nickel. In other cases, the leaching step is followed by solvent extraction and ion exchange to produce nickel sulfate (NiSO₄), a common precursor in battery electrode materials. MHP is an intermediate product of the hydrometallurgical processing of laterite ores. After the laterite ores undergo HPAL to extract nickel and cobalt into an aqueous

solution containing soluble heavy metal ions, called a pregnant leach solution (PLS), an alkaline reagent is used to increase the pH level of solution. This reduces the solubility of the metallic ions and causes a precipitate to form. Examples of alkaline reagents include caustic soda (NaOH), soda ash (Na₂CO₃), hydrated or slaked lime (Ca(OH)₂), magnesium hydroxide (Mg(OH)₂) and magnesia (MgO), the latter being most often used to selectively precipitate nickel and cobalt [6]. MHPs can be contaminated with manganese and unreacted MgO, which then calls for extra stages of precipitation in a circuit to yield precipitate containing up to 40% nickel by mass on a dry basis. The precipitate is then filtered and dried. The precipitation of Ni, Co and Mn (after being leached by sulfuric acid) in PLS to form MHP occur through the following chemical reactions [21].

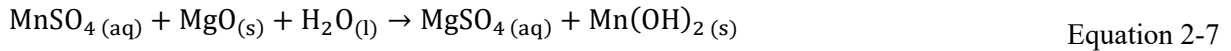
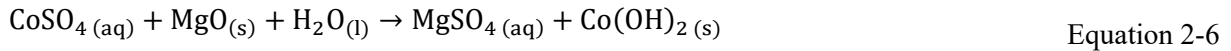
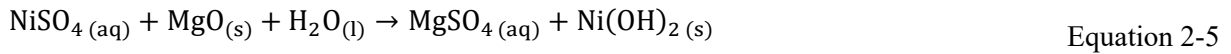


Figure 2-6 shows a typical process of MHP production from a laterite ore feed source [22]. It is important to note here that a heap leaching stage is presented in this flowsheet, which is different than a flowsheet for MHP production from HPAL. Nickeliferous laterites contain anywhere from 10% to 50% iron content by mass, and 20-50% of this content is dissolved into PLS from an atmospheric or heap leach. As a result, the concentration of iron in PLS from heap leaching ranges from 15-30 g/L compared to less than 8 g/L from HPAL [22]. The recycle leach and two iron removal stages in Figure 2-6 also help maintain the feed solution that is optimal for the following two mixed hydroxide precipitates (in which Ni and Co are the desired precipitates). As pH levels gradually increase with the addition of magnesia, Ni²⁺ and Co²⁺ precipitate first and then Mn²⁺ and Mg²⁺ [6].

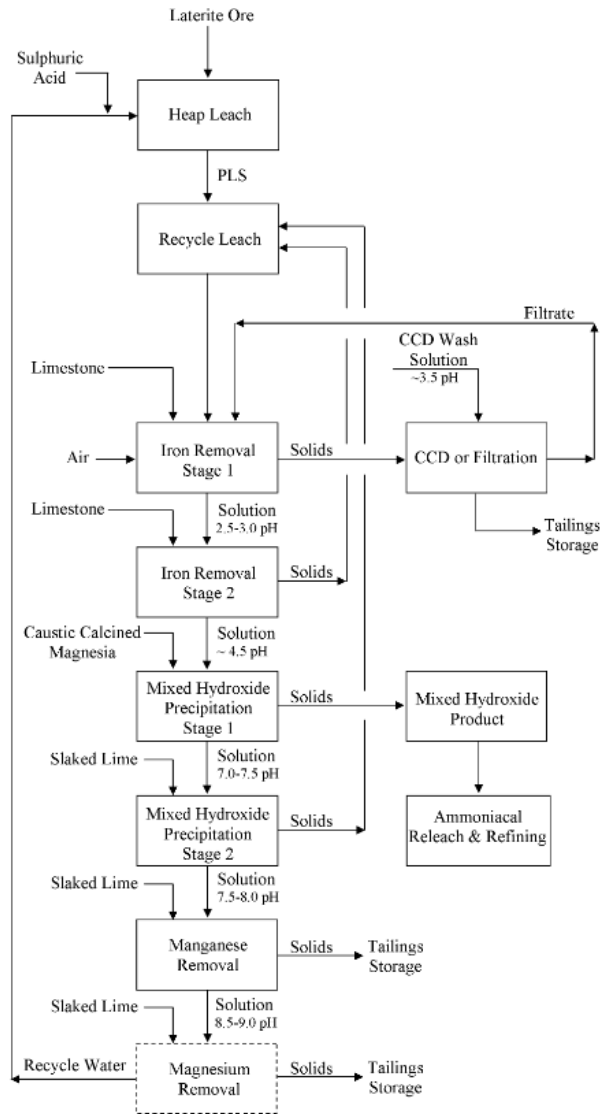


Figure 2-6: An MHP precipitation circuit from laterite ore undergoing heap leaching. Adapted from Willis, B., 2007 [22]. Unpublished.

MHP is quickly transitioning from just an intermediate product to the product of choice, as it is starting to replace $\text{Ni}(\text{SO})_4$ as battery precursor material. Additionally, it behaves similarly to nickel briquettes and laterites, allowing interchangeable processing infrastructure [20]. Indonesia is currently the leading nickel producer globally, accounting for 42% of global nickel reserves and 51% of nickel mine production. Within the country, four publicly traded companies – PT Aneka Tambang (Antam), Mederka Battery Materials (MBMA), Trimegah Bangun Persada (TBP) and PT Vale Indonesia (Vale) produced 353,000 tonnes of

nickel in 2023. From these four, MBMA, TBP and Vale are ramping up production of MHP vastly and are targeting approximately a 750% increase in production in 2028 as compared to 2025, also shown in Figure 2-7 [23]. Goro (owned by Prony Resources) is changing focus to MHP production as well as Blackstone Minerals (based in Australia) which owns a nickel sulfide mine in Vietnam and Giga Metals (based in Canada) [20].

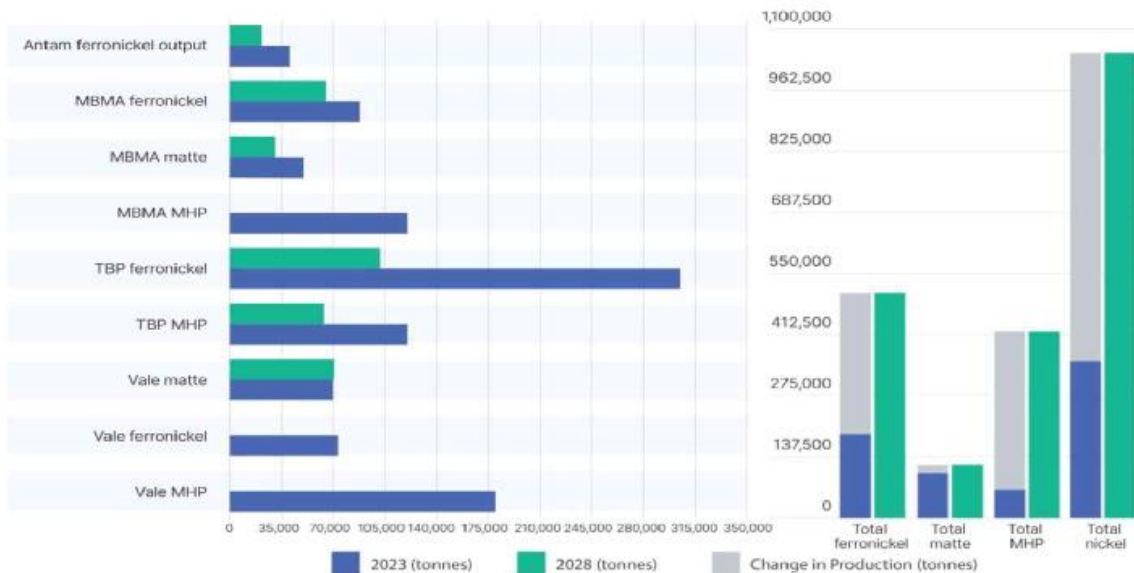


Figure 2-7: The 2023 Production and 2028 Target for Major Indonesian Nickel Companies [23].

With the growing MHP production on a global scale, the refining and extraction processes from this intermediate form into plating grade nickel sulfates, metals used in stainless steel and alloys and high purity metals (class I and II) for specialty applications and battery materials become very desirable. When considering hydrometallurgical processes for extracting and refining nickel from MHPs, there are several significant challenges. These complex processes are sensitive to the feed material's composition and necessitate meticulous waste stream management.

A study [24] proposed a method for selective leaching of nickel from a mixed nickel-cobalt hydroxide precipitate using acid leaching; by applying a preferential oxidation step, Ni is dissolved into the PLS, whereas Co and Mn stay intact in a stable solid form. The study concluded that the effect of temperature and aging of MHP was negligible on metal extraction rates and leaching kinetics, but impurities like Ca and Mg within the MHP called for the need for further selected leaching processes to achieve a high-purity Ni extraction [24]. Another study [25] proposed direct solvent extraction (DSX) techniques to remove Mn

and other smaller impurities in MHP. They concluded that complete Mn removal is achieved in two extraction stages, where co-extracted Ni and Co can be scrubbed out using a mild sulfuric acid solution [25]. This highlights that refining processes must be fine-tuned to feed MHP composition and require the usage of acids and waste management for slurries. A third study explored the dissolution of nickel-cobalt hydroxide precipitate using various organic acids, including citric ($C_6H_8O_7$), oxalic ($C_2H_2O_4$), and malic ($C_4H_6O_5$) acid. Citric acid emerged as the most effective, achieving dissolution rates of 91.2% for Ni, 86.8% for Co, and 90.8% for Mn. However, the study concluded that the use of oxidants, namely potassium permanganate ($KMnO_4$) and hydrogen peroxide (H_2O_2), were unsuccessful in achieving selective dissolution in an organic acid environment. This was not the case with a sulfuric acid environment. The study also mentions that the leaching rate is characterized by a shrinking core model, and kinetics are highly dependent on acid type, acid concentration, leaching time, temperature, and specific solid-to-liquid ratios [26].

2.4 The Mond Process - Extractive Metallurgy

The Mond Process, also referred to as the Carbonyl Process, is a significant metallurgical technique that was developed in the late 19th century for the extraction and purification of nickel and iron. The process, discovered by Ludwig Mond in 1890, utilizes the unique and selective property of nickel to form a volatile carbonyl molecule when reacting with CO in a metallic state. This innovation facilitates the extraction of nickel from a variety of feed sources and the production of high-purity powders, coatings, foams and pellets. He was granted a patent for this process in 1890, and since then, the Mond Process has been commercialized, particularly by the International Nickel Company in Sudbury, ON (one of the largest deposits of nickel worldwide) [27].

Ludwig Mond accidentally synthesized nickel carbonyl while working on apparatus for the Solvay process. He was experiencing high maintenance costs of the magnesia plant he was experimenting with, due to the corrosion of nickel valves, leading to the formation of a black crust on the surface. Along with his assistant Carl Langer, Mond found that there were trace quantities of carbon monoxide gas in the nitrogen used for flushing operations. After the investigation, the two found that the reaction between the nickel on the valves and carbon monoxide formed a volatile carbonyl. Furthermore, nickel was the only metal to form a carbonyl at atmospheric pressure and the carbonyl decomposed at slightly elevated temperatures to metallic nickel and liberated carbon monoxide gas. This reaction mechanism opened possibilities to selectively extract

nickel from ores, leaving all other metallic oxides intact in solid form, and yielding pure nickel at a cheaper cost than through electrolysis [28].

The Mond Process consists of three subsequent reactions. Although reaction conditions have been altered and optimized for various commercial applications since the research work by Mond and Langer, chemistry remains the same.

1. Reduction of Nickel Oxide:

Nickel oxide is reduced with hydrogen gas (introduced either as pure gas often as synthesis gas, which is a mixture of hydrogen and carbon monoxide) at temperatures ranging from 175°C to 900°C through a first order reaction [29]. The products are metallic nickel and water. In Mond's work, nickel oxide was reduced in powder form by passing pure hydrogen gas over the solid sample at 400°C [30].



2. Carbonylation:

Metallic nickel reacts with CO gas at atmospheric pressure (though studies and commercial operations have also been conducted at higher pressure, resulting in favourable kinetics) and temperature ranges from 50°C to 115°C [31]. This is a readily reversible reaction, with the product of the forward reaction being gaseous nickel tetracarbonyl.



3. Thermal Decomposition:

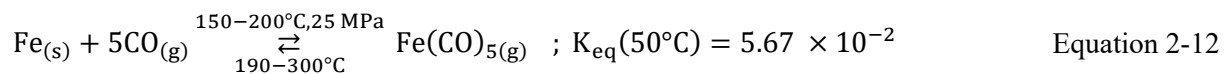
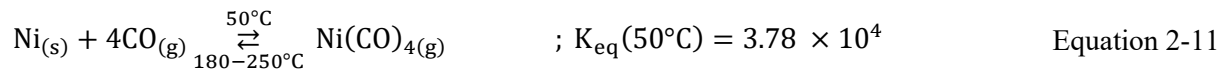
When nickel carbonyl is heated to 175°C, the equilibrium shifts, and pure nickel is deposited while CO is liberated in the gas phase. Studies have shown that this decomposition reaction is chemically controlled below 175°C and occurs through heterogeneous nucleation in the temperature range of 248°C and 305°C [31]. The decomposition process can be optimized to deposit nickel powder or nickel onto substrates as per market demands. The CO can then be recycled back to the carbonylation step, after the needed purification steps, to minimize operational costs and waste.



The Mond Process was a revolutionary discovery allowing for the effective extraction of pure nickel, but the major drawback of the process lies in the toxicity of the produced nickel carbonyl molecule. Nickel carbonyl is a highly toxic and flammable vapour which has led to decades of continuous research and engineering to mitigate its risks. $\text{Ni}(\text{CO})_4$ has a threshold limit value (TLV) of 50 parts-per-billion (PPB) in Canada [32]. TLV refers to “the airborne concentration of a chemical substance under which workers can be repeatedly exposed daily, over a working lifetime without adverse effects.” [33]. In industrial-scale operations, safety measures such as constant gas monitoring and adequately sealed reactors are necessary to mitigate the risks of nickel carbonyl poisoning. During Mond and Lager’s pilot scale operation to synthesize nickel carbonyl, they were not yet aware of the danger of poisoning from the vapour, as they were more focused on avoiding CO poisoning. There were seven fatalities due to carbonyl poisoning in their Clydach operations in 1902, located in Wales. Taken aback by these events, Ludwig Mond was unmotivated to proceed with scaling up. His son, Alfred Mond, then took control of the Clydach factory and went on to merge with the American-based International Nickel Company (INCO) in 1928 [28].

2.5 Industrial Application of the Mond Process

Following the discovery of nickel carbonyl in 1890, Ludwig Mond built the first commercial nickel refinery using the practice of vapometallurgy in 1902. The refinery was owned by the Mond Nickel Company and was based in Clydach, South Wales, and its product was high-purity nickel pellets [34]. In 1929, the Mond Nickel Company was bought by Inco. The first nickel refinery built in Clydach is still operational to this day and utilizes the same process that was developed 135 years ago. The production begins with a nickel oxide feedstock obtained from Sudbury, Canada mines. Nickel oxide is continuously fed into a rotary reduction kiln, where it reacts with pure hydrogen gas at 230°C and is reduced to impure nickel granules [35]. In a subsequent volatilization reaction, the metallic nickel is exposed to a carbon monoxide environment at close to atmospheric pressure and between 38-60°C, where nickel tetracarbonyl is formed. After a 4-day reaction period, the extent of carbonylation is estimated to be 95%. [5]. Along with nickel, iron components are abundant in feedstocks used commercially, which leads to the formation of iron carbonyls under specific conditions as well. The equilibrium constants for the formation of nickel tetracarbonyl and iron pentacarbonyl at 50°C and atmospheric pressure versus 25 MPa, respectively, are presented in Equation 2-11 and Equation 2-12 ([30], [34]).



At atmospheric pressure, the formation equilibrium of iron pentacarbonyl is negligible compared to nickel carbonyl, and hence the operations in Clydach do not call for further separation of the two carbonyls through distillation. However, the kinetics of the reaction are very slow; it takes 98 hours to achieve a 90% yield. Following 6 volatilization reactors in series, the nickel carbonyl stream is sent to a thermal decomposition plant. The vapour is injected into the top of decomposition towers, and as a result of the high wall temperatures ranging from 300-500°C, the gas decomposes to form nickel powders or pellets at a 99.99% purity. The annual production capacity of nickel powders and pellets in Clydach was 10,000 metric tons

and 35,000 metric tons, respectively, as of 2017 [35]. The atmospheric carbonylation process at INCO, Clydach, is shown in Figure 2-8 [5].

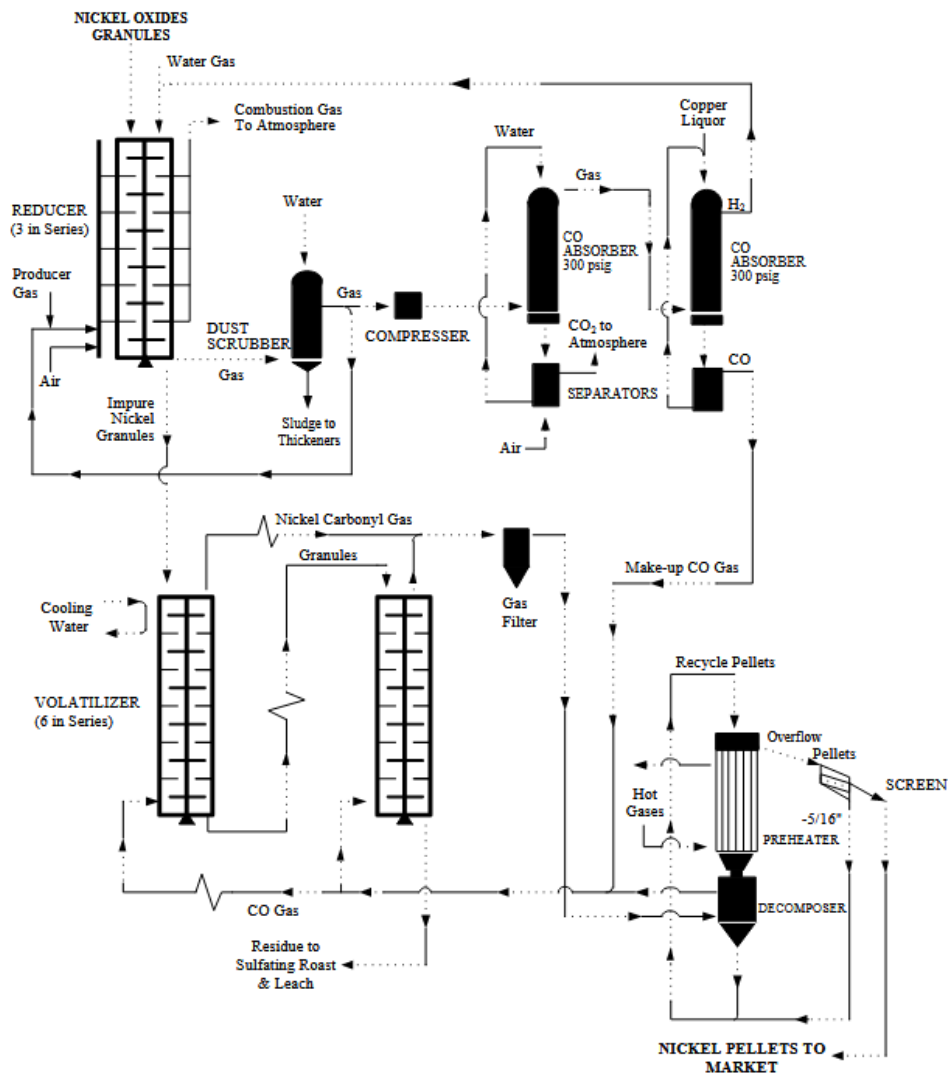


Figure 2-8: The atmospheric carbonylation process at the INCO, Clydach nickel refinery.

Reproduced under terms of the CC-BY license [5]. Copyright 2015, UNSW Sydney.

Stemming from successful operations in the Clydach plant, Inco opened a second refinery, using medium-pressure carbonylation as compared to atmospheric pressure, in the year 1973 in Sudbury, Canada. They saw that the process yielded a very high-purity product, lower energy consumption was required for refining compared to hydrometallurgy or pyrometallurgy-based processes, and even though toxic intermediates in

the form of nickel/iron carbonyls were formed, there was no off-gas venting to the atmosphere, as CO is recycled back. Furthermore, the concentration of toxic carbonyls was environmentally monitored at the PPB level [35]. The Vale Sudbury refinery uses a medium-pressure carbonylation process, which inherently produces iron carbonyl as well. Nickel and iron carbonyl are condensed and then distilled to separate the components based on the differences in volatility. The distillate, containing pure nickel carbonyl, is fed to a series of ten decomposition towers (10 meters in height and 2 meters in diameter) to produce nickel products. The bottoms product from the distillate is also decomposed to produce FeNi pellets. The kinetics of the medium-pressure carbonylation process are much faster (taking 28 hours to achieve a 98% extraction yield of Ni) [36].

In Russia, initial carbonyl refining took place before World War II. Two small plants applied a high-pressure carbonylation process in the 1920s to provide nickel to produce nickel-cadmium batteries to be used in tanks and military aircraft. Currently, a company called Norilsk Nickel employs the high-pressure process using a feed of off-spec electrolytic nickel cuts and granular nickel metalics. The feed is continuous to a static vertical carbonylation reactor, where it meets with a counter current CO stream. Formed carbonyls are distilled and a 1-meter-wide decomposer produces nickel powders and pellets [37].

Chinese operations for carbonyl nickel refining have been ongoing since the early 1960s. A company called Jiangyou Hebao Nanomaterials Co. Ltd. built a high-pressure refinery in the Sichuan province using a feed of scrap nickel to yield powders for the nuclear industry use. In the early 2000s, the Jinchuan group built a pilot-scale carbonyl refinery plant for nickel powder production with a capacity of 500 metric tons, before constructing a 10,000 metric ton commercial-scale plant in 2015. Their unit operations were very similar to Vale's because they shared the same type of feedstock – sulphide ores. The pilot plant initially used high-pressure carbonylation conditions but transitioned to a medium-pressure operation for the commercial plant [35].

A summary of the types of feed, operating conditions, capacity, extraction rates, commissioning year and types of products associated with the plants mentioned above are presented in Table 2-1 [35].

Table 2-1: A comparison of the commercial-scale carbonyl refining processes.

| Refinery | Vale Clydach | Vale Sudbury | Norilsk Nickel | Jinchaun |
|---|---------------------------|--|-------------------------------|---|
| Feed | Impure NiO | Impure Ni metallics | Ni metallics, Off- spec Ni | Ni metallics, Off- spec Ni |
| Pressure (MPa) | Atmospheric | 7.0 | 22.5 | 7.0-9.0 |
| Carbonylation Temperature (°C) | 50-60 | 170 | 150-250 | 150-220 |
| Annual Capacity (mt/a) | 45,000 | 60,000 | 5,000 | 10,000 |
| Ni extraction (%) | 90 | 97-98 | 97-98 | 97-98 |
| Commissioning Year | 1902 | 1973 | Early 1960s | 2015 |
| Typical Products | Ni powders and pellets | Ni powders and pellets, FeNi pellets | Ni powders and pellets | Ni powders and pellets, Fe powders, FeNi powders |

Historically, carbonyl refineries have used impure nickel oxide or matte feeds, but modern implementations are also considering laterite-derived intermediates such as MHPs using very similar processing conditions. MHP is treated first through thermal decomposition, where the nickel hydroxide decomposes to nickel oxide and liberates water. The nickel oxide is then reduced with hydrogen, and metallic nickel is subjected to a CO environment to form nickel carbonyl. Refining nickel out of an MHP intermediate poses a more sustainable and direct pathway to class I nickel and battery-grade materials than hydrometallurgy. Westwin Elements, based in Lawton, Oklahoma is an example of a company that is applying carbonyl refining to MHP feeds. They have commissioned a demonstration scale plant in 2024 with a capacity of 20 metric tons per year, which will use feedstocks of MHP, high-grade nickel matte and black mass. The feed is prepared and then reduced via hydrogen, then sent to their commercialized carbonyl circuit where the nickel carbonyl

is selectively volatilized. Final products, including class I nickel powder and nickel briquettes, are formed through the decomposition step. They are also producing battery-grade nickel sulfate through their commercial dissolution circuit (using sulfuric acid) [38].

2.6 Reduction of Ni(OH)₂ by Hydrogen

2.6.1 Thermal decomposition of Ni(OH)₂ to NiO

The first step in the reduction of nickel hydroxide by hydrogen is the thermal decomposition to nickel (II) oxide. Ni(OH)₂ is thermally stable at ambient conditions but starts to dehydrate upon heating. The decomposition, also known as dehydroxylation of Ni(OH)₂ powder (removal of structurally bound hydroxide groups), is observed within a temperature range of 210°C and 280°C. The endothermic reaction of Ni(OH)₂ dehydroxylation under an inert or hydrogen atmosphere within this temperature range is shown in Equation 2-13. The mass losses (in terms of mass percentage) associated with the decomposition of Ni(OH)₂ powder under an inert atmosphere in a PTGA at temperatures of 300°C, 400°C, and 500°C were found to be 23.7%, 26.1%, and 26.9% respectively [39]. Through X-ray diffraction analysis, it has been shown that no intermediate crystalline phases are formed in the decomposition of Ni(OH)₂ to NiO. At temperatures around 300°C, the NiO product retains the fine particulate nature of the precursor, as this temperature range is moderate enough to avoid any sintering [40].



Kinetic studies of Ni(OH)₂ decomposition done in a PTGA under isothermal conditions show that the reaction accelerates with temperature in the 200°C to 300°C range, which then starts to plateau near 90% conversion. The deceleration in the reaction is caused by the retention of the product water within the NiO lattice and steric hindrance of the remaining residual hydroxyl groups. Based on numerical model fitting of the PTGA data (using a 10 mg loaded sample), a first-order random nucleation mechanism was found valid in the 20-70% conversion range, where the kinetics were linear. This indicates that NiO nucleates at random points on Ni(OH)₂ particles and continues to grow, rather than the reaction moving inward from the particle surface (as described by a shrinking-core model). Scanning electron microscopy imaging shows that there is no evidence of a sharp reaction interface (disproving the possibility of a moving boundary reaction mechanism wherein there is an unreacted core with a distinct NiO shell). Outside this conversion range, the initial induction phase and final declaratory phases did not obey first-order kinetics. At a higher sample loading of 100 mg, the reaction seemed to obey a multi-step diffusion/first-order combined mechanism,

which was likely attributed to the longer exit path lengths for product water. The apparent activation energy for Ni(OH)₂ dehydration is related to the energy required to break O-H bonds and form the NiO lattice. The isothermal study conducted by Carney et al. [40] reported this value to be 130-140 kJ/mol.

2.6.2 Reduction of NiO to Metallic Ni

The reduction of bulk nickel oxide with hydrogen to form metallic nickel is a critical step preceding the carbonylation reaction. It is a solid-gas reaction that can proceed under different rate-limiting or diffusion-limited mechanisms and is known to be affected by temperature, NiO particle size/morphology, and porosity of the resultant Ni product. Key kinetic models presented in the literature that are based on a chemical interface-controlled mechanism include nucleation-growth models (Avrami-Erofeev series) and phase-boundary models (shrinking core). Diffusion-controlled models are presented by Jander or Ginstling-Brounshtein equations.

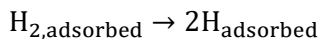
Bandrowski et al. [41] proposed that NiO reduction by hydrogen occurs through two simultaneous reactions: the first is a reaction between NiO and the adsorbed hydrogen on the NiO surface, and the second is at the Ni/NiO boundary interface once metallic nuclei are formed. Since H₂ absorbs poorly onto the NiO surface, the first reaction is rate-limiting. As more Ni nuclei appear, the second reaction dominates as H₂ more readily dissociates on the Ni surface. This mechanism leads to sigmoidal reduction kinetics, including an induction period, then an accelerated conversion, and then a decelerated conversion as the NiO surfaces are saturated [41]. The induction period is the initiation of the reduction process, where fresh nuclei (crystallization centers of the new phase) start to develop and grow. The following autocatalytic period commences once enough Ni nuclei have formed and can catalyze the dissociation of adsorbed H₂. As the concentration of remaining NiO sites decreases, the reaction rate drops; this phase is the slow termination phase. Richardson et al. [42] reported that the reduction of porous bulk NiO entered the slow termination phase after 80% conversion and it followed a pseudo-first-order behaviour. This mechanism is the basis for nucleation-and-growth models; however, the reduction of larger particles has also been modelled using shrinking-core models. In both cases, the role of oxygen vacancies is critical, and it governs the different kinetic behaviours of reduction.

Under a H₂ atmosphere, NiO begins to react at temperatures as low as 250-300°C, but the reduction at these relatively low temperatures proceeds at a slow rate, which is followed by a long induction period. Manukyan et al. [43] found that in a lower temperature regime of 270-500°C, the kinetic curves have a sigmoidal shape with induction times of up to 2000 s, and result in incomplete conversion (indicated by presenting a degree

of conversion of ~0.4 for a reduction temperature of 270°C). Low-temperature reduction was found to create a complex polycrystalline structure of Ni/NiO with a characteristic pore size on the order of 100 nm. In comparison, no induction period was observed for reduction under the temperature range of 900-1320°C and full conversion was reported, which occurred in under 40 s. At the higher temperature regime, the resultant metallic structure after the reaction is defined by its fine characteristic pore size, under 10 nm [43]. Richardson et al. [42] studied the reduction mechanism of porous bulk NiO at temperatures of 175-300°C, and their XRD results showed that NiO is directly converted to Ni without the appearance of any intermediate oxide phases. In a study aimed at studying the reduction of NiO powder and pellets through thermogravimetric analysis, Chatterjee et al. [44] reported that the activation energy for reduction was 20.14 kJ/mol and 19.21 kJ/mol for the powder and pellet, respectively.

2.6.3 Role of Oxygen Vacancies

Bulk NiO reduction predominantly occurs on the interface between the solid phases of Ni and NiO, and the oxygen vacancies in between are crucial in the reaction mechanism. The most common face of a NiO crystal is the NiO(100) surface, which is not readily reactive with H₂. The first phase of the reaction is the adsorption of the H₂ molecule to the nickel surface. H₂ molecules bind more favourably to Ni-Ni sites as compared to Ni-O sites, and they do not bind to oxygen-covered sites at all. On a NiO(100) surface, the presence of oxygen vacancies increases the adsorption energy of H₂ and lowers the activation energy associated with the cleavage of the H-H bond. Rodrigues et al. [45] estimated the adsorption energy of H₂ on a flat NiO(100) surface to be >5kcal/mol, which increased to 12.8 kcal/mol on a surface rich with oxygen vacancies. The dissociation of the adsorbed H₂ molecule, as per Equation 2-14, was found to be more favourable on two neighbouring Ni atoms compared to adjacent Ni and O atoms (shown by a decrease in activation energy by 1.6 kcal/mol) [45]. A schematic of a 4-layer slab of NiO(100) surfaces with a surface level oxygen vacancy before and after hydrogen introduction is shown in Figure 2-9[45].



Equation 2-14

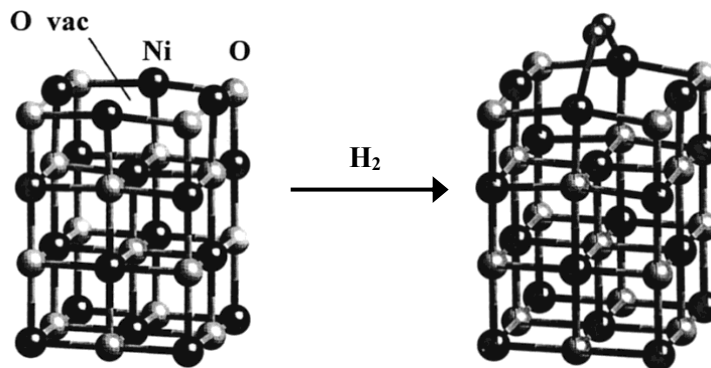


Figure 2-9: A 4-layer slab view of NiO surfaces before hydrogen introduction (left) and after (right) where nickel atoms are black spheres and oxygen atoms are grey. Reproduced with permission [45].

Copyright 2002, American Chemical Society.

The energy barrier associated with the cleavage of the H-H bond was estimated to be 16 kcal/mol which decreased to 8 kcal/mol due to the H-H bond length increasing from 0.74 to 0.87 Å. Oxygen vacancies were found to be 9.1 kcal/mol more stable in the bulk material compared to a system with surface vacancies. However, in the presence of hydrogen, oxygen vacancies are not static and migrate to the NiO surface, with direct access to incoming hydrogen molecules [45]. The migration is an exothermic process ($\Delta H = -5.8$ kcal/mol), and causes the surface vacancy sites to be 24 kcal/mol more stable than bulk sites [46]. Hence, the stable vacant oxygen sites on the surface provide H₂ easier access to metallic nickel within the lattice, which is a better hydrogen dissociating agent (can cleave the H-H bond) than NiO. After there are sufficient metallic nickel sites available on the NiO surface, the autolytic phase of reduction starts, where hydrogen dissociation on the NiO surface can occur for a prolonged period of time. The reduction of NiO specifically is generally modelled with the assumption that NiO is converted to metallic Ni without the formation of any intermediates (e.g. Ni₃O₂). However, the exact mechanism of reduction varies widely and is based on different kinetic models [45].

2.6.4 Kinetic Models and Mechanisms

2.6.4.1 Nucleation and Growth (Avrami-Erofeev) Models:

Both Ni(OH)₂ decomposition and NiO reduction are well described by Avrami-Erofeev models, in which the formation of product nuclei and subsequent growth governs the reaction rate. Experimental data validate that a first-order decomposition reaction was suitable for Ni(OH)₂ based on fitting of experimental data [40]. Kinetics based on Avrami-Erofeev equations relate the reaction rate constant and temperature to the

reduction degree of the species of interest. The general form of these kinetics is denoted as AE_n , and it is presented in Equation 2-15 [39].

$$AE_n: kt = (-\ln(1 - x))^{\frac{1}{n}} \quad \text{Equation 2-15}$$

Where k is the apparent reaction rate constant, x is the fractional conversion (wt.%), t is the reaction time, and n is the Avrami-Erofeev exponent, which is found by fitting the model to experimental data.

A study by Carney et al. [40] on the isothermal decomposition kinetics for $Ni(OH)_2$ powder was unable to report a specific geometry-defining Avrami exponent. Pöyhtäri et al. [39] fitted the Avrami-Erofeev kinetic model for direct $Ni(OH)_2$ reduction and NiO reduction at various isothermal conditions of 300, 400, and 500°C. Based on their fitting results for $Ni(OH)_2$ reduction, they reported Avrami exponents of 1.02, 1.15, and 1.11 for the three temperatures, respectively. The exponents for NiO reduction were found to be 1.57, 1.20, and 1.10, respectively [39]. Through a series of PTGA experiments for the reduction of NiO powder, Lee and Min [29] suggested that a 2nd order Avrami-Erofeev model ($n=2$) was most suitable to model the kinetics. They conducted their isothermal reduction at temperatures ranging from 400 to 700°C.

2.6.4.2 Phase Boundary (Interface) Controlled Models:

Geometric contraction models (denoted by “ R_n ”) are an example of the shrinking core model where the reaction occurs on the phase boundary and consumes the solid particle slowly. The reaction is limited by the formation of products on the phase boundary, which inhibits gas diffusion to the product surface. The shrinkage of the unreacted zone can be modelled as one-, two-, or three-dimensional (R_1 , R_2 , R_3 , respectively). The general form of the geometrical contracting model is denoted as R_n and is shown in Equation 2-16 [39].

$$R_n: kt = 1 - (1 - x)^{\frac{1}{n}} \quad \text{Equation 2-16}$$

Where k is the apparent reaction rate constant, x is the fractional conversion (wt.%), t is the reaction time, and n is the dimension of contraction (ranging from 1 to 3).

When considering the kinetics for isothermal decomposition of $Ni(OH)_2$, there are conflicting conclusions from various studies on whether a contracting area/volume model is an appropriate model. El-Salaam and Hassan [47] proposed a contracting volume mechanism for $Ni(OH)_2$ powder decomposition with $E_a = 119$ kJ/mol using a sample size of 500 mg. Hazell and Irving [48] proposed a contracting area mechanism with $E_a = 95 \pm 5$ kJ/mol for conversion under 60% and using a sample size of 60%. Both studies found that the

retention of product water at higher conversions made model fitting less accurate in that region. However, the study from Carney et al. [40] deduced that $\text{Ni}(\text{OH})_2$ followed first-order kinetics rather than a contracting volume/area mechanism. They also noted that sample size for decomposition experiments could be the leading cause of the differing observed mechanisms; Carney et al. [40] used a sample size of 10 mg in their study as compared to 500 mg in the previous isothermal studies. At a sample size of 10 mg and low decomposition temperatures, SEM images did not show any evidence of cracking or surface changes across the particles due to the reaction. These conclusions support that a boundary reaction mechanism was not suitable for modelling the decomposition at these specific conditions. The SEM images showing the powder particles of fresh, partially converted (56%), and nearly fully converted (92%) $\text{Ni}(\text{OH})_2$ are shown in Figure 2-10 [40].

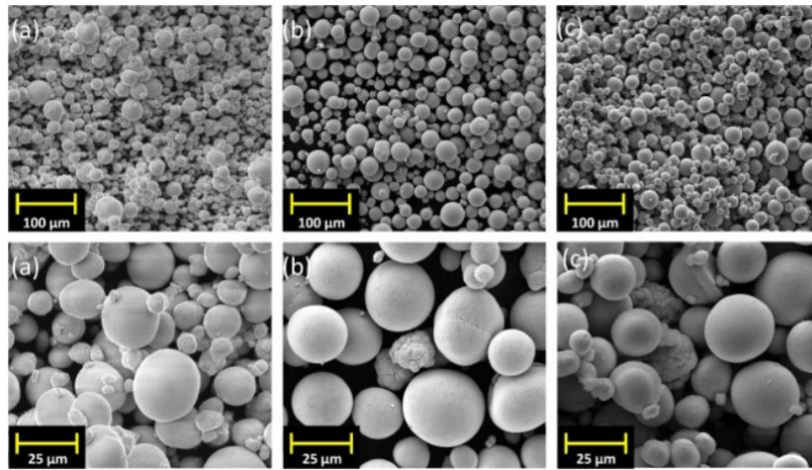


Figure 2-10: SEM micrographs of: (a) feed $\text{Ni}(\text{OH})_2$. (b) Partially converted PTGA product after 2-hour isothermal hold at 200°C. (c) Nearly fully converted PTGA product after 2-hour isothermal hold at 250°C. Reproduced with permission [40]. Copyright 2015, Elsevier.

For NiO reduction, a moving-interface model, or a contracting area/volume model (as described above) applies under certain conditions, under which a Ni layer coats the NiO surface. Pöyhtäri et al. [39] conducted PTGA experiments to study the direct reduction of $\text{Ni}(\text{OH})_2$ powder with H_2 , using a feed of 100 mg. The sample was first heated at a rate of 20°C/min under an Ar environment, and the inert environment was maintained for an additional 10 minutes after the targeted reduction temperature was achieved, to decompose the hydroxide. Reduction experiments were carried out at temperatures of 300, 400, and 500°C. Results from their model fitting indicated that the reaction approaches AE1 model behaviour at 300°C, and at higher temperatures, the phase-boundary-controlled reactions (R2, R3). The R2 model was a good fit for

higher reduction temperatures, but the study could not discriminate between the AE_n and R3 models at 300°C [39].

2.6.4.3 Diffusion-Controlled Models

Diffusional limitation can play a role in solid-gas reactions in one of two ways: 1) external mass transfer of gas to and from the bulk reacting solid, and 2) internal diffusion of reactants/products within the solid (or through the product layer). External mass transfer diffusion resistance can be minimized by using small sample sizes, using high H_2 flow rates, and well-mixed conditions. Similar to the geometric contraction models, there are different diffusion models for 1-, 2-, or 3-dimensional geometries (denoted by “ D_n ”), presented in the following equations [39].

$$D_1 (1 - D): \quad kt = x^2 \quad \text{Equation 2-17}$$

$$D_2 (2 - D \text{ Valensi Equation}): \quad kt = (1 - x)\ln(1 - x) + x \quad \text{Equation 2-18}$$

$$D_3 (3 - D \text{ Jander Equation}): \quad kt = \left[1 - (1 - x)^{\frac{1}{3}}\right]^2 \quad \text{Equation 2-19}$$

$$D_4 (3 - D \text{ Ginstling - Brounshetin Equation}): \quad kt = \left(1 - \frac{2x}{3}\right) - (1 - x)^{\frac{2}{3}} \quad \text{Equation 2-20}$$

Where k is the apparent reaction rate constant, x is the fractional conversion (wt.%), and t is the reaction time.

Chatterjee et al. [49] studied the kinetics of the hydrogen reduction of NiO powder compared to pellets and specifically varied the hydrogen flow rate to see the effect on gas diffusion into the solid particles. Between 300-600°C, they found that the rate-controlling step was the diffusion of H_2 and product H_2O through the gas boundary layer when the hydrogen flow rate was not sufficiently high. The activation energies for the reduction of NiO powder and pellet were found to be 20.14 and 19.21 kJ/mol, respectively (lower than the true chemical activation energy), which is characteristic of the rate controlled by gas film diffusion [49]. Generally, intra-particle diffusion does not limit $Ni(OH)_2$ reduction because the product Ni tends to form as a highly porous structure. Manukyan et al. [43] found that internal diffusional effects become more prominent at higher reduction temperatures; they showed that reduction under 500°C was accurately modelled by the AE_n equations, whereas the D1 model was relevant for reduction temperatures above 900°C (due to sintering effects of the product Ni layer) [43]. Plascencia and Utigard [50] conducted reduction

experiments of Tokyo-based NiO with H₂ in a PTGA, and through kinetic model fitting, concluded that diffusion control significantly competes with the chemical reaction at reduction temperatures over 950°C.

2.7 Carbonylation of Nickel

2.7.1 Reaction Kinetics

2.7.1.1 Rate Laws and Pressure/Temperature Dependence

The carbonylation reaction of metallic nickel and the decomposition reaction take place according to Equation 2-9 and Equation 2-10. The carbonylation reaction proceeds with the adsorption of CO on the Ni particles, formation and desorption of $\text{Ni}(\text{CO})_4$, and external and internal mass transfer of reaction and product gases. At sufficiently low pressures, studies of non-catalytic carbonylation of nickel have treated the rate as first-order in CO partial pressure for a given Ni surface area. Cui et al. [5] studied this reaction at 80-100°C and CO pressure of up to 155 atm and CO gas flow rate of 0.5 L/min. The extents of Ni carbonylation for the various explored operating conditions are presented in Figure 2-11 [5].

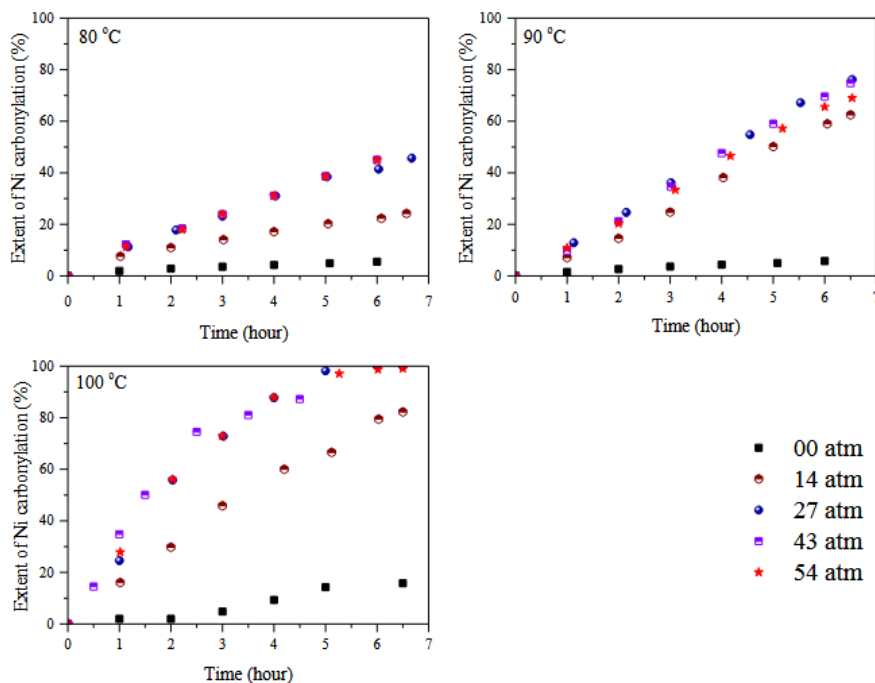


Figure 2-11: Measured carbonylation of nickel at 80, 90, and 100°C and CO pressure up to 54 atm gauge pressure. Reproduced under terms of the CC-BY license [5]. Copyright 2015, UNSW Sydney.

The results showed that the carbonylation rate increased with increasing temperature. Even at a pressure of 27 atm, they achieved a 99% degree of carbonylation at 100°C. Increasing pressure from 0-27 atm has a

significant positive effect on the rate but further increase in pressure to 54 atm showed only a minor effect on the reaction rate. This suggests that saturation of surface sites or diffusional limitations play a role at higher CO pressures. When conducting analysis on the particle size of the feed material, the study achieved a 98% extent of nickel carbonylation when the mean particle size was 1.1 microns. When the same experiments were conducted with particles having a mean size of 2.67 microns, the extent decreased to 67%. Cui et al. [5] treated the irreversible carbonylation reaction of nickel to be first order in CO pressure (presented in Equation 2-21) and also presented an equation to determine the reaction rate constant (presented in Equation 2-22).

$$r = SkP_{CO} \quad \text{Equation 2-21}$$

$$k = Ae^{-\frac{E_a}{RT}} \quad \text{Equation 2-22}$$

Where S is the interfacial gas-solid area, k is the reaction rate constant, P_{CO} is the partial pressure of CO at the interface, A is the pre-exponential factor, E_a is the activation energy (J/mol), R is the universal gas constant (J/(mole · K)), and T is temperature (K).

Goldberger and Othmer [51] gathered kinetic data for the nickel carbonyl reaction and showed that it follows a modified first-order rate equation. Due to the apparent changes in nickel reactivity with changing temperature and pressure, the rate expression included an empirical term related to the activity of nickel. The modified first-order rate expression is given by Equation 2-23. An increase in nickel activity with pressure was observed in their study, and they deemed this to be due to an increase in nickel surface covered by adsorbed CO at higher pressures. The increase in nickel activity at 75°C from 1 atm up to 4 atm is shown by Figure 2-12 [51].

$$kt = \frac{\ln\left(\frac{a_s^0}{a_s^0 - X}\right)}{P_{CO,i} - P_{CO,eq}} \quad \text{Equation 2-23}$$

Where X is the fraction of nickel converted, a_s^0 is the surface activity of nickel (at time = 0), k is the rate constant, $P_{CO,i}$ and $P_{CO,eq}$ are the partial pressures of CO at the reaction interface and equilibrium, respectively, and t is time.

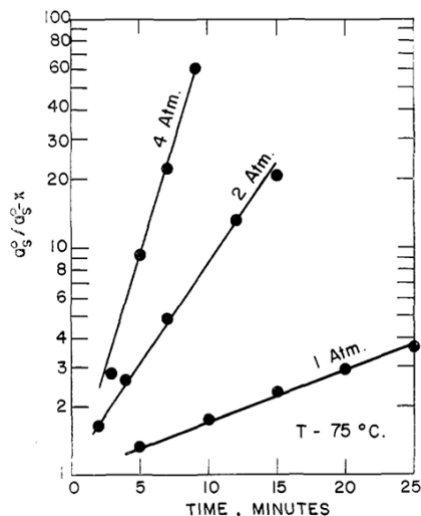


Figure 2-12: Fitting of the modified first-order rate expression for nickel carbonyl formation to experimental data by Goldberger and Othmer to obtain nickel activity at 1 atm, 2 atm, and 4 atm.

Reproduced with permission [51]. Copyright 1963, American Chemical Society.

Lascelles and Renny [52] from INCO Europe Ltd., Clydach, UK, conducted the carbonylation reaction of nickel single crystal disks in 1892. The disks were 25 mm in diameter, 0.7 mm thick, and of (100), (110), and (111) orientation. In their work, they observed that there is an apparent exponent on the pressure term of the reaction rate, which is a function of carbonylation temperature (i.e. reaction rate is proportional to P_{CO}^α). When measuring $Ni(CO)_4$ formation rates on single-crystal nickel sites, they found the pressure exponent increasing from 0.8 at 65°C to 1.9 at 130°C and 2.9 at 160°C. Under atmospheric pressure, the maximum carbonylation rate occurred at a temperature of $135 \pm 2.5^\circ C$ (T_{max}) for all crystals. The obtained rates of nickel carbonyl formation at T_{max} for Ni(111), Ni(100), and Ni(110) were 4.4×10^{-9} , 1.4×10^{-9} , and 1.7×10^{-9} mole/(cm² · min) respectively. The apparent activation energy for the reaction was 35.6 ± 2.1 kJ/mole for all three crystals from 50-100°C [52].

2.7.1.2 Activation Energies

The activation energy for Ni carbonylation reflects the energy required to dissociate the Ni atoms from the solid lattice and then coordinate them with the CO ligands. In the work of Cui et al. [5], under a CO partial

pressure of 54 atm and a temperature range of 80-100°C, an activation energy of 114 kJ/mole was found for nickel powder, which more or less agreed with Redmon's obtained value of 127 kJ/mol in 1980 [5]. During their study on nickel single crystals, Lascelles and Renny [52] reported that the apparent activation energy for the reaction was 35.6 ± 2.1 kJ/mole for all three crystals from 50-100°C. This value is much lower than the number reported by Cui et al. [5], likely because single nickel crystals contain an orderly atomic pattern with no grain boundaries and are very pure, requiring lower energy for the dissociative adsorption of CO onto Ni surfaces. Greiner and Menzel's kinetic studies [53] showed that the activation energy of sulfur-covered Ni(100) site is reduced to 8 kJ/mole, and the maximum carbonylation rate occurs at 62°C. Sulfur is known to be an effective poison for catalytic reactions on Ni and other transition metals involving CO. A small sulfur coverage (less than 20% of the monolayer) is sufficient to saturate this effect. The effect is connected with the suppression of the irreversibly chemisorbed CO, which would otherwise prevent the Ni(CO)₄ molecules from forming. The CO binding energy appeared to decrease gradually with sulfur coverage (important for carbonyl formation), and in turn caused the activation energy to decrease linearly [53]. Cui et al. also explored the catalytic effect of sulfur on carbonylation, concluding that an addition of 0.1 wt.% sulfur decreased the reaction time to 60% extent from 4.2 hours (non-catalytic reaction) to less than 40 minutes. However, increasing sulfur from 0.1 wt.% to 0.7 wt.% reduced the overall extraction efficiency from 90% to 80% [5].

2.7.2 Mechanistic Models

2.7.2.1 Reaction Pathway

The mechanism for Ni carbonylation is multi-step as CO molecules coordinate to a surface Ni atom and cause its detachment as gaseous Ni(CO)₄. It is established in literature that the reaction forms intermediate nickel carbonyl species under different conditions, in the form of Ni(CO), Ni(CO)₂, and Ni(CO)₃. Liang et al. [54] showed evidence of a sequential surface reaction through intermediates at low pressure (10⁻⁸ atm) from mass spectroscopy. The sequential steps are presented below [54]:

1. Mono-carbonylated compound forms as the rate-limiting step, creating a chemi-sorbed surface layer from the removal of Ni from the lattice. At low CO coverage, CO adsorption is reversible. The entire surface is first saturated with the mono-ion.
2. Di- and tri-carbonylated compounds form after the surface is saturated with the mono-ion. The di- and tri-carbonylated molecules create a physisorbed surface layer.

3. The physisorbed surface layer allows for the fourth carbonyl ligand to attach and form $\text{Ni}(\text{CO})_4$ gaseous species.

The transient intermediates are not stable as free molecules under ambient conditions but can form for short periods of time on the Ni surface or revert back to Ni if the CO supply is insufficient. In Redmon's research from 1980 [55], he noted that the rate-determining step is the formation of the monocarbonyl intermediate on the surface, which requires the largest activation energy compared to the formation of the other intermediates.

2.7.2.2 Role of Surface Structure

The atomic structure of the Ni surface influences the rate of carbonylation and activation energy. Low-coordinated surface sites, such as steps, kinks, and defects, are shown to promote nickel removal as compared to terrace sites. A generic crystalline arrangement showing where terrace, kink, and stepped sites are located, and a specific Ni(211) surface is shown in Figure 2-13 [56].

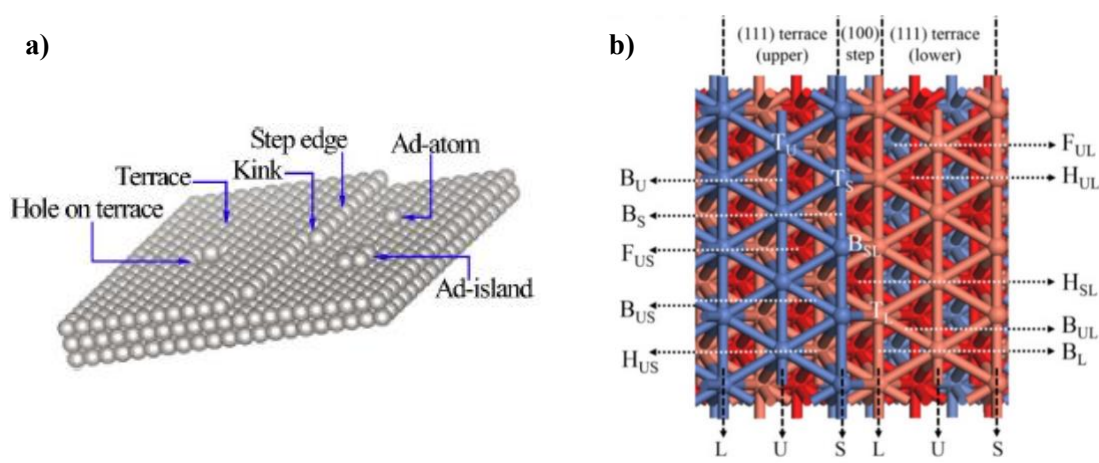


Figure 2-13: A generic crystalline arrangement highlighting a) terrace, kink, and stepped edge sites and b) a Ni(211) surface, composed of (111) terrace sites and (100) stepped sites (right).

Reproduced with permission [56]. Copyright 2021, Elsevier.

For the formation of $\text{Ni}(\text{CO})_4$, binding to a stepped edge is not favourable because CO chemisorbs strongly to a step, which causes the binding of the other three carbonyl ligands to be harder and less likely [46]. Anderson et al. [57] used density functional theory (DFT) to calculate the barrier for dissociation on various Ni surfaces. The dissociation barrier for CO on Ni(100) and Ni(110) steps was found to be 90 kJ/mole less

than on Ni(111) terrace site, which means that CO preferentially chemisorbs to the stepped edges and highly limits the rate of Ni(CO)₄ formation. The addition of sulfur, generally done by pulsing a small amount of H₂S along with the CO stream, can be used to prevent the CO from binding to the stepped sites. A proposed mechanism by Anderson et al. [57] is that sulfur creates a physical barrier preventing the chemisorption of CO at that site. The same study showed that the dissociation barrier of CO onto a step covered by sulfur is 47 kJ/mole larger than on the Ni (111) site [57].

Chapter 3

Experimental and Methodology

The experimental study of this project includes the reduction and carbonylation of nickel from MHPs. This chapter discusses the materials, sample preparation methods, tools, equipment, and instrumentation used in the flow system, as well as the experimental procedure and characterization techniques employed. Each powder sample was first pressed into a pellet, which was then placed into a quartz crucible and loaded into the PTGA. After reduction and carbonylation experiments, the residue was characterized by ICP-OES, BET surface area analysis, and an inline FTIR spectrometer was used to detect the presence of various product gases.

3.1 Materials

The gases and reagents used for the reduction and carbonylation experiments in this project are listed in Table 3-1.

Table 3-1: Gases and reagents used in experiments.

| Gas | Specification and Supplier | Application |
|---------------------------------|---|---|
| Argon (Ar) | 99.995% purity, from Linde Canada Inc. | Inert reaction gas (RG) |
| Nitrogen (N₂) | 99.995% purity, from Linde Canada Inc. | <ol style="list-style-type: none"> 1. Purge gas (PG) for the PTGA – envelopes the balance mechanism within the PTGA to maintain constant balance conditions 2. Furnace gas (FG) for the PTGA – provides heat to the vessel 3. Adsorption gas for BET surface area analysis |
| Hydrogen (H₂) | 99.999% purity from Linde Canada Inc. | Reaction gas (RG) for the reduction environment |

| | | |
|--------------------------------------|---|--|
| Carbon Monoxide (CO) | 99.5% purity from Linde Canada Inc. | Reaction gas (RG) for the carbonylation environment |
| Hydrochloric acid (HCl) | 37% HCl from Sigma-Aldrich | A component of aqua regia, used to digest metallic compounds prior to ICP analysis |
| Nitric Acid (HNO₃) | 70% HNO ₃ from Sigma-Aldrich | A component of aqua regia, used to digest metallic compounds before ICP analysis |

The four MHP samples that were used in this project for reduction and carbonylation tests are listed in Table 3-2.

Table 3-2: Samples used for reduction and carbonylation experiments.

| Sample | Specification and Supplier | Application |
|---------------|--|----------------------|
| L1-MHP | MHP derived from Turkish laterite ore, powder | Feed to PTGA reactor |
| L2-MHP | MHP derived from Indonesian laterite ore, powder | Feed to PTGA reactor |
| B1-MHP | MHP derived from black mass, powder | Feed to PTGA reactor |
| B2-MHP | MHP derived from black mass, powder | Feed to PTGA reactor |

The compositions of the four MHPs (based on elements of highest weight percentage and elements of interest) are listed in Table 3-3, as found from the ICP analysis.

Table 3-3: Composition of the MHP samples used in reduction and carbonylation tests (wt.%).

| Sample | Ni | Co | Mg | Al | Mn | Li | Na | Balance (hydroxide and crystalline water) |
|---------------|-----------|-----------|-----------|-----------|-----------|-----------|-----------|--|
| L1-MHP | 32.0 | 1.5 | 1.4 | 0.39 | 4.3 | - | - | ~ 60 |
| L2-MHP | 42.6 | 5.1 | - | 0.2 | 1.0 | 0.8 | - | ~ 50 |
| B1-MHP | 48.1 | 3.7 | - | 1.2 | 3.2 | - | - | ~ 44 |
| B2-MHP | 32.4 | 11.7 | - | 0.1 | 10.6 | 0.3 | 4.4 | ~ 40 |

3.2 Sample Preparation

The MHPs, as received from the suppliers, were in fine powder form. From initial testing of the MHP powders in the PTGA, it was found that there was significant entrainment of the powders when depressurizing the reactor from higher pressure (at 450 psig). The fine particles were being carried out of the quartz basket due to the high flow rate of gas exiting the reactor, causing an artificial mass loss unrelated to the reduction or carbonylation reaction. For this reason, the powders were compressed into a pellet prior to reduction experiments. Approximately 1 gram of powder was placed in a 14 mm pellet die set, which was compressed at a load of 7 metric tons for 2 minutes using a Carver 12-ton hydraulic press (model 3912). The 14 mm MHP pellets of approximately 1 gram served as the initial feed material to the PTGA reactor.

3.3 Flow System Setup and Procedures

The flow system used in this research project revolved around a high-pressure thermogravimetric analyzer (PTGA), which provided the reaction environment for both reduction and carbonylation tests. Thermogravimetric analysis is a technique that measures the mass change of a sample as it is subjected to a target temperature under a controlled, reactive environment. Descriptions of the main components of the flow system are listed below and are shown as part of a process flow diagram in Figure 3-1.

PTGA Apparatus: The Cahn TG 151 unit has a 10 g sample loading capacity and 35 mL sample volume capacity. It can operate under various gas atmospheres, including toxic and flammable gases. It is rated for a maximum pressure of 1000 psig at 1000°C. The feed was first weighed and then placed in a cylindrical quartz basket with a diameter of 19 mm, a height of 20 mm, and a dry weight of 2.5 g. The basket was then

hung inside the reactor tube, which has a diameter of 38 mm. The PTGA seals shut, enclosing the sample within the reactor tube. The PTGA uses three gases: Nitrogen PG, Nitrogen FG, and either Argon, Hydrogen, or Carbon Monoxide RG (depending on the reaction type). The maximum flow rate of each gas was limited to 200 ml/min in the PTGA, as recommended by the operating manual.

Back-pressure regulators (BPRs): A constant reaction pressure within the PTGA was maintained through two stainless steel back-pressure regulators from Swagelok. The low-level BPR from Swagelok (part number: KBP1F0D4A5A20000) was capable of regulating pressure from 0-100 psig and was used for reduction experiments conducted at 6 psig. The high-level BPR from Swagelok (part number: KBP1D1C5JA10) was capable of regulating pressure from 0-500 psig and was used for high pressure carbonylation tests at 150 psig and 450 psig.

Fourier Transform Infrared Spectrometer (FTIR): The FTIR used in this project was the Varian 640-IR. FTIR spectroscopy is a technique used to analyze the infrared spectrum of a sample to provide detection and concentration (to some limit) of the evolved gases. Molecules in the evolved gas absorb energy at specific frequencies, which correspond to their vibrational bonds. The FTIR was used as an inline process gas detector, which allowed for the detection of water vapour produced during reduction tests, CO reactant gas and $\text{Ni}(\text{CO})_4$ that were produced during carbonylation tests. The length of the gas cell located inside the FTIR module was 10 cm.

Decomposition Furnace: A tube furnace rated for 1100°C was used downstream of the FTIR to decompose any produced carbonyls (to CO gas and metallic compounds) and to heat the exhaust gas prior to entering the catalytic converter. The decomposition furnace typically operated at 450°C, a high enough temperature to fully decompose any produced carbonyls.

Catalytic Converter: A standard automotive catalytic converter was used to completely oxidize CO to CO_2 before venting to the fume hood.

Flowmeters: A total of 6 different flowmeters were used to control the flowrate of gases in the system. They are listed in Table 3-4

Table 3-4: Description and application of flowmeters within the system.

| Flowmeter Name | Gas | Range (ml/min) | Control Device |
|-----------------------|-------------------|-----------------------|---|
| FC1 | N ₂ PG | 0-400 | OMEGA FM Control Box |
| FC2 | N ₂ FG | 0-400 | OMEGA FM Control Box |
| FC3 | Ar RG | 0-400 | OMEGA FM Control Box |
| FC4 | Air | 0-30 LPM | Swagelok forward-pressure regulator, flow monitored by OMEGA manual rotameter |
| FC5 | H ₂ RG | 0-200 | Bronkhurst Control Box |
| FC6 | CO RG | 0-200 | Bronkhurst Control Box |

Gas Detectors (GD): There were four gas detectors placed inside the fume hood as a safety measure to detect the presence of toxic gases during venting procedures or in the event of a gas leak. They are listed in Table 3-5.

Table 3-5: Description and application of gas detectors within the system.

| Gas Detector (GD) | Type of Gas | Location | Alarm Condition |
|--------------------------|-------------------------------------|--|---|
| GD1 | O ₂ | Exhaust line tubing in the fume hood | Concentration < 18% (when the alarm sounds, it is indicative that H ₂ concentration is greater than 3% during reduction experiments) |
| GD2 | CO | Fume hood – open to a ventilated environment | Concentration > 25 ppm for 10 mins or >100 ppm for 3 seconds |
| GD3 | H ₂ | Fume hood – open to a ventilated environment | Concentration >100 ppm |
| GD4 | CO-O ₂ -H ₂ S | Exhaust line tubing in the fume hood | CO Concentration >25 ppm |

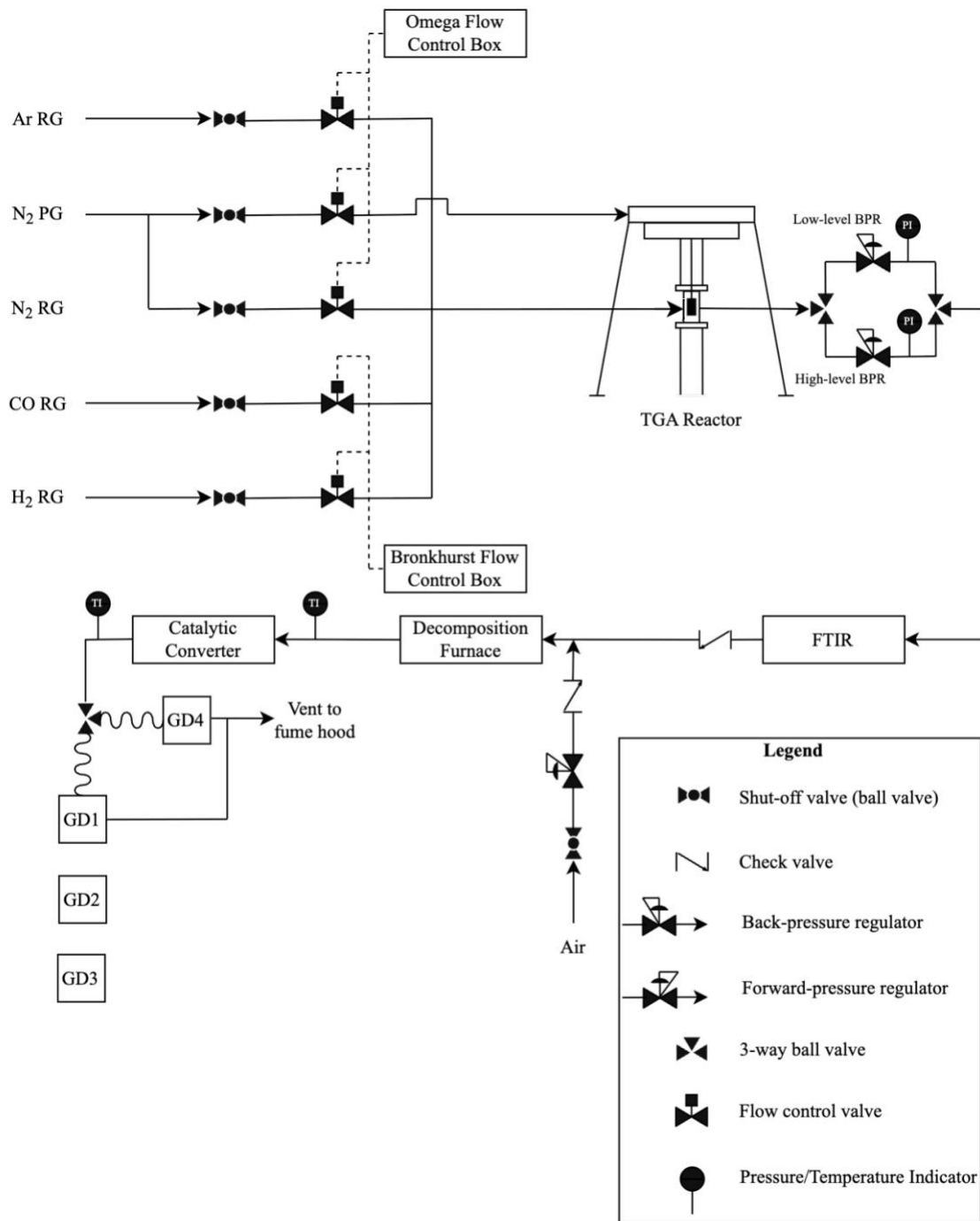


Figure 3-1: Flow diagram of the laboratory-scaled system within a fume hood, used for reduction and carbonylation experiments.

3.3.1 Reduction Experiments

Reduction experiments were conducted in the flow system shown in Figure 3-1. Prior to reduction experiments, the mass of the quartz basket was measured, and the mass of the sample inside the basket was measured. The sample weight and desired temperature profile for the reduction experiment were entered into the *Cahn PTGA* software. After the sample is placed within the reaction tube of the PTGA, gas flows are established, and the reactor is pressurized to 6 psig (near atmospheric pressure). A typical temperature profile utilized for the reduction experiments is split into four stages, shown in Figure 3-2.

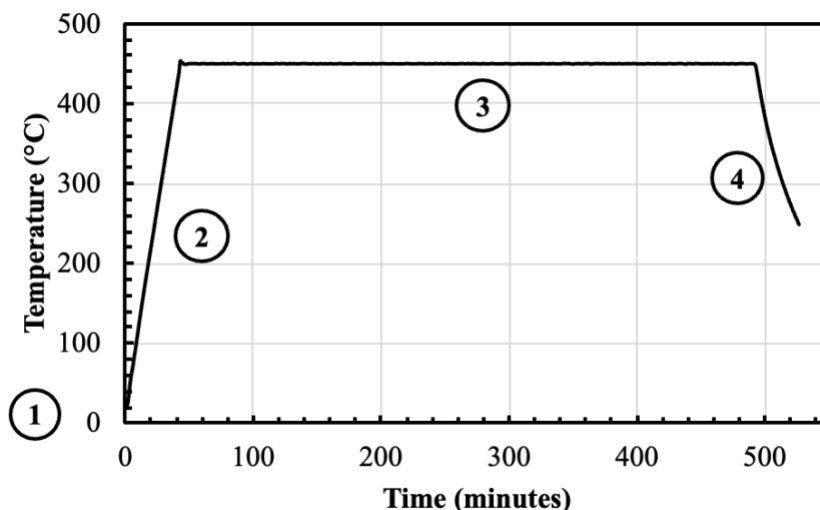


Figure 3-2: Typical temperature profile of reduction experiments.

Stage 1: Establishing gas flows and pressurizing the reactor – RG: Ar, FG: N₂, PG: N₂

Before introducing gases from the cylinders, the air flow rate was set to 15 L/min. The decomposition furnace was kept off for reduction experiments. The N₂ flow was initiated, and the flow rates for the PG and FG were set to 200 ml/min through the OMEGA FM control box. The Ar RG flow was initiated, and the flow rate was set to 200 ml/min. The low-level BPR was used to maintain the PTGA pressure at 6 psig (ambient pressure test) after the flows were established. Data acquisition through *PTGACQ* software was then commenced.

Stage 2: Temperature ramp of 10°C/min - RG: H₂, FG: N₂, PG: N₂

After the data acquisition starts, the Ar flow was stopped and H₂ flow was started and set to 190 ml/min using the Bronkhorst flow control box. Using a ramp of 10°C/min, the temperature was generally set to increase under a H₂ atmosphere until reaching a temperature of 450°C.

Stage 3: Isothermal step - RG: H₂, FG: N₂, PG: N₂

Under an H₂ atmosphere, the temperature stays constant, generally at 450°C for 450 minutes (8 hours), to allow the reduction reaction to complete.

Stage 4: Temperature ramp of -10°C - RG: Ar, FG: N₂, PG: N₂

After the isothermal step, the H₂ flow was stopped, Ar flow was started, and the temperature decreased. Data acquisition was stopped. If a subsequent carbonylation test was to be conducted the following day, the PTGA is kept in an Ar atmosphere overnight by completely closing the low-level BPR. If the reduction experiment was the stand-alone test, the PTGA is vented to the fume hood after purging with Ar for 20 minutes.

3.3.2 Carbonylation Experiments

Carbonylation experiments were conducted on the following day of the reduction experiment. The PTGA was cooled down to room temperature overnight and kept under an Ar environment to avoid re-oxidation of the sample. A typical temperature profile for this test, segmented into four sections, is shown in Figure 3-3.

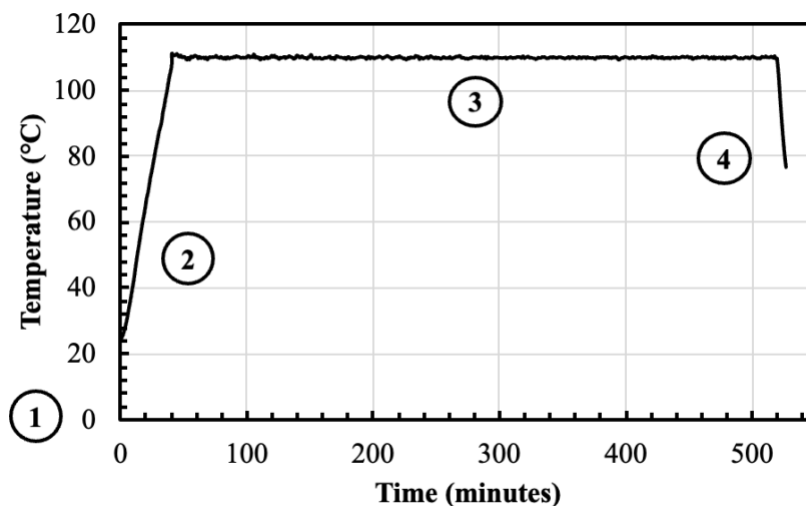


Figure 3-3: Typical temperature profile of carbonylation experiments.

Stage 1: Establishing gas flows and pressurizing the reactor – RG: Ar, FG: N₂, PG: N₂

Before introducing gases from the cylinders, the air flowrate was set to 15 L/min. The decomposition furnace was turned on and set to a temperature of 500°C for carbonylation experiments. The N₂ flow was

initiated and the flowrates for the PG and FG were set to 800 ml/min through the OMEGA FM control box. The Ar RG flow was initiated, and the flowrate was set to 800 ml/min. The high-level BPR was used to maintain the PTGA pressure at either 150 psi or 450 psi for pressurized carbonylation tests after the flows were established. Data acquisition through *PTGACQ* software was then commenced. When the pressure of the PTGA was steady at the desired level, the flowrates of Ar and N₂ were reduced to 200 ml/min.

Stage 2: Temperature ramp of 2°C/min - RG: CO, FG: N₂, PG: N₂

The Ar flow was stopped, and CO flow was initiated and set to 190 ml/min using the Bronkhurst flow control box. The background for the FTIR was collected under a CO atmosphere. After the background was collected, FTIR and PTGA data acquisition commenced through their respective software. Using a ramp of 2°C/min, the temperature was generally set to increase under a CO atmosphere until reaching a temperature of 110°C.

Stage 3: Isothermal step - RG: CO, FG: N₂, PG: N₂

Under a CO atmosphere, the temperature stays constant, generally at 110°C for 480 minutes (8 hours), to allow a high carbonylation extent.

Stage 4: Temperature ramp of -10°C - RG: Ar, FG: N₂, PG: N₂

After the isothermal step, the CO flow was stopped, Ar flow was started, and the temperature decreased back to room temperature at a rate of -10°C/min. Data acquisition was stopped. After 20 minutes of flowing Ar through the reactor (to ensure all the residual carbonyls and unreacted CO have been purged), the PTGA is slowly vented to the fume hood and depressurized.

3.4 Characterization Techniques and Data Analysis

3.4.1 PTGA

Thermogravimetric analysis is a widely used thermal analysis technique that measures changes in mass for a loaded sample over a given temperature and pressure range under specified environmental conditions. The working principle of a PTGA is based on the detection of mass variations as a result of physical or chemical changes to a sample. The PTGA used in this study was the Cahn TG 151. The PTGA system consisted of a pressure balance, furnace vessel, stand, and elevator. The pressure balance vessel was constructed from solid 316 stainless steel and is designed to operate at a pressure range of 1.9×10^{-7} psig to 1500 psig at ambient temperature. The pressure balance has a closed-loop servo network which automatically compensates for the weight changes in the sample. The electrical current required to return the balance beam to its null position is directly proportional to the weight. This is a null balance, so the reference sample always remains in a uniform temperature zone. The furnace vessel, also constructed from 316 stainless steel, was designed to operate up to 1000°C at 1000 psig. An internal quartz tube separated the reaction chamber from the furnace. A joint coupling ring was used to seal the furnace vessel to the pressure balance. The sample was loaded in the furnace by opening the coupling ring and lowering the furnace vessel using the elevator.

The output of the thermo-gravimetric analyzer was a mass-loss curve with respect to time, indicating the loss of mass due to the removal of water and oxygen during reduction experiments and the evolution of nickel carbonyl during carbonylation experiments. The raw data for mass was normalized for both types of experiments, such that data across different samples and conditions can be compared on the same basis.

For reduction, a normalized conversion can be obtained by applying Equation 3-1 to the raw mass data obtained from the PTGA software. By subtracting the final mass of the solid from the initial sample mass in the denominator, the conversion is normalized to a scale of 0 to 1.

$$\text{Normalized Conversion (X)} = \frac{m_0 - m_t}{m_0 - m_r} \quad \text{Equation 3-1}$$

Where m_0 (mg) is the initial mass of the sample before reduction, m_t (mg) is the mass at time t , and m_r (mg) is the final mass of the solid after reduction.

A mass loss fraction provides insight into the amount of mass that has decreased with respect to only the initial mass. This can be calculated through Equation 3-2.

$$\text{Mass Loss Fraction} = \frac{m_0 - m_t}{m_0}$$

Equation 3-2

Where m_0 (mg) is the initial mass of the sample before reduction, and m_t (mg) is the mass at time t

Figure 3-4a presents a mass loss curve for a reduction test with the B1-MHP sample as obtained from the PTGA instrument and Figure 3-4b presents the normalized conversion after applying Equation 3-1 to the raw mass data.

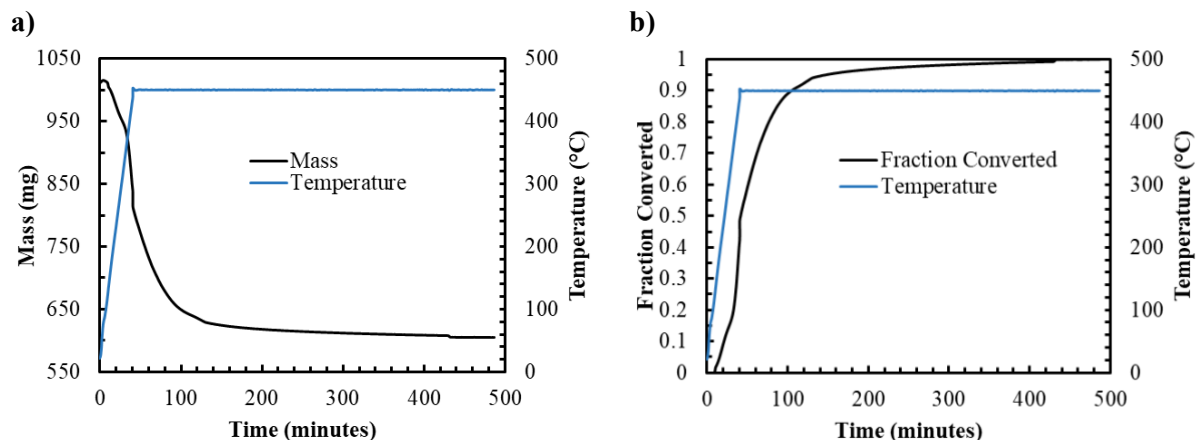


Figure 3-4: a) A reduction curve for B1-MHP at 450°C showing mass loss and temperature profile against time, and b) normalized fraction converted and temperature profile against time.

During the first 40 minutes, when the temperature ramps to 450°C at a rate of 10°C, the trapped moisture within the sample is released and the metallic hydroxides are decomposed to form water vapour and metallic oxides. As the temperature approaches the setpoint of 450°C, reduction begins and the kinetics shift. During the dehydration step (from 0 to 40 minutes), it is assumed that only the removal of free water (trapped moisture) and water released from the decomposition of the hydroxide contributes to the loss of mass. This assumption can be validated through ICP analysis of the fresh B1-MHP sample, which indicates that the balance of the B1-MHP composition after considering all metallic components (i.e. the moisture content and bonded -OH groups) is 44 wt.%. This also agrees with the fraction converted after the first 40 minutes, shown in Figure 3-4a. Furthermore, as discussed in section 2.6.1, Pöyhtäri et al. [39] saw a 26.9% mass loss (a fully dried sample with no trapped moisture) associated with the decomposition of $\text{Ni}(\text{OH})_2$ under an inert PTGA environment at 500°C.

During the reduction step (from 40 to 500 minutes), it is assumed that the main contributor to mass loss is the loss of oxygen from the NiO reduction reaction. This assumption is made because Ni is the main metallic

element in the four samples (ranging from 32.44 to 46.66 wt.%), while no other metals have a concentration greater than 5% in any of the samples (except for B2-MHP, consisting of 11.7% cobalt and 10.6% Manganese). Co(OH)_2 is known to take two forms, referred to as α - and β -form, and can be produced with different morphologies via chemical precipitation from aqueous solution. β - Co(OH)_2 is more stable and starts to decompose to the oxide form at 200°C, whereas α - Co(OH)_2 decomposes at 130°C under a nitrogen atmosphere [58]. Based on the precursor, the product of the decomposition can be either Co_3O_2 or CoO . CoO begins to reduce under a pure H_2 atmosphere at 300°C [59] and Co_3O_2 was fully reduced to metallic Co in 50 minutes at 300°C [60]. Mn(OH)_2 will also decompose at temperatures of 450°C, but studies have shown that the reduction of MnO_2 powder begins at 305°C under an Ar- H_2 atmosphere, but complete reduction to MnO occurs at 610°C, and no further reactions are observed at elevated temperatures [61]. With this, there will be a minor error when estimating the degree of nickel reduction for the B2-MHP sample, as the decomposition and subsequent reduction of cobalt and manganese hydroxides may contribute to the mass loss to some extent.

Carbonylation curves (raw PTGA data for mass loss) can be normalized by relative mass (%) against time, as shown by Equation 3-3. Figure 3-5 shows the construction of the relative mass percentage curve from raw data through this equation. During carbonylation experiments, the extraction of Ni can be expected to be the main contributor to the observed mass loss, since the conditions are too moderate for the extraction of cobalt and manganese. $\text{Co}_2(\text{CO})_8$ (dicobalt octacarbonyl) is known to form at moderate pressures, yet the exact conditions of synthesis through carbonylation remain unknown. For the formation of $\text{Mn}_2(\text{CO})_{10}$ (dimanganese decacarbonyl), a slurry of MnI_2 , Cu, and magnesium metal powder is reacted with CO gas at a pressure of 3000 psig [62]. Due to the elevated pressures and complexity of processes required for the synthesis of $\text{Co}_2(\text{CO})_8$ and $\text{Mn}_2(\text{CO})_{10}$, they are unlikely to have a significant effect on the mass loss from the carbonylation experiments carried forward at relatively moderate conditions. However, to present the data accurately, the results are presented as a mass percentage relative to the initial sample mass before carbonylation.

$$\text{Normalized mass (\%)} = \frac{m_t}{m_r} \times 100 \quad \text{Equation 3-3}$$

Where m_t (mg) is the mass at time t , and m_r (mg) is the final mass of the solid after reduction (used as the initial mass for the subsequent carbonylation experiment)

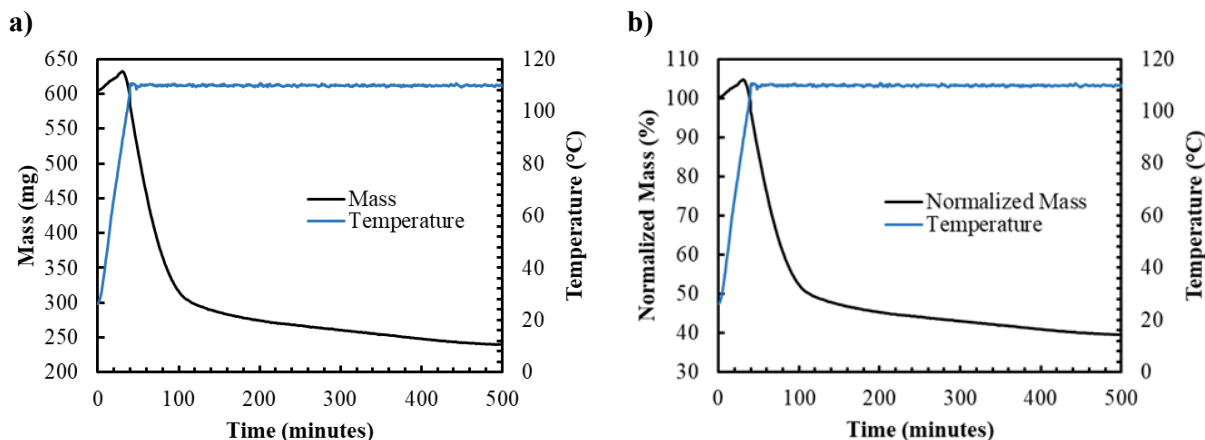


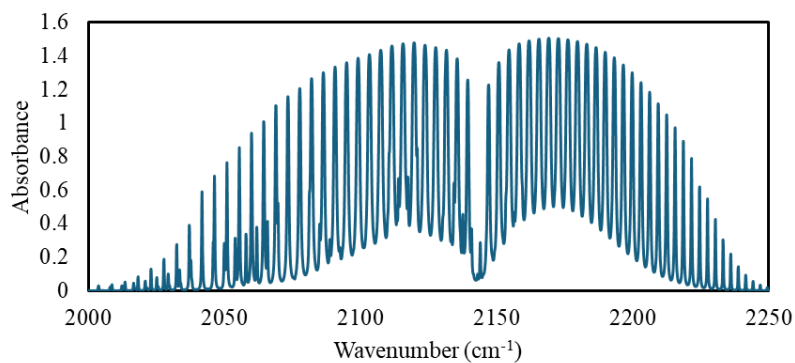
Figure 3-5: a) The carbonylation curve for B1-MHP at 110°C and 450 psig showing mass loss and temperature profile against time and b) Normalized Mass (%) for the same experiment against time.

The increase in mass during the first 30 minutes, as seen by Figure 3-5, is due to the adsorption of CO gas molecules on the surface Ni sites. After the available sites are saturated, the formation of $\text{Ni}(\text{CO})_4$ starts to occur, causing the mass loss seen from 30 minutes to 500 minutes. When constructing Figure 3-5b, the mass values were normalized to the initial mass of the solid before the carbonylation experiment, m_r .

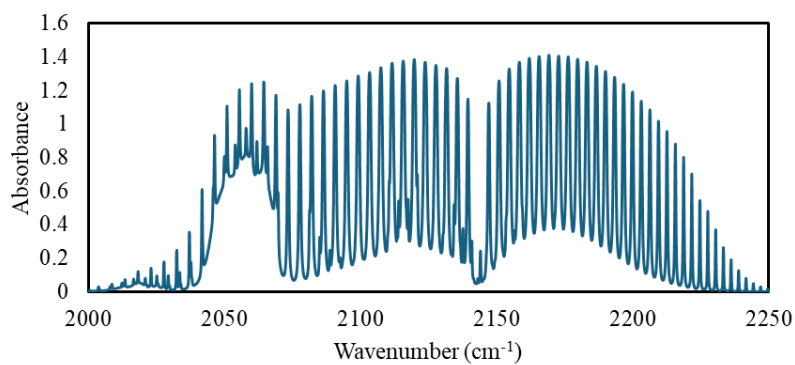
3.4.2 FTIR

The FTIR used in this project was the Varian 640-IR, with a gas cell of a 10 cm path length. It was used as an inline process gas detector, which allowed for the detection of water vapour produced during reduction tests and CO reactant gas and Ni(CO)₄ that were produced during carbonylation tests. During the carbonylation experiments, the off-gas from the PTGA consisted of small concentrations of Ni(CO)₄ in CO gas. An FTIR spectrum of pure CO gas (fed to the PTGA at a pressure of 450 psig and a flow rate of 200 ml/min) is shown in Figure 3-6a, which spans from wavenumbers 2000 cm⁻¹ to 2250 cm⁻¹. Initially, a background spectrum was collected under argon flow, which was automatically subtracted from the sample measurements to isolate the absorbance features of newly formed species. The IR peak of nickel carbonyl vapour occurs at a wavenumber of 2057 cm⁻¹, and so an interference was observed during carbonylation due to the overlapping absorption bands of CO and Ni(CO)₄, shown in Figure 3-6b. To resolve this issue, separate background experiments were conducted by flowing pure CO at 150 psig and 450 psig and a flow rate of 200 ml/min through the flow system in the absence of any reactive solid in the PTGA. The CO spectrum was automatically subtracted from the sample measurements to isolate the Ni(CO)₄ IR peak, shown in Figure 3-6c. During carbonylation, the IR peak corresponding to Ni(CO)₄ became saturated generally within the first 30 minutes of the experiment. As a result, it was not possible to perform the quantification of the Ni(CO)₄ peaks throughout the carbonylation experiments. Hence, the FTIR was used to detect the presence of carbonyls instead. The input parameters to the Varian FTIR software are presented in Table 3-6.

a)



b)



c)

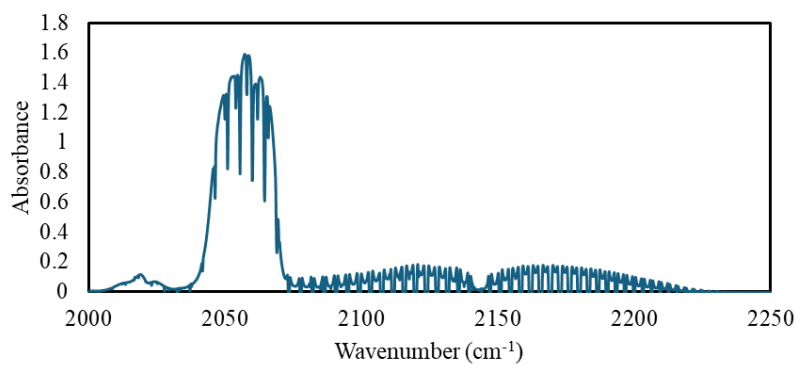


Figure 3-6: Results of a) IR spectrum of pure CO gas at a pressure of 450 psig and a flow rate of 200 ml/min, b) IR spectrum of overlapping CO and Ni(CO)₄ absorption bands during carbonylation production, and c) Saturated Ni(CO)₄ peak at 2057 cm⁻¹ wavenumber without overlap of CO absorption band when using a background spectrum with CO.

Table 3-6: Input parameters for the Varian 640-IR instrument software.

| Kinetics | |
|--------------------|---|
| Time resolution: | 50 seconds |
| Length of run: | 600 minutes |
| Electronics | |
| Speed: | 5 kHz |
| Filter: | 2.56 kHz |
| Resolution: | 0.25 cm ⁻¹ |
| Optics | |
| IR source: | Mid-infrared (MIR) |
| Beam: | Internal |
| Detector: | Mercury Cadmium Telluride (MIR) broadband |

3.4.3 ICP

ICP-OES is an analytical technique used for the detection and quantification of chemical elements. The ICP instrument in this research project was Prodigy High Dispersion ICP by Teledyne Labs and was set up to analyze the elemental composition of aqueous samples in the concentration range of 5 mg/L to 100 mg/L. To create aqueous samples, the solid pellets were first crushed into a fine powder. 50 mg of each solid sample was digested using 8 mL of aqua regia solution. Aqua regia is a 1:3 (volume/volume) mixture of concentrated nitric acid (HNO₃, ≤ 70 %) and hydrochloric acid (HCL, ≤ 37 %). Once the solids were visibly seen to be digested, the acidic solution was diluted with deionized water (DI) to a volume of 50 mL. If the anticipated concentration of an element was outside the detection range of the ICP instrument, the 50 mL solution was diluted with DI by a factor. Each solution was subjected to vacuum filtration to remove any suspended solids. The aqueous samples were then brought to the ICP analysis instrument, where they were introduced from the digestion tube to the instrument using a peristaltic pump. A nebulizer using high-speed flow of argon contacts the liquid and shatters small liquid droplets into aerosol. After the removal of larger droplets in a spray chamber, the aerosol is transported to the plasma. The emitted light is transferred to the diffraction grating using transfer lenses, and the light is separated into its component wavelengths in the

optical spectrometer. The intensity of emissions from different wavelengths is directly proportional to the concentrations of elements in the sample. The ICP analysis output was the concentration of the element(s) of choice in the diluted aqueous solution. To calculate the mass fraction of the desired element within the analyzed sample, Equation 3-4 was used. From the ICP analysis of fresh samples and residual samples of carbonylation, the extraction efficiency per element was determined using Equation 3-5.

$$x_i = \frac{C_{i,ICP} \times D_F \times 0.05 \text{ L}}{m_{\text{digested}}} \quad \text{Equation 3-4}$$

Where x_i is the mass fraction of element, i , $C_{i,ICP}$ (mg/L) is the diluted concentration of element, i , obtained from ICP analysis, D_F is the dilution factor, and m_{digested} (mg) is the total initial mass of the sample that was digested (generally around 50 mg).

$$E_i(\%) = \frac{m_o x_{o,i} - m_c x_{c,i}}{m_o x_{o,i}} \times 100 \quad \text{Equation 3-5}$$

Where $E_i(\%)$ is the extraction efficiency of element, i , m_o (mg) is the mass of the fresh sample before the reduction experiment (measured by a table mass balance), $x_{o,i}$ is the mass fraction of element, i , in the fresh sample (measured by ICP analysis), m_c (mg) is the mass of the residue after carbonylation (measured by a table mass balance), and $x_{c,i}$ is the mass fraction of element, i , in the residue after carbonylation (measured by ICP analysis).

The error in the measured concentration through ICP analysis was 1.25%, which was a combination of the method's uncertainty (i.e., uncertainty in the initial measured mass and dilutions) and variations in the instrument.

3.4.4 BET

The Micrometrics ASAP 2020 instrument was used to take surface area measurements using the (BET) method and pore characteristic measurements using the Barrett-Joyner-Halenda (BJH) method. Before the analysis, the surface of the sample was degassed (cleared of adsorbed gases and water) under a vacuum system at elevated temperatures using the same instrument. After the degassing step, the sample was transferred to the analysis port. The surface area analyzer measures the amount of probing gas (N_2) that is adsorbed onto the sample surface at different relative pressures. Adsorption and desorption isotherms are created using the BET method, from which the surface area can be determined.

Table 3-7: Input parameters to the ASAP 2020 software during the degas and analysis steps.

| Degas - Evacuation Phase | |
|---|-----------------------|
| Temperature ramp rate: | 10°C/min |
| Target temperature: | 90°C |
| Evacuation rate: | 10 mmHg/s |
| Unrestricted evacuation from: | 10 mmHg |
| Vacuum setpoint: | 500 µmHg |
| Evacuation time: | 10 minutes |
| Degas - Heating phase | |
| Ramp rate: | 10°C/min |
| Hold temperature: | 250°C |
| Hold time: | 300 minutes |
| Adsorptive Properties | |
| Gas: | N ₂ |
| Thermal translational hard sphere diameter: | 0.386 nm |
| Molecular cross-sectional area: | 0.162 nm ² |
| Density conversion factor: | 0.0015468 |
| Maximum manifold pressure: | 925 mmHg |

Chapter 4

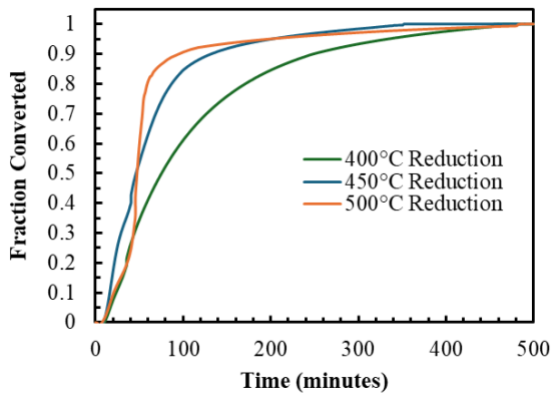
Results and Discussion

4.1 MHP Reduction

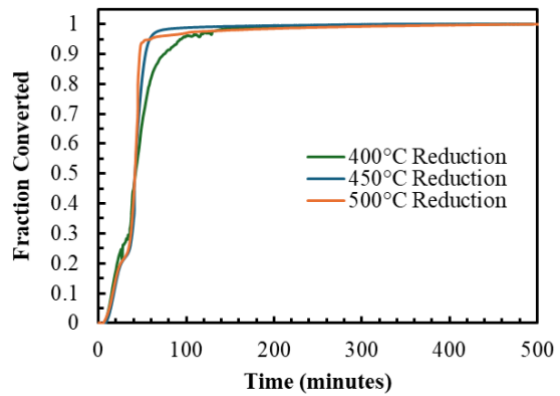
4.1.1 Effect of MHP Reduction Temperature

To investigate the reduction of MHPs, the four samples were subjected to isothermal reduction in the PTGA reactor. Reduction experiments were carried out under a hydrogen gas atmosphere (flowing at 200 ml/min) at three different temperatures – 400, 450, and 500°C. The aim was to characterize the kinetics of the reduction reaction, the fraction of reduced nickel and compare the samples. The mass loss data from the PTGA was used to calculate the fraction of reduced nickel at any given point in time, the rate of mass loss, and the final plateau of mass once the reduction has completed. This allowed for a kinetic comparison between the samples and how reduction behaviour evolves with temperature. The results are presented in Figure 4-1. The raw data for mass loss obtained from the PTGA was normalized to a fraction of Ni converted using Equation 3-1. It should be noted that even if complete conversion of Ni(OH)₂ to metallic nickel did not occur, the conversion profiles would still show the final value approaching 1, as Equation 3-1 takes into account the initial mass of the sample and the final mass after the reduction experiment was completed. To evaluate the fraction of mass loss during the reduction experiment and compare it to a theoretical value, Equation 3-2 was used. A theoretical mass loss fraction for the conversion of Ni(OH)₂ to Ni can be obtained by applying Equation 3-2 and substituting the molar mass of Ni(OH)₂ (92.71 g/mol) as m_0 , and the molar mass of Ni (58.69 g/mol) as m_t . This results in a theoretical mass loss fraction of 0.37. If the experimental mass loss fraction for any reduction experiment is less than 0.37, it indicates that the complete reduction of Ni(OH)₂ to Ni did not occur. If the experimental mass loss fraction is greater than the theoretical value, there was either a significant additional contribution to mass loss from the removal of moisture (absorbed by the sample during transport) or from the reduction of other metallic oxides. The mass loss fractions of the four MHPs after reduction are presented in Table 4-1. Nickel in MHP samples is initially present in the hydroxide form, and so the initial mass loss represents the removal of moisture in the sample, followed by the decomposition of the hydroxides in the temperature range of 210 to 280°C [39], and NiO reduction starting around 300°C, albeit at a very slow rate [40]. The rate of NiO accelerated significantly when isothermal conditions were achieved.

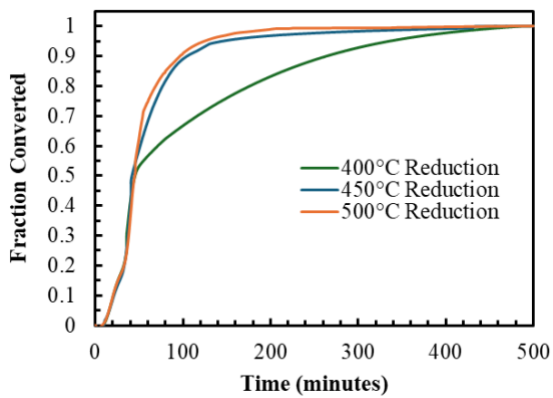
a) L1-MHP



b) L2-MHP



c) B1-MHP



d) B2-MHP

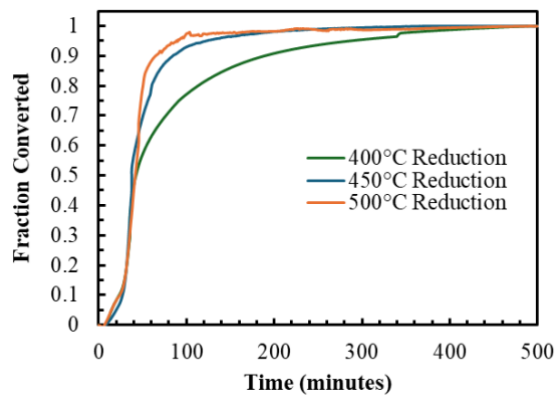


Figure 4-1: Fractional conversion during reduction under H₂ atmosphere at 6 psig and temperatures of 400°C, 450°C, and 500°C of a) L1-MHP, b) L2-MHP, c) B1-MHP, and d) B2-MHP.

Table 4-1: Mass loss fractions during the reduction of the four MHP samples at 400, 450, and 500°C.

| Sample | Mass Loss Fraction from Reduction | |
|---------------|--|------|
| L1-MHP | After 400°C reduction: | 0.32 |
| | After 450°C reduction: | 0.37 |
| | After 500°C reduction: | 0.39 |
| L2-MHP | After 400°C reduction: | 0.42 |
| | After 450°C reduction: | 0.42 |
| | After 500°C reduction: | 0.43 |
| B1-MHP | After 400°C reduction: | 0.38 |
| | After 450°C reduction: | 0.40 |
| | After 500°C reduction: | 0.42 |
| B2-MHP | After 400°C reduction: | 0.28 |
| | After 450°C reduction: | 0.29 |
| | After 500°C reduction: | 0.30 |

Figure 4-1a shows that there is an improvement in the L1-MHP reduction kinetics with each increment of temperature increase. 100 minutes after the introduction of H₂ gas, the conversion fraction at 400°C was 0.61, whereas a fraction of 0.84 and 0.91 was achieved at 450°C and 500°C, respectively. It took 250 minutes to achieve a 0.9 conversion fraction at 400°C; that time was decreased to 130 minutes at 450°C and 95 minutes at 500°C. Particularly for reduction at 400°C and 450°C, the rates of Ni(OH)₂ decomposition (predominantly occurring in the first 40 minutes while the temperature ramps to the isothermal condition setpoint) were the slowest among the four samples. L1-MHP has the highest content of structurally bound hydroxide groups and crystalline water, which necessitates additional energy for dehydration, yielding slower kinetics during the initial temperature ramp phase. The data in Table 4-1 shows that, at 450°C, the final mass loss fraction agrees with the theoretical fraction associated with the complete conversion of Ni(OH)₂ to metallic Ni (which is 0.37). A steady increase of mass loss fraction from 0.32 to

0.37 to 0.39 is observed as the reduction temperature in each experiment was increased, indicating that the reduction temperature has a positive effect on NiO reduction, also seen by the reduction conversion curves. Comparing the two MHPs derived from laterite ore, the reduction temperature had a much more pronounced effect on the conversion of Ni in L1-MHP as compared to L2-MHP. Figure 4-1b shows very minimal changes in the reduction kinetics of L2-MHP at the various temperatures; however, they were much more rapid as compared to L1-MHP. After 100 minutes of the introduction of H₂ gas, the conversion fractions were 0.96, 0.99, and 0.97 at 400, 450, and 500°C, respectively. The improvement in reduction kinetics from L1-MHP to L2-MHP correlates with the initial Ni content in the samples, which increases from 32 wt.% to 42.6 wt.% between L1 and L2-MHP fresh samples. The greater nickel content translates to a higher number of NiO sites available for reaction with H₂ gas and hence results in faster kinetics. The conversion curves completely plateau for L2-MHP, indicating that an increase in reduction time would not yield further improvement in conversion. The data for L2-MHP in Table 4-1 shows that the reduction mass loss fraction across the three temperatures stays fairly constant, 0.42 at 400°C and 450°C, and 0.43 at 500°C. The conversion data presented in Figure 4-1 b) agrees with the trend of reduction temperature having minimal effect on reduction rate and kinetics. The effect of Co(OH)₂ dehydration and subsequent reduction on mass loss fraction would be more prominent for L2-MHP, as the fresh sample has a Co concentration of 5.1 wt%, compared to 2.5% in L1-MHP. As a result, the overall mass loss fractions are greater than those of L1-MHP.

Figure 4-1c shows that for B1-MHP, there is a positive effect of increasing the reduction temperature from 400°C to 450°C on reduction kinetics, but a very minimal effect when the reduction temperature is increased from 450°C to 500°C. 100 minutes after introducing H₂ gas, the conversion fractions were 0.67, 0.89, and 0.91 for the reduction temperatures of 400°C, 450°C, and 500°C, respectively. Compared to the L1-MHP conversions fraction at 400°C and 450°C, B1-MHP showed higher conversions at these temperatures. A common factor between L2-MHP and B1-MHP is the high Ni content in the fresh sample (48.1 wt.% Ni in fresh B1-MHP) as compared to L1-MHP. This, combined with the fact that B1-MHP has a hydroxide and crystalline water content of 15 wt.% less than that of L1-MHP, causes the B1-MHP kinetics to be faster at lower temperatures. The reduction mass loss fractions increase from 0.38 to 0.40 to 0.42 as the reduction temperature increases in each experiment. A reduction temperature of 450°C was optimal for B1-MHP, because even though the mass loss fraction at this temperature was slightly higher than the theoretical value of 0.37 for Ni(OH)₂ to Ni conversion, the rate of reduction was significantly improved over the 400°C condition.

Consistent with B1-MHP, the kinetics for B2-MHP become faster when the reduction temperature was increased from 400°C to 450°C. However, the increase to 500°C caused minimal change in kinetics. 100 minutes after introducing H₂ gas, the conversion fractions were 0.77, 0.93, and 0.97 for the reduction temperatures of 400°C, 450°C, and 500°C, respectively. Although fresh B2-MHP has a Ni content (32.4 wt.%) that is similar to L1-MHP, the content of hydroxides/crystalline water is 18 wt.% less, which results in a higher reaction rate corresponding to Ni(OH)₂ dehydroxylation in the first 40 minutes for all three reduction temperatures. Although the fraction converted curves presented in Figure 4-1d approach a value of 1 at the end of the reduction experiment, the mass loss fractions for B2-MHP provide a contradicting conclusion. B2-MHP had the lowest mass loss fractions after reduction, 0.28, 0.29, and 0.30 after reduction at 400°C, 450°C, and 500°C, respectively, indicating that complete conversion of Ni(OH)₂ did not occur with this sample at any of the temperatures. A significant differentiator between fresh B2-MHP and the other samples is the high initial Co concentration of 11.7 wt.%. At specific loadings and reaction conditions, cobalt is known to influence the reduction behaviour of NiO. An experimental study was conducted by Dzakaria et al. [63] in which doped NiO with Co at a 3 wt.% and 10 wt.% level. They then conducted reduction experiments in H₂ atmosphere at 500°C of the two doped samples along with pure NiO to obtain overall conversion. It was found that the 10% Co/NiO sample was 87.9% converted to Ni, the 3% Co/NiO sample was 93.7% converted and pure NiO was 97% converted. However, 100% conversion for all three samples was achieved at a reduction temperature of 700°C [63]. In this project, the Co concentration was very similar to the 10% Co/NiO sample used by Dzakaria et al. [63], along with the type of reducing gas used, and the reduction temperature. This points to the conclusion that Co played a role in hindering NiO reduction and caused the reduction mass loss fractions for B2-MHP to be less than the theoretical value.

4.1.2 BET Surface Area and Pore Diameter Results for Reduction Residues

After reduction at 400, 450, and 500°C of the four MHPs, BET analysis was conducted on the solid residues using nitrogen adsorption and desorption to determine the specific surface area and average pore diameter. This analysis was used to gain insight into the changing microstructure of the MHP pellets during reduction, and also the effect on the subsequent carbonylation reaction and overall Ni extraction. The BET surface area and average pore diameter results are presented in Table 4-2. A significant point of consideration while conducting BET analysis directly after reduction is the potential for re-oxidation of the reduced metal when exposed to ambient air during the process. A study on the kinetics of the oxidation of reduced metals in the air at room temperature by Nabey et al. [64] used EDX analysis to determine oxygen uptake percentage at various exposure times of metals in ambient air. They showed that reduced Ni (at a 99.7% purity) absorbed

only 0.035% oxygen (compared to the initial sample mass) when exposed to air for 10 hours, and the oxygen formed a thin film on the metallic surface [64]. Although the kinetics of oxidation of Ni at room temperature in air are very slow, it should be noted that the measured BET surface areas and pore diameters may reflect the effects of slight surface oxidation during sample transfer.

Table 4-2: BET surface area and average pore diameter results for fresh MHP pellets and residues after reduction at 400, 450, 500°C.

| Sample | BET Surface Area (m²/g) | | Average Pore Diameter (nm) | |
|---------------|---|-------|-----------------------------------|------|
| L1-MHP | Fresh pellet: | 2.2 | Fresh pellet: | 11.4 |
| | After 400°C reduction: | 90.5 | After 400°C reduction: | 4.7 |
| | After 450°C reduction: | 46.7 | After 450°C reduction: | 6.8 |
| | After 500°C reduction: | 57.6 | After 500°C reduction: | 9.5 |
| L2-MHP | Fresh pellet: | 26.3 | Fresh pellet: | 4.0 |
| | After 400°C reduction: | 39.6 | After 400°C reduction: | 14.7 |
| | After 450°C reduction: | 32.8 | After 450°C reduction: | 13.5 |
| | After 500°C reduction: | 26.1 | After 500°C reduction: | 10.8 |
| B1-MHP | Fresh pellet: | 201.9 | Fresh pellet: | 2.6 |
| | After 400°C reduction: | 104.7 | After 400°C reduction: | 2.9 |
| | After 450°C reduction: | 68.5 | After 450°C reduction: | 5.8 |
| | After 500°C reduction: | 70.8 | After 500°C reduction: | 7.3 |
| B2-MHP | Fresh pellet: | 118.0 | Fresh pellet: | 5.1 |
| | After 400°C reduction: | 26.2 | After 400°C reduction: | 15.0 |
| | After 450°C reduction: | 20.5 | After 450°C reduction: | 14.7 |
| | After 500°C reduction: | 14.5 | After 500°C reduction: | 7.2 |

BET analysis of the fresh pellets reveals that black mass-derived samples have higher initial specific surface areas (B1-MHP: 201.9 m²/g, B2-MHP: 118.0 m²/g) compared to laterite-derived samples (L1-MHP: 2.2 m²/g, L2-MHP: 26.3 m²/g). The removal of oxygen from the NiO lattice structure is known to create a more porous, metallic structure. However, the exact structure of the product Ni lattice, along with porosity, is dependent on the properties of the precursor material [46]. The higher initial surface area for black mass-derived samples can be crucial for enhancing the availability of reactive sites for hydrogen interaction.

After reduction at 400°C, L1-MHP exhibited an increase of surface area from 2.2 m²/g to 90.5 m²/g, and a corresponding pore diameter shift from 11.4 nm to 4.7 nm. The increase in surface area signifies the formation of micro-porous (pores with a diameter less than 2 nm) and meso-porous (pores with a diameter between 2 nm and 50 nm) structures from the removal of the bonded hydroxides and oxygen from the NiO lattice. After reduction at 450°C, the surface area decreases to 46.7 m²/g, suggesting that the product Ni is partially sintered at higher temperatures in L1-MHP. After the fresh pellet experiences an initial decline in pore diameter from the 400°C reduction, the pore diameter showed a proportional relationship with the reduction temperature, steadily increasing to 9.5 nm at 500°C. The surface area of L2-MHP moderately increased from 26.3 m²/g to 39.6 m²/g, but to a lesser extent compared to L1-MHP. The surface area continued to decrease with an increasing reduction temperature, similar to L1-MHP. L2-MHP exhibited an immediate increase in pore diameter at 400°C, from 4.0 nm to 14.7 nm, followed by a gradual decrease at higher temperatures. This suggests that a direct relationship between BET surface area and pore diameter cannot be applied across the samples, and there are large variations in fresh sample compositions affecting the microstructure after reduction.

In contrast, black mass-derived samples exhibited initial declines in surface area after reduction at 400°C (B1-MHP: 201.9 m²/g to 104.7 m²/g, B2-MHP: 118.0 m²/g to 26.2 m²/g). The trend continues at elevated temperatures, where both samples exhibited a reduction in surface areas. This suggests that the black mass-derived samples undergo thermally induced sintering and structural densification at a lower temperature (400°C) compared to laterite-derived samples. Solely analyzing the black mass MHP pellets, the surface area is greatest in the fresh samples as compared to the reduction residues, which also correlates with the pore diameter being the smallest. However, B1-MHP experiences pore coarsening at elevated temperatures, whereas the microstructure of B2-MHP becomes denser. The additional content of Co and Mn may play a role in hindering the formation of larger mesopores in B2-MHP.

4.1.3 Kinetic Modelling of MHP Reduction at Different Temperatures

To obtain a comprehensive understanding of the reduction behaviour observed for the MHP samples, experimental NiO conversion data for the L1-MHP and B1-MHP samples obtained from the PTGA were systematically fitted to established kinetic models presented by Pöyhtäri et al. [39]. These two samples were chosen because they exhibited the largest variation in reduction behaviour across the three temperatures. The aim was to determine the predominant kinetic regime applicable to each sample, analyze the shift of regime across the reaction time/reduction temperature, and draw conclusions for trends in BET surface area and pore diameter. Three classes of kinetic models were considered for this analysis, as also presented in the literature review section 2.6.4:

1. Avrami-Erofeev (AE) nucleation-growth models (Equation 2-15):

Where k is the apparent reaction rate constant, x is the fractional conversion of NiO (wt.%), t is the reaction time, and n is the Avrami exponent that reflects nucleation and growth dimensionality. Models with $n = 1, 2, 3$ were fit to experimental data.

2. Geometric contraction (phase-boundary) models (Equation 2-16):

Where n was varied again ($n = 1, 2, 3$) to examine different scenarios of phase-boundary reactions (i.e. the dimensionality of contraction).

3. Diffusion-based kinetic models (Equation 2-17, Equation 2-18, Equation 2-19):

Where the 1-D diffusion (D1), 2-D Valensi diffusion model (D2), and the 3-D Jander diffusion model (D3) were considered.

For each kinetic model and temperature, the rate constant, k , was estimated by rearranging the model equation to express conversion, x , as a function of time, t . A non-linear least squares optimization was performed by minimizing the sum of squared differences between the model-predicted conversions and the experimental conversions at each time point. This allowed for a best-fit estimation of the reaction rate constant. During the kinetic fitting procedure, the data analysis was initiated after isothermal conditions were achieved in the experiment; data points from time $t = 40$, $t = 45$, and $t = 50$ minutes onwards were used for reduction experiments at temperatures of 400°C, 450°C, and 500°C, respectively. From the start point of each data set, 100 minutes of reduction reaction time were considered for the kinetic fitting analysis. Restricting the data sets to these extents excluded conversion data influenced by the dehydration of the metallic hydroxides (during the temperature ramp-up phase) and ensured a closer fit to kinetic models near

the end of the reaction period. The results of the kinetic model fitting to the conversion data for L1-MHP and B1-MHP are presented in Figure 4-2. Although all the kinetic models mentioned above were fit to experimental conversion data, only the best-fitting kinetic models per mechanism were plotted to ensure adequate readability and comparison between them.

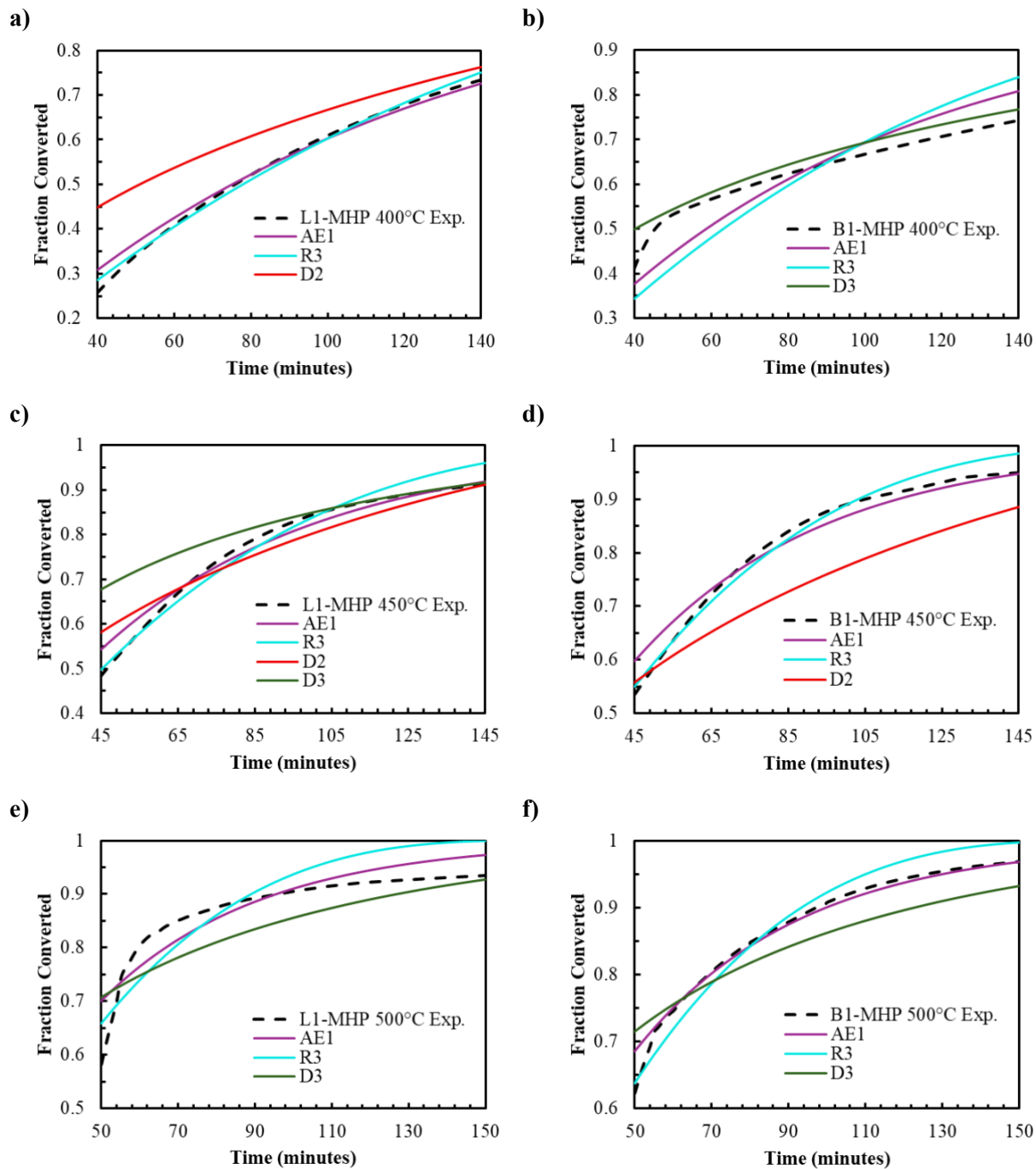


Figure 4-2: Kinetic model fitting to experimental reduction conversion for a) L1-MHP at 400°C, b) B1-MHP at 400°C, c) L1-MHP at 450°C, d) B1-MHP at 450°C, e) L1-MHP at 500°C, and f) B1-MHP at 500°C.

For reduction experiments at 400°C, the kinetic fitting results are shown in Figure 4-2a and Figure 4-2b and they provide different conclusions between L1-MHP and B1-MHP. The AE1 model and R3 model both align very closely with experimental data for L1-MHP, suggesting that nucleation-controlled and phase-boundary-controlled reactions describe the reaction to a reasonable degree. The D2 model was a poor fit at this temperature, indicating that diffusional limitations are likely minimal under these conditions. However, the diffusion-based kinetic model was most accurate in describing the reduction behaviour of B1-MHP. Except for the fit to experimental data from 40 to 50 minutes, the D3 model was able to predict NiO conversion more accurately than the AE1 and R3 models. The difference in the most appropriate kinetic mechanism for the laterite-based MHP compared to the black mass-based MHP can be attributed to their respective shifts in surface area and pore diameter after reduction at 400°C. L1-MHP surface area increases from 2.2 m²/g to 90.5 m²/g but B1-MHP decreases from 201.9 m²/g to 104.7 m²/g. The B1-MHP pellet experienced a massive surface area reduction initially, and the average pore diameter was only 62% of L1-MHP at 400°C. These two characteristics of the B1-MHP pellet microstructure may have contributed to significant intra-particle diffusional limitations for H₂ gas and the product H₂O.

At 450°C reduction, the AE1 and R3 models continued to represent the experimental conversion data most accurately for L1-MHP across the considered 100-minute period, shown in Figure 4-2c. The fit of the D3 model noticeably improved for L1-MHP from 400°C to 450°C in the latter stages of reduction (from 100 to 145 minutes). The D2 model also approaches experimental conversion during the latter reaction times, suggesting that the onset of internal pellet structural changes (such as evolving pore channels and decreasing surface area) at 450°C can be described well by diffusion-based models if the conversion is further extrapolated into latter reaction times. For B1-MHP, the fit of the D3 model became less representative of the actual conversion at 450°C; this can be correlated to the average pore size increasing from 2.9 nm at 400°C to 5.8 nm at 450°C, causing less inward intra-particle diffusional limitations for H₂ and outward diffusional limitations for product H₂O. The R3 model accurately predicted conversion from 45 to 75 minutes, and the AE1 model from there onwards, as shown in Figure 4-2d.

At the highest reduction temperature (500°C), none of the kinetic models were able to accurately predict the NiO conversion in L1-MHP from 50 to 90 minutes. In particular, the experimental data exhibited a very rapid conversion rate from 50 minutes to 65 minutes, which the predicted models did not follow (shown in Figure 4-2e). The closest-fitting kinetic model for L1-MHP remained the AE1 model. Like the trends at 450°C reduction, the D3 model approaches the experimental conversion at the very end, pointing to a possible conclusion that product water retention within the sample becomes significant as the reduction

reaction nears completion, occupying pore volume and hindering the formation of metallic Ni. B1-MHP exhibited a complete shift of kinetic regime, as experimental conversion was accurately predicted by the AE1 model across the 100 minutes, shown in Figure 4-2f. The average pore diameter again increased from 5.8 nm (at 450°C) to 7.3 nm (at 500°C), further reducing the diffusional limitations of gas transport to and from the particle's microstructure.

Overall, the results from the kinetic mechanism fitting to experimental conversion data agreed with the conclusions provided by Pöyhtäri et al. [39]. They concluded that the AE models, as well as the R2 and R3 models, had the best fit to their experimental NiO conversion data. Figure 4-2b showed that the D2 model accurately predicted NiO conversion at 400°C, when the average pore diameters for the B1-MHP were the smallest. A shift in kinetic mechanism from AE/R3 models to a diffusion-based model (D2) at later stages of L1-MHP reduction was also observed. Pöyhtäri et al. [39] did not consider the D2 model for kinetic fitting, and they found that the D1 model provided a poor fit to experimental data. Since the fresh samples used by Pöyhtäri et al. [39] for reduction experiments were in powder form and consisted of a 100 mg load (as compared to pelletized samples of approximately 1000 mg in this research study), diffusional effects were less prominent in their experimental work.

4.2 MHP Carbonylation

4.2.1 Effect of MHP Reduction Temperature on Nickel Carbonylation

Earlier experiments highlighted that the temperature during hydrogen reduction of the various MHPs had notable effects on the overall mass loss fractions (Table 4-1) and the kinetics of NiO conversion. Variation in reduction temperature also resulted in evolving microstructures within the pelletized samples, characterized by shifts in BET surface area and average pore diameters (Table 4-2). The evolving structure of the sample during reduction is important as it can affect the subsequent extraction of nickel via carbonylation. The carbonylation step is sensitive to the characteristics of the precursor material. To further explore this relationship, B1-MHP was reduced three separate times at 400°C, 450°C, and 500°C. After each reduction, a subsequent carbonylation test was conducted at 450 psig and 110°C to observe the effect of reduction temperature on the Ni extraction via carbonylation. The results are shown in Figure 4-3. B1-MHP was chosen because initial carbonylation tests showed the highest Ni extraction from the sample compared to the rest. The objective was to establish correlations between the initial reduction temperature, structural characteristics of the reduced material, and the resulting Ni extraction efficiency and carbonylation rates.

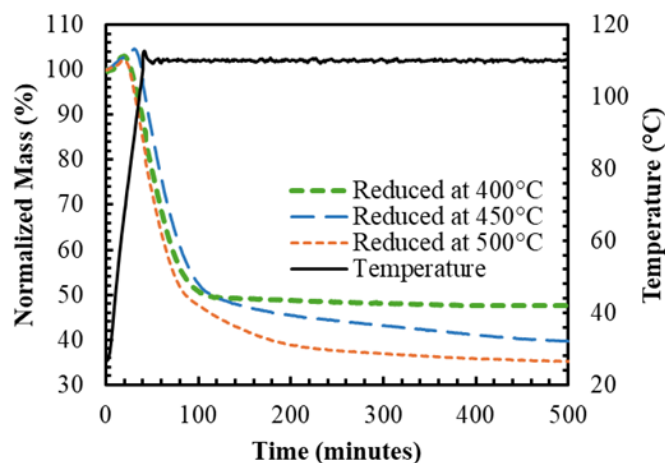


Figure 4-3: Normalized mass for carbonylation at conditions of 450 psig and 110°C for B1-MHP reduced at temperatures of 400°C, 450°C, and 500°C.

The carbonylation tests demonstrate how structural differences caused by a variation in reduction temperature influenced carbonylation behaviour. Initially, there is a short phase of approximately 40

minutes during which the normalized mass rises above 100% (when the mass relative to the initial mass increases). During this phase, the CO adsorbs onto the available metallic Ni sites. Once the Ni sites are saturated with the mono-carbonylated compound, the second and third ligands attach very quickly. With the attachment of the fourth CO ligand, the $\text{Ni}(\text{CO})_4$ molecule releases in vapour form, and Ni extraction efficiency from the sample begins. The rate of carbonylation for each sample within this set of experiments was constant until 50% normalized mass was achieved, which occurred at approximately 100 minutes of reaction time. Thereafter, the carbonylation kinetics differed, where mass loss from B1-MHP (reduced at 400°C) exhibited a sudden plateau, eventually achieving a final mass of 47% after 500 minutes. For samples reduced at 450°C and 500°C, mass loss from the carbonylation reaction continued after 100 minutes, although at significantly slower rates than before. The two respective samples achieved a final normalized mass of 39% and 34% after 500 minutes. Higher amounts of mass extraction can be expected for B1-MHP reduced at 450°C if the mass loss trend is extrapolated because it did not reach a significant plateau, in contrast to the sample reduced at 500°C. According to ICP analysis of the carbonylation residues, the total Ni extraction from B1-MHP reduced at 400, 450, and 500°C was $80.5\pm 2\%$, $95\pm 2\%$, and $93\pm 2\%$, respectively.

The improved mass loss and Ni extraction can be attributed to the structural characteristics of the pelletized sample, which are induced by higher reduction temperatures. The moderate surface area ($68.5 \text{ m}^2/\text{g}$ to $70.8 \text{ m}^2/\text{g}$) combined with substantially larger pores (5.8 nm to 7.3 nm) may have helped facilitate CO accessibility to internal metallic Ni sites, but more importantly, could have allowed for enhanced outward transport of $\text{Ni}(\text{CO})_4$ molecules from the internal sites. The $\text{Ni}(\text{CO})_4$ molecule is tetrahedral in shape, with a Ni-C bond length of 1.817 Å, whereas CO is a linear molecule with a bond length of 1.127 Å [65]. Due to its larger molecular size and coordination of four CO ligands around a single Ni atom, the outward diffusion of $\text{Ni}(\text{CO})_4$ during carbonylation becomes a more significant transport limitation compared to the inward diffusion of CO. Thesis findings underline that both surface area and pore structure of the reduced material affect Ni extraction through carbonylation. A moderate reduction temperature of 450°C was found to be an appropriate reaction condition for B1-MHP, as further increasing the temperature to 500°C did not offer additional Ni extraction. However, Ni extraction increased by 14.5% between 400°C and 450°C reduction. From a practical and scale-up standpoint, Figure 4-3 suggests that the application of the moderate reduction temperature could yield potential energy savings and capital expenditure savings (as a result of selecting reaction equipment suitable for 450°C over 500°C conditions).

4.2.2 Effect of Carbonylation Temperature

To study the effect of carbonylation temperature on kinetics and overall extraction, a series of experiments was conducted on B1-MHP. The carbonylation temperature varied from 100°C to 110°C to 120°C for B1-MHP samples reduced at 450°C. The data sets, as output by the PTGA, were converted to a normalized mass percentage (with respect to the initial sample mass before carbonylation). The results of these experiments are shown in Figure 4-4.

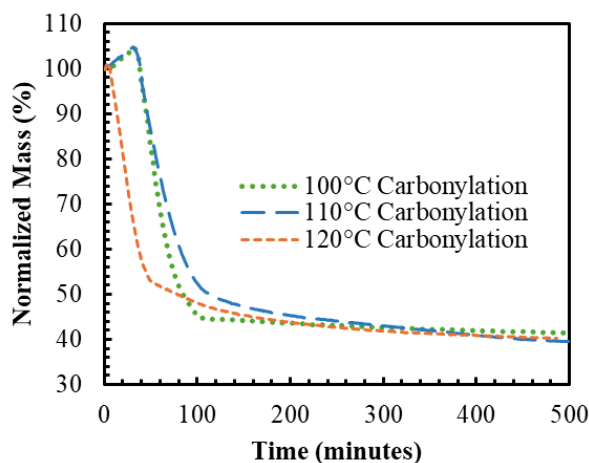


Figure 4-4: Normalized carbonylation mass at conditions of 450 psig, and varying temperatures of 100°C, 110°C, and 120°C for B1-MHP (reduced at 450°C).

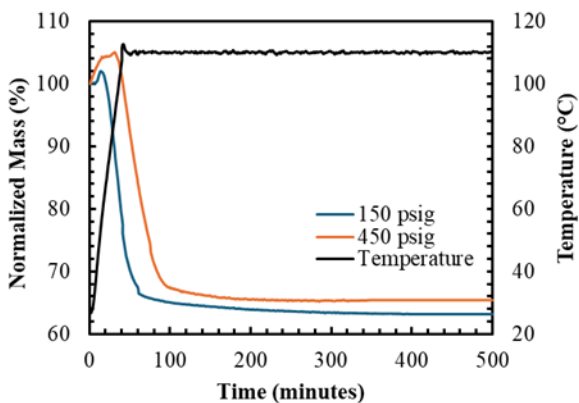
At carbonylation temperatures of 100°C and 110°C, the mass increase phase from CO adsorption took 45 minutes, and the kinetics for both temperatures were similar for the first 60 minutes. At this point, they started to deviate from each other, with the 100°C extraction achieving a significant plateau within 105 minutes. Extraction from the 110°C experiment continued, but at a much slower rate than the first 100 minutes. In contrast, carbonylation at 120°C did not exhibit any initial mass increase, indicating that the higher reaction temperature helped overcome the initial barrier to reaction between CO gas and metallic surfaces. The curve at 120°C is similar to the lower temperature extractions but essentially translated earlier by 45 minutes. The PTGA results show that extractions at all three temperatures approached a normalized mass of 40%, suggesting that the carbonylation temperature did not affect overall mass loss or Ni extraction from B1-MHP. This is further supported by ICP analysis on the carbonylation residues, which showed that the total Ni extraction from B1-MHP carbonylated at 100, 110, and 120°C was $96\pm 2\%$, $95.0\pm 2\%$, and $93\pm 2\%$, respectively. The small differences in extraction are within the margin of analytical uncertainty,

and the variability could be due to the sample heterogeneity in elemental composition (minor differences in Ni distribution between tested samples could affect ICP results).

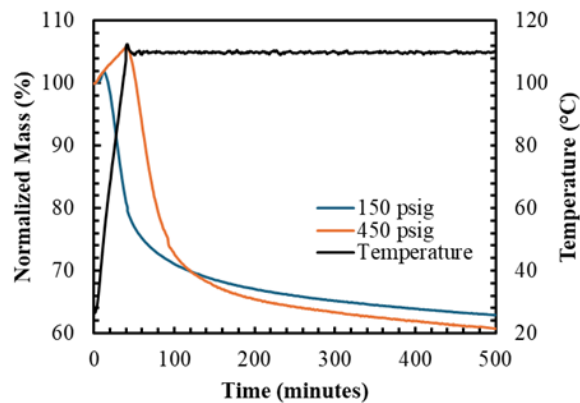
4.2.3 Effect of Carbonylation Pressure

To study the effect of CO pressure on carbonylation kinetics and Ni extraction, a series of carbonylation experiments was conducted on the four MHPs following reduction at a temperature of 450°C. Each sample was subjected to carbonylation at 110°C under two different CO pressures: 150 psig and 450 psig. The data sets, as output by the PTGA, were converted to a normalized mass percentage (with respect to the initial sample mass before carbonylation). Final Ni extraction efficiencies were quantified by ICP analysis of the fresh sample and carbonylation residue. This dual approach was adopted to compare the kinetics of carbonylation along with metal extraction efficiency in a parallel manner. Furthermore, the standalone PTGA data was not sufficient to estimate Ni extraction because cobalt carbonyl formation (specifically at higher pressures and for samples with higher Co content, such as B2-MHP) could potentially contribute to the mass loss along with nickel carbonyl. The results of normalized mass during each carbonylation test are presented in Figure 4-5 and the Ni and Co extraction efficiencies from this set of experiments are presented in Table 4-3.

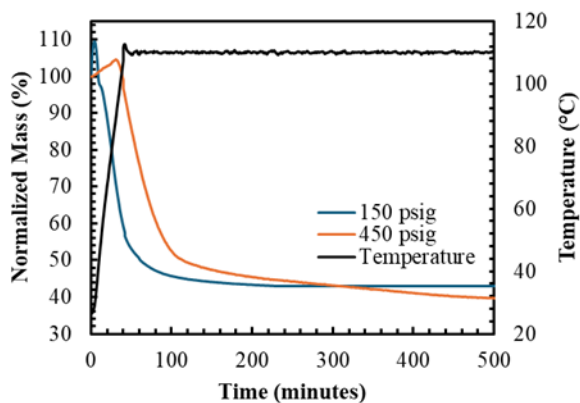
a) L1-MHP



b) L2-MHP



c) B1-MHP



d) B2-MHP

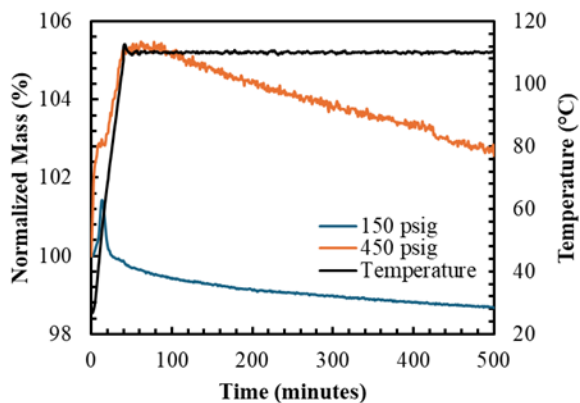


Figure 4-5: Normalized mass for carbonylation at conditions of 150 psig and 450 psig, 110°C (reduced at 450°C) for a) L1-MHP, b) L2-MHP, c) B1-MHP, and d) B2-MHP.

Table 4-3: Ni and Co extraction efficiency from ICP analysis at carbonylation conditions of 150 psig and 450 psig, 110°C (reduced at 450°C) for L1-MHP, L2-MHP, B1-MHP, and B2-MHP.

| Sample | Carbonylation Pressure | Ni Extraction Efficiency ($\pm 2\%$) | Co Extraction Efficiency ($\pm 2\%$) |
|---------------|-------------------------------|--|--|
| L1-MHP | 150 psig | 77 % | ~ 0 % |
| | 450 psig | 78 % | 4 % |
| L2-MHP | 150 psig | 57 % | 8 % |
| | 450 psig | 78 % | 5 % |
| B1-MHP | 150 psig | 78 % | ~ 0 % |
| | 450 psig | 95 % | 9 % |
| B2-MHP | 150 psig | 13 % | 3 % |
| | 450 psig | 16 % | 4 % |

As seen in Figure 4-5, all the MHPs at each carbonylation pressure exhibit an increase in mass due to the initial adsorption of CO onto the solid sample. The time taken to achieve a peak in mass was always higher for the samples carbonylated at 450 psig, and the mass peak was generally higher than the peak achieved at a pressure of 150 psig. The exception to this trend was B1-MHP, which achieved a peak relative mass of 110% within only 5 minutes of introducing CO into the PTGA, whereas it took 30 minutes to achieve a peak mass of 104% at 450 psig. For each sample (except B2-MHP), the peak was followed by a high rate of mass extraction until a time of approximately 100 minutes.

For L1-MHP, the increase of pressure from 150 psig to 450 psig did not affect kinetics and overall Ni extraction. During the high mass extraction phase in the first 100 minutes of the reaction, both samples of L1-MHP exhibited similar mass-loss trends at the two pressures. The mass at 150 psig started to plateau at 60 minutes, as compared to 85 minutes at 450 psig. Eventually, the relative mass approached 63% and 65% at 150 psig and 450 psig, respectively. ICP analysis showed that the extraction of Ni increased ever so slightly when L1-MHP was carbonylated at the higher pressure (77% Ni extraction increased to 78%). A

significant finding was that 3.5% of Co was extracted at 450 psig, suggesting that the implementation of an even higher carbonylation pressure would require downstream separation of nickel and cobalt carbonyls.

L2-MHP benefited from a higher carbonylation pressure more than L1-MHP, as ICP results show the Ni extraction increasing from 57% to 78% from lower to higher pressure. Figure 4-5b shows that mass extraction from L2-MHP occurs at a high rate until 60 minutes at 150 psig and 100 minutes at 450 psig. In contrast to L1-MHP, the mass does not plateau after this, but rather, mass loss continues at a decreased rate. The extraction results at 450 psig exhibited a greater rate of mass loss after 100 minutes compared to 150 psig. The slower phase of mass extraction can potentially be related to the carbonylation of Ni-Co alloys in the sample. Wang et al. [66] studied the extraction of Ni from Ni alloy powder (ranging from 50 – 60 % Ni by weight) through carbonylation and reported that elevated pressure is required to accelerate the activation of the Ni surface from the alloy. Using an initial alloy sample weight of 30 g and a carbonylation pressure of 145 psig, they achieved a 66% Ni extraction efficiency after 24 hours of reaction time with CO. At 290 psig, 63% efficiency was achieved after 17.5 hours. With the intermittent addition of H₂S, which is known to catalyze the carbonylation reaction, they achieved a 99% extraction after only 7.5 hours. This highlights that the surface characteristics of the alloy are altered, which promotes the carbonylation of Ni. The exact composition of the alloy used by Wang et al. [66] is unknown, along with the nature of the formed alloys during carbonylation tests in this project. However, it is evident that the carbonylation of Ni from alloys proceeds at a slower rate compared to pure metallic Ni.

The highest improvement in extraction efficiency was observed for B1-MHP, from which 95% of Ni was extracted at 450 psig, as compared to 78% at 150 psig. The carbonylation mass curves for this sample Figure 4-5c exhibit a similar trend to L2-MHP, where mass loss at 450 psig continues to occur at a slow rate past 100 minutes but plateaus at 150 psig. Theoretically, a Ni extraction efficiency higher than 95% could be possible at 450 psig if reaction times were extended. Additionally, 9% of Co was extracted at higher pressure, further validating that CO pressure has a positive effect on cobalt carbonyl formation.

B2-MHP is a sample characterized by its high initial Co content, at 11.7 wt.%. This feature of B2-MHP, along with it having the lowest surface area post-reduction at 450°C (20.5 m²/g), could potentially be the cause for the anomaly in low Ni extraction (only 13% and 16% of Ni was extracted at 150 psig and 450 psig). Figure 4-5d shows that a mass peak of 105% was achieved at 100 minutes for the 450 psig experiment, indicating that a larger content of CO was required to initialize the carbonylation reaction. The experiment at 150 psig saw a mass peak of 101% after 20 minutes. The PTGA data also reports a very low

mass extraction at both pressures, with the trend at 450 psig exhibiting a linear decline in mass at a slow rate. These results suggest that the Ni within the sample was not readily accessible to CO, likely due to the presence of cobalt, which may have inhibited the reaction through the formation of a Ni-Co alloy.

During this analysis, it was found that the Ni extraction obtained from ICP did not correspond exactly to the mass loss data from the PTGA. There are three main reasons for the difference in ICP extraction results and PTGA mass-loss data.

1. Sample heterogeneity: Each pellet of approximately 1 g that was loaded in the PTGA for reduction and carbonylation experiments may not represent the bulk Ni concentration measured by ICP analysis on a 0.05 g digest.
2. Analytical uncertainty in ICP analysis: There was a $\pm 5\%$ relative error in concentration from the digestion process analytical instrument.
3. PTGA mass referencing: The carbonylation tests began with the apparent final mass of the prior reduction step. The PTGA could be opened to measure the mass of the reduction residue, as this would have caused partial re-oxidation of the sample and would affect the subsequent carbonylation reaction. Hence, the final mass from the reduction experiments reported by the PTGA was used as the initial carbonylation mass. This method did not account for any buoyancy differences in reduction and carbonylation reaction gases.

Elevating the carbonylation pressure from 150 psig to 450 psig significantly improved Ni extraction in L2-MHP and B1-MHP. In comparison, the effect of CO pressure was insignificant for L1-MHP and B2-MHP. When purely drawing trends between the BET surface area /pore diameter after reduction and Ni extraction, L2-MHP had average pore diameters twice the size of L1-MHP post 450°C, and the surface area of B1-MHP was more than twice B2-MHP. A high Ni extraction efficiency is the result of a high surface area before carbonylation, appropriate pore sizes to facilitate CO and Ni(CO)₄ transport through porous networks, a high initial Ni content, and low content of Co, Mn or other metals that could form alloys with Ni.

Each MHP sample had its inherent structural characteristics and composition, which had effects of varying magnitudes on Ni extraction. The effect of surface area after the reduction of each sample at 450°C on the respective Ni extraction from carbonylation is shown in Figure 4-6. This again highlights that a high sample surface area promotes the carbonylation of Ni.

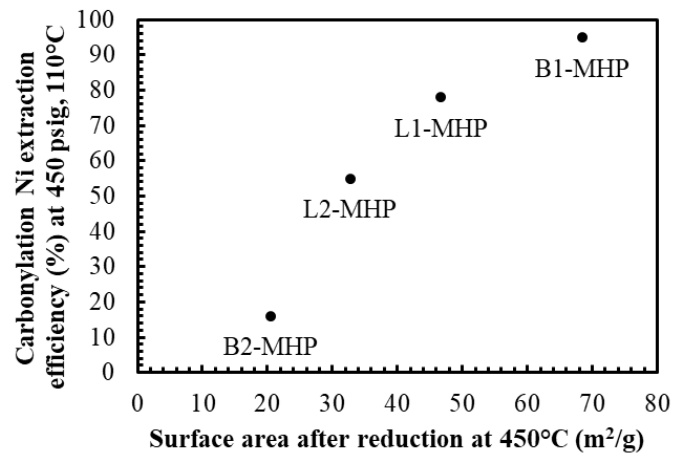


Figure 4-6: Ni extraction efficiency (%) at carbonylation conditions of 450 psig, 110°C for the four MHP samples against the BET surface area of the respective sample after a 450°C reduction

Chapter 5

Conclusions and Recommendations

5.1 Conclusions

This study systematically evaluated the extraction of Ni from MHPs derived from two primary sources: laterite ore and black mass. The aim was to maximize nickel recovery through a two-step dry process, involving the hydrogen reduction of the metallic oxides and the selective extraction of nickel into the vapour phase via carbonylation using carbon monoxide. The integrated approach, employing PTGA, FTIR, ICP-OES, and BET characterization techniques, provided insight into reaction mechanisms, kinetics, and structural transformations of the MHP samples throughout the two-step nickel extraction process.

Thermogravimetric analysis of the four MHPs allowed for the characterization of the reduction kinetics at varied temperatures (400°C, 450°C, and 500°C). Reduction experiments demonstrated significant differences in reaction behaviour between the samples. The mass-loss profiles indicated a positive effect of elevated temperature on the overall mass loss for L1-MHP and B1-MHP. For these two samples, the increase in reduction temperature correlated with pore enlargement, which facilitated effective H₂ gas and product H₂O transport to and from the metallic Ni sites within the porous pellet. Furthermore, it was found that the Avrami-Erofeev reduction kinetic model was most suitable for L1-MHP and B1-MHP, indicating the dominance of a nucleation-growth mechanism for the hydrogen reduction of nickel hydroxides in the PTGA setup. General reduction trends indicated that lower temperatures led to incomplete NiO reduction, whereas higher temperatures caused structural densification (sintering) and a decrease in surface area.

Carbonylation experiments highlighted the impact of reduction temperature, carbonylation temperature, and carbonation pressure on nickel extraction efficiency and kinetics. For B1-MHP, the mass extraction from carbonylation improved significantly at the higher temperatures of 450°C and 500°C. Conditions at these reduction temperatures yielded a favourable balance between surface area and pore size to facilitate effective diffusion of CO and Ni(CO)₄. An increase in carbonylation temperature from 110°C to 120°C removed the phase of mass increase (from the CO adsorption) and accelerated the extraction process to achieve a normalized mass of 55% within 50 minutes, as compared to 100 minutes at lower carbonylation temperatures. Although the initial extraction phase was accelerated, the normalized mass at all three temperatures approached 40% at the end of the reaction period. The evaluation of carbonylation pressures (150 psig versus 450 psig) showed that a higher pressure enhanced Ni extraction for L2-MHP (from 57%

to 78%) and B1-MHP (from 78% to 95%). When the Ni extraction efficiencies of the four MHPs were plotted against their respective BET surface area (after reduction at 450°C), it was evident that there is a direct correlation; carbonylation precursor materials with a high surface area (for example, B1-MHP with a BET surface area of 68.5 m²/g) were more effective at facilitating the formation of Ni(CO)₄. Samples characterized by a high surface area after reduction, well-developed pore structures, and an optimal Co concentration exhibited the maximum Ni extraction, respectively. The highest Ni extraction of 95% was achieved from B1-MHP (reduced at 450°C, carbonylated at 450 psig and 110°C).

In conclusion, this research successfully demonstrated a selective extraction pathway for Ni from MHPs through a completely dry processing route. The findings emphasize the importance of controlling reduction and carbonylation conditions to maximize extraction. The parameters of reactions affected each sample differently, according to its unique morphology and composition, but the results indicate that this research can be extended to allow sustainable and economically viable extraction of Ni from other primary and secondary sources as well.

5.2 Recommendations

Optimization of reaction conditions and kinetics:

Detailed experiments can be conducted with smaller increments in reduction/carbonylation temperature and carbonylation pressure to evaluate the effects on residue surface area, pore structure, and Ni extraction efficiency. The optimal conditions will vary depending on the precursor composition and microstructure; therefore, a series of experiments to determine the optimal reaction conditions for each distinct sample would be beneficial.

Advanced structural and morphological characterization:

1. SEM can be performed on fresh samples, reduction residues, and carbonylation residues across various reaction conditions to help visualize the morphological changes occurring. This may also give insight into reaction mechanisms and help understand how the Ni is distributed within the non-homogeneous particles.
2. Energy-dispersive X-ray (EDX) spectroscopy can be performed on fresh samples and reaction residues to generate elemental maps of the sample particles, giving further insight into how the elements of interest are distributed within the particles and how the distribution changes. X-ray

diffraction (XRD) can be used to understand the changes in the crystalline structures of Ni, Fe, Co, and other similar elements, as well as their respective transformations.

Flow system enhancement:

1. Carbonylation experiments can be performed at higher pressures using an autoclave reactor with mixing, allowing for greater solid-gas contact, effectively reducing any diffusional limitations.
2. The existing flow setup can be modified to allow for a feed of H₂S gas into the PTGA. Literature indicates that the intermittent pulsing of H₂S reactivates the carbonylation reaction and can be used to shorten reaction times and maximize Ni extraction [66].
3. Future work should explore the dilution of the off-gas stream with inert gas (such as N₂) to reduce the effective concentration of Ni(CO)₄ entering the FTIR cell. This would help keep the carbonyl peak within the detection range of the instrument and prevent signal saturation. With this improvement, a quantitative analysis of the carbonyl peaks can be performed to obtain an approximate concentration profile against time, complementing the mass loss data from the PTGA.
4. Using the observed relationships between reduction conditions, pressure effects, and feed composition, preliminary reactor sizing can be carried forward to a small pilot-scale design. A prototype carbonylation reactor can be designed to be suitable for multiple types of feed sources. Computational fluid dynamics and process simulation software can be utilized to model the solid-gas interactions, pressure/temperature profiles, and reaction kinetics.
5. A small-scale downstream carbonyl decomposition can be designed and implemented within the existing flow system to close the loop of the carbonyl process. Initial trials can use a simple copper tube, outfitted with a heater to raise the internal temperature to around 175°C and to recover metallic Ni in powder form from the producing Ni(CO)₄. Later iterations should consider exploring chemical vapour deposition design on a larger scale to produce high-purity Ni for various end-use applications

Letters of Copyright Permission

Figure 2-1:

7/21/25, 9:33 AM Terms and Conditions - Natural Resources Canada

Terms and Conditions

Ownership and Usage of Content Provided on This Site

Materials on this website were produced and/or compiled by Natural Resources Canada for the purpose of providing Canadians with access to information about the programs and services offered by the Government of Canada. You may use and reproduce the materials as follows:

<https://natural-resources.canada.ca/corporate/terms-conditions> 11/15

<https://natural-resources.canada.ca/corporate/terms-conditions> 11/15

7/21/25, 9:33 AM Terms and Conditions - Natural Resources Canada

Non-Commercial Reproduction

Permission to reproduce Government of Canada works, in part or in whole, and by any means, for personal or public non-commercial purposes, or for cost-recovery purposes, is not required, unless otherwise specified in the material you wish to reproduce.

A **reproduction** means making a copy of information in the manner that it is originally published – the reproduction must remain as is, and must not contain any alterations whatsoever.

The terms **personal** and **public non-commercial purposes** mean a distribution of the reproduced information either for your own purposes only, or for a distribution at large whereby no fees whatsoever will be charged.

The term **cost-recovery** means charging a fee for the purpose of recovering printing costs and other costs associated with the production of the reproduction.

Users are required to:

- Exercise due diligence in ensuring the accuracy of the materials reproduced;
- Indicate both the complete title of the materials reproduced, as well as the author organization; and
- Indicate that the reproduction is a copy of an official work that is published by the Government of Canada and that the reproduction has not been produced in affiliation with, or with the endorsement of the Government of Canada.

Unless otherwise specified, this authorization is also applicable to all published information regardless of its format.

<https://natural-resources.canada.ca/corporate/terms-conditions> 12/15

Figure 2-2:

7/21/25, 9:58 AM

RightsLink Printable License

ELSEVIER LICENSE
TERMS AND CONDITIONS

Jul 21, 2025

This Agreement between Param Dave, University of Waterloo ("You") and Elsevier ("Elsevier") consists of your license details and the terms and conditions provided by Elsevier and Copyright Clearance Center.

| | |
|------------------------------|--|
| License Number | 6073660985653 |
| License date | Jul 21, 2025 |
| Licensed Content Publisher | Elsevier |
| Licensed Content Publication | Ore Geology Reviews |
| Licensed Content Title | Nickel sulfide deposits in Australia: Characteristics, resources, and potential |
| Licensed Content Author | Dean M. Hoatson, Subhash Jaireth, A. Lynton Jaques |
| Licensed Content Date | Nov 1, 2006 |
| Licensed Content Volume | 29 |
| Licensed Content Issue | 3-4 |
| Licensed Content Pages | 65 |
| Start Page | 177 |
| End Page | 241 |

<https://s100.copyright.com/AppDispatchServlet>

1/8

7/21/25, 9:58 AM

RightsLink Printable License

| | |
|---|--|
| Type of Use | reuse in a thesis/dissertation |
| Portion | figures/tables/illustrations |
| Number of figures/tables/illustrations | 1 |
| Format | electronic |
| Are you the author of this Elsevier article? | No |
| Will you be translating? | No |
| Title of new work | Dry Extraction of Nickel from Mixed-Hydroxide Precipates via Reduction and Carbonylation |
| Institution name | University of Waterloo |
| Expected presentation date | Aug 2025 |
| Portions | Figure 3 |
| The Requesting Person / Organization to Appear on the License | Param Dave, University of Waterloo |
| Requestor Location | 942 Donnelly Street Milton, ON L9T 6E2 Canada |
| Order reference number | Figure 2-2 |
| Publisher Tax ID | GB 494 6272 12 |
| Total | 0.00 CAD |

Figure 2-3:

7/21/25, 9:48 PM

RightsLink Printable License

ELSEVIER LICENSE TERMS AND CONDITIONS

Jul 21, 2025

This Agreement between Param Dave, University of Waterloo ("You") and Elsevier ("Elsevier") consists of your license details and the terms and conditions provided by Elsevier and Copyright Clearance Center.

| | |
|------------------------------|--|
| License Number | 6073941145903 |
| License date | Jul 21, 2025 |
| Licensed Content Publisher | Elsevier |
| Licensed Content Publication | Minerals Engineering |
| Licensed Content Title | Assessing the energy and greenhouse gas footprints of nickel laterite processing |
| Licensed Content Author | T. Norgate,S. Jahanshahi |
| Licensed Content Date | Jun 1, 2011 |
| Licensed Content Volume | 24 |
| Licensed Content Issue | 7 |
| Licensed Content Pages | 10 |
| Start Page | 698 |
| End Page | 707 |

<https://s100.copyright.com/AppDispatchServlet>

1/8

| | |
|---|--|
| Type of Use | reuse in a thesis/dissertation |
| Portion | figures/tables/illustrations |
| Number of figures/tables/illustrations | 1 |
| Format | electronic |
| Are you the author of this Elsevier article? | No |
| Will you be translating? | No |
| Title of new work | Dry Extraction of Nickel from Mixed-Hydroxide Precipitates via Reduction and Carbonylation |
| Institution name | University of Waterloo |
| Expected presentation date | Aug 2025 |
| Portions | General laterite ore processing paths figure |
| The Requesting Person / Organization to Appear on the License | Param Dave, University of Waterloo |
| Requestor Location | Mr. Param Dave 942 Donnelly Street Milton, ON L9T 6E2 Canada |
| Order reference number | Figure 2-3 |
| Publisher Tax ID | GB 494 6272 12 |
| Total | 0.00 CAD |

Figure 2-4:

7/21/25, 10:23 PM

RightsLink Printable License

ELSEVIER LICENSE
TERMS AND CONDITIONS

Jul 21, 2025

This Agreement between Param Dave, University of Waterloo ("You") and Elsevier ("Elsevier") consists of your license details and the terms and conditions provided by Elsevier and Copyright Clearance Center.

| | |
|------------------------------|---|
| License Number | 6073960293990 |
| License date | Jul 21, 2025 |
| Licensed Content Publisher | Elsevier |
| Licensed Content Publication | Elsevier Books |
| Licensed Content Title | Extractive Metallurgy of Nickel, Cobalt and Platinum Group Metals |
| Licensed Content Author | Frank K. Crundwell, Michael S. Moats, Venkoba Ramachandran, Timothy G. Robinson, William G. Davenport |
| Licensed Content Date | Jan 1, 2011 |
| Licensed Content Pages | 6 |
| Start Page | 117 |
| End Page | 122 |
| Type of Use | reuse in a thesis/dissertation |
| Portion | figures/tables/illustrations |

<https://s100.copyright.com/AppDispatchServlet>




1/8

| | |
|---|--|
| Number of figures/tables/illustrations | 1 |
| Format | electronic |
| Are you the author of this Elsevier chapter? | No |
| Will you be translating? | No |
| Title of new work | Dry Extraction of Nickel from Mixed-Hydroxide Precipitates via Reduction and Carbonylation |
| Institution name | University of Waterloo |
| Expected presentation date | Aug 2025 |
| Portions | General HPAL process for a laterite ore feed leached in sulfuric acid |
| The Requesting Person / Organization to Appear on the License | Param Dave, University of Waterloo |
| Requestor Location | Mr. Param Dave 942 Donnelly Street Milton, ON L9T 6E2 Canada |
| Order reference number | Figure 2-4 |
| Publisher Tax ID | GB 494 6272 12 |
| Total | 0.00 CAD |


Figure 2-9:

7/22/25, 12:28 AM

Rightslink® by Copyright Clearance Center

Sign in/Register  

Experimental and Theoretical Studies on the Reaction of H₂ with NiO: Role of O Vacancies and Mechanism for Oxide Reduction



Author: José A. Rodriguez, Jonathan C. Hanson, Anatoly I. Frenkel, et al
Publication: Journal of the American Chemical Society
Publisher: American Chemical Society
Date: Jan 1, 2002
Copyright © 2002, American Chemical Society

Quick Price Estimate

This service provides permission for reuse only. If you do not have a copy of the portion you are using, you may copy and paste the content and reuse according to the terms of your agreement. Please be advised that obtaining the content you license is a separate transaction not involving RightsLink.

If credit is given to another source for the material you requested from RightsLink, permission must be obtained from that source.

Note: Individual Scheme and Structure reuse is free of charge and does not require a license. If the scheme or structure is identified as a Figure in the article, permission is required.

This type of permission/license, instead of the standard Terms and Conditions, is sent to you because no fee is being charged for your order. Please note the following:

- Permission is granted for your request in both print and electronic formats, and translations.
- If figures and/or tables were requested, they may be adapted or used in part.
- Please print this page for your records and send a copy of it to your publisher/graduate school.
- Appropriate credit for the requested material should be given as follows: "Reprinted (adapted) with permission from {COMPLETE REFERENCE CITATION}. Copyright {YEAR} American Chemical Society." Insert appropriate information in place of the capitalized words.
- One-time permission is granted only for the use specified in your RightsLink request. No additional uses are granted (such as derivative works or other editions). For any uses, please submit a new request.

If credit is given to another source for the material you requested from RightsLink, permission must be obtained from that source.

This reuse is free of charge and does not require a license. Please print this page for your records.

I would like to...

Requestor Type

Portion

Number of Table/Figure/Microgra

Format

Select your currency

Price: 0.00 CAD

[CONTINUE](#)

Figure 2-10:

7/22/25, 12:39 AM

RightsLink Printable License

ELSEVIER LICENSE
TERMS AND CONDITIONS

Jul 22, 2025

This Agreement between Param Dave, University of Waterloo ("You") and Elsevier ("Elsevier") consists of your license details and the terms and conditions provided by Elsevier and Copyright Clearance Center.

| | |
|------------------------------|---|
| License Number | 6074010917203 |
| License date | Jul 22, 2025 |
| Licensed Content Publisher | Elsevier |
| Licensed Content Publication | Journal of Alloys and Compounds |
| Licensed Content Title | Isothermal decomposition kinetics of nickel (II) hydroxide powder |
| Licensed Content Author | C.S. Carney,R.E. Chinn,Ö.N. Doğan,M.C. Gao |
| Licensed Content Date | Sep 25, 2015 |
| Licensed Content Volume | 644 |
| Licensed Content Issue | n/a |
| Licensed Content Pages | 7 |
| Start Page | 968 |
| End Page | 974 |

<https://s100.copyright.com/AppDispatchServlet>

1/8

| | |
|---|--|
| Type of Use | reuse in a thesis/dissertation |
| Portion | figures/tables/illustrations |
| Number of figures/tables/illustrations | 1 |
| Format | electronic |
| Are you the author of this Elsevier article? | No |
| Will you be translating? | No |
| Title of new work | Dry Extraction of Nickel from Mixed-Hydroxide Precipates via Reduction and Carbonylation |
| Institution name | University of Waterloo |
| Expected presentation date | Aug 2025 |
| Portions | Figure 5 |
| The Requesting Person / Organization to Appear on the License | Param Dave, University of Waterloo |
| Requestor Location | Mr. Param Dave 942 Donnelly Street Milton, ON L9T 6E2 Canada |
| Order reference number | Figure 2-10 |
| Publisher Tax ID | GB 494 6272 12 |
| Total | 0.00 CAD |

Figure 2-12:

7/22/25, 1:00 AM

Rightslink® by Copyright Clearance Center

PD ?

Kinetics of Nickel Carbonyl Formation

Author: W. M. Goldberger, D. F. Othmer
Publication: Industrial & Engineering Chemistry Research
Publisher: American Chemical Society
Date: Jul 1, 1963
Copyright © 1963, American Chemical Society

Quick Price Estimate

This service provides permission for reuse only. If you do not have a copy of the portion you are using, you may copy and paste the content and reuse according to the terms of your agreement. Please be advised that obtaining the content you license is a separate transaction not involving RightsLink.

If credit is given to another source for the material you requested from RightsLink, permission must be obtained from that source.

Note: Individual Scheme and Structure reuse is free of charge and does not require a license. If the scheme or structure is identified as a Figure in the article, permission is required.

This type of permission/license, instead of the standard Terms and Conditions, is sent to you because no fee is being charged for your order. Please note the following:

- Permission is granted for your request in both print and electronic formats, and translations.
- If figures and/or tables were requested, they may be adapted or used in part.
- Please print this page for your records and send a copy of it to your publisher/graduate school.
- Appropriate credit for the requested material should be given as follows: "Reprinted (adapted) with permission from {COMPLETE REFERENCE CITATION}. Copyright {YEAR} American Chemical Society." Insert appropriate information in place of the capitalized words.
- One-time permission is granted only for the use specified in your RightsLink request. No additional uses are granted (such as derivative works or other editions). For any uses, please submit a new request.

If credit is given to another source for the material you requested from RightsLink, permission must be obtained from that source.

This reuse is free of charge and does not require a license. Please print this page for your records.

I would like to...

Requestor Type

Portion

Number of Table/Figure/Microgra

Format

Select your currency

Price: 0.00 USD

[CONTINUE](#)

Figure 2-13:

7/22/25, 1:15 AM

RightsLink Printable License

ELSEVIER LICENSE
TERMS AND CONDITIONS

Jul 22, 2025

This Agreement between Param Dave, University of Waterloo ("You") and Elsevier ("Elsevier") consists of your license details and the terms and conditions provided by Elsevier and Copyright Clearance Center.

| | |
|------------------------------|---|
| License Number | 6074030038495 |
| License date | Jul 22, 2025 |
| Licensed Content Publisher | Elsevier |
| Licensed Content Publication | International Journal of Hydrogen Energy |
| Licensed Content Title | Theoretical investigation of the reactivity of flat Ni (111) and stepped Ni (211) surfaces for acetic acid hydrogenation to ethanol |
| Licensed Content Author | Hui Shi,Ming Xia,Huaiqian Lu,Qilong Xie,Litao Jia,Bo Hou,Yong Xiao,Debao Li |
| Licensed Content Date | Apr 26, 2021 |
| Licensed Content Volume | 46 |
| Licensed Content Issue | 29 |
| Licensed Content Pages | 17 |
| Start Page | 15454 |
| End Page | 15470 |

<https://s100.copyright.com/AppDispatchServlet>

1/8

| | |
|---|--|
| Type of Use | reuse in a thesis/dissertation |
| Portion | figures/tables/illustrations |
| Number of figures/tables/illustrations | 1 |
| Format | electronic |
| Are you the author of this Elsevier article? | No |
| Will you be translating? | No |
| Title of new work | Dry Extraction of Nickel from Mixed-Hydroxide Precipates via Reduction and Carbonylation |
| Institution name | University of Waterloo |
| Expected presentation date | Aug 2025 |
| Portions | Crystalline arrangement of Ni(211) surface |
| The Requesting Person / Organization to Appear on the License | Param Dave, University of Waterloo |
| Requestor Location | Mr. Param Dave 942 Donnelly Street Milton, ON L9T 6E2 Canada |
| Order reference number | Figure 2-13 |
| Publisher Tax ID | GB 494 6272 12 |
| Total | 0.00 CAD |

References

- [1] “Global nickel demand in the Net Zero Scenario, 2023-2040 – Charts – Data & Statistics,” IEA. Accessed: Jul. 20, 2025. [Online]. Available: <https://www.iea.org/data-and-statistics/charts/global-nickel-demand-in-the-net-zero-scenario-2023-2040>
- [2] Kerfoot, Derek G. E., “Nickel,” in *Ullmann’s Encyclopedia of Industrial Chemistry*, Weinheim: Wiley-VCH Verlag GmbH & Co. KGaA, 2005.
- [3] N. R. Canada, “Nickel facts.” Accessed: Jan. 09, 2025. [Online]. Available: <https://natural-resources.canada.ca/minerals-mining/mining-data-statistics-and-analysis/minerals-metals-facts/nickel-facts/20519>
- [4] D. M. Hoatson, S. Jaireth, and A. L. Jaques, “Nickel sulfide deposits in Australia: Characteristics, resources, and potential,” *ResearchGate*, 2006, doi: 10.1016/j.oregeorev.2006.05.002.
- [5] Y. Cui, “Carbonylation of Nickel and Iron from Reduced Oxides and Laterite Ore,” Thesis, UNSW Sydney, 2015. doi: 10.26190/unsworks/2881.
- [6] C. H. Köse, “Hydrometallurgical processing of lateritic nickel ores,” Master Thesis, Middle East Technical University, 2010. Accessed: Jan. 11, 2025. [Online]. Available: <https://open.metu.edu.tr/handle/11511/19895>
- [7] R. Moskalyk and A. Alfantazi, “Nickel laterite processing and electrowinning practice | Request PDF,” *ResearchGate*, vol. 15, no. 8, pp. 593–605, 2002, doi: 10.1016/S0892-6875(02)00083-3.
- [8] Y. Li, H. Yu, D. Wang, W. Yin, and Y. Bai, “The Current Status of Laterite Nickel Ore Resources and its Processing Technology,” *Met. Mine*, no. 413, pp. 5–9.
- [9] T. Norgate and S. Jahanshahi, “Assessing the energy and greenhouse gas footprints of nickel laterite processing | Request PDF,” *ResearchGate*, vol. 24, no. 7, pp. 698–707, 2011, doi: 10.1016/j.mineng.2010.10.002.
- [10] A. D. Dalvi, W. G. Bacon, and R. C. Osborne, “The Past and the Future of Nickel Laterites,” presented at the PDAC 2004 International Convention, Trade Show and Investors Exchange, 2004.
- [11] F. Crundwell, M. S. Moats, V. Ramachandran, T. Robinson, and W. G. Davenport, “Smelting of nickel sulfide concentrates by roasting and electric furnace smelting,” in *Extractive Metallurgy of Nickel, Cobalt, and Platinum-Group Metals*, Amsterdam, Netherlands: Elsevier, 2011, pp. 199–214.

- [12]F. Crundwell, M. S. Moats, V. Ramachandran, T. Robinson, and W. G. Davenport, “Converting – Final Oxidation of Iron from Molten Matte,” in *Extractive Metallurgy of Nickel, Cobalt, and Platinum-Group Metals*, Amsterdam, Netherlands: Elsevier, 2011, pp. 233–246.
- [13]F. Crundwell, M. S. Moats, V. Ramachandran, T. G. Robinson, and W. G. Davenport, “Overview of the Hydrometallurgical Processing of Laterite Ores,” in *Extractive Metallurgy of Nickel, Cobalt and Platinum-Group Metals*, Amsterdam, Netherlands: Elsevier, 2011, pp. 117–121.
- [14]T. Gultom and A. Sianipar, “High Pressure Acid Leaching: A Newly Introduced Technology in Indonesia,” presented at the IOP Conference Series: Earth and Environmental Science, 2010.
- [15]A. Vahed, P. Mackey, and A. Warner, “‘Around the Nickel World in Eighty Days’: A Virtual Tour of World Nickel Sulphide and Laterite Operations and Technologies,” presented at the Ni-Co 2021: The 5th International Symposium on Nickel and Cobalt, 2021, pp. 3–39.
- [16]K. K. Mamyrbayeva, A. N. Kuandykova, T. A. Chepushtanova, and Y. S. Merkitabeyev, “Review of technology for hydrometallurgical processing of lateritic nickel ores over the past 20 years in the world,” *Non-Ferr. Met.*, no. 1, pp. 13–21, Jun. 2024, doi: 10.17580/nfm.2024.01.03.
- [17]K. Zhao, F. Gao, and Q. Yang, “Comprehensive Review on Metallurgical Upgradation Processes of Nickel Sulfide Ores,” *J. Sustain. Metall.*, vol. 8, no. 1, pp. 37–50, 2022, doi: 10.1007/s40831-022-00501-3.
- [18]N. Faris, M. I. Pownceby, W. J. Bruckard, and M. Chen, “The Direct Leaching of Nickel Sulfide Flotation Concentrates – A Historic and State-of-the-Art Review Part I: Piloted Processes and Commercial Operations,” *Miner. Process. Extr. Metall. Rev.*, vol. 44, no. 6, pp. 407–435, Aug. 2023, doi: 10.1080/08827508.2022.2070617.
- [19]C. A. Chamberlain, O. J. C. Czerny, H. Liu, and T. H. Muller, “Atmospheric Acid Leach Process for Laterites,” WO 2009/018619 A1, 2009
- [20]“Mixed hydroxide precipitate — the new class one nickel,” MINING.COM. Accessed: Mar. 12, 2025. [Online]. Available: <https://www.mining.com/mixed-hydroxide-precipitate-the-new-class-one-nickel/>
- [21]N. Safitri, Z. Mubarik, R. Winarko, and Z. T. Ichlas, “Recovery of nickel and cobalt as MHP from limonitic ore leaching solution: Kinetics analysis and precipitate characterization,” in *ResearchGate*, 2018, pp. 020030–1 to 020030–11. doi: 10.1063/1.5038312.
- [22]B. Willis, “DOWNSTREAM PROCESSING OPTIONS FOR NICKEL LATERITE HEAP LEACH LIQUORS,” in *ResearchGate*, Perth, Australia, 2007, pp. 21–23. Accessed: Mar. 13, 2025. [Online].

Available:

https://www.researchgate.net/publication/272566493_DOWNSTREAM_PROCESSING_OPTIONS_FOR_NICKEL_LATERITE_HEAP_LEACH_LIQUORS

- [23] G. Peh, "Indonesia's nickel companies: The need for renewable energy amid increasing production," Institute for Energy Economics and Financial Analysis. Accessed: Mar. 18, 2025. [Online]. Available: <https://ieefa.org/resources/indonesias-nickel-companies-need-renewable-energy-amid-increasing-production>
- [24] C. Williams, W. Hawker, and J. W. Vaughan, "Selective leaching of nickel from mixed nickel cobalt hydroxide precipitate," *Hydrometallurgy*, vol. 138, pp. 84–92, Jun. 2013, doi: 10.1016/j.hydromet.2013.05.015.
- [25] V. D. Andriyanto, Z. T. Ichlas, and M. Z. Mubarak, "Removal of Impurities from Nickel and Cobalt in Mixed Hydroxide Precipitate with Solvent Extraction Using Di(2-Ethylhexyl) Phosphoric Acid," *Miner. Process. Extr. Metall. Rev.*, no. 0, Oct. 2024, doi: 10.1080/08827508.2024.2418625.
- [26] S. Hussaini, A. M. Tita, S. Kursunoglu, M. Kaya, and P. Chu, "Leaching of Nickel and Cobalt from a Mixed Nickel-Cobalt Hydroxide Precipitate Using Organic Acids," *Minerals*, vol. 14, no. 3, Art. no. 3, Mar. 2024, doi: 10.3390/min14030314.
- [27] "Operations: Special Products," Canadian Mining Journal. Accessed: Mar. 27, 2025. [Online]. Available: <https://www.canadianminingjournal.com/featured-article/operations-special-products/>
- [28] P. Morris, "The legacy of Ludwig Mond," *Endeavour*, vol. 13, no. 1, pp. 34–40, Jan. 1989, doi: 10.1016/0160-9327(89)90049-5.
- [29] D. S. Lee and D. J. Min, "A Kinetics of Hydrogen Reduction of Nickel Oxide at Moderate Temperature," *Met. Mater. Int.*, vol. 25, no. 4, pp. 982–990, Jul. 2019, doi: 10.1007/s12540-019-00261-y.
- [30] L. Mond, C. Langer, and F. Quincke, "L.—Action of carbon monoxide on nickel," *J. Chem. Soc. Trans.*, vol. 57, no. 0, pp. 749–753, Jan. 1890, doi: 10.1039/CT8905700749.
- [31] J. Das, S. Srikanth, and Premchand, "Thermodynamics and Kinetics of the Carbonyl process for the Refining of Nickel," presented at the Recent advances in metallurgical processes - Vol 1, IIS, Bangalore, Jul. 1997, pp. 171–175. Accessed: Mar. 27, 2025. [Online]. Available: <http://eprint.nmlindia.org/6561>
- [32] "Nickel," CAREX Canada. Accessed: Mar. 27, 2025. [Online]. Available: <https://www.carexcanada.ca/profile/nickel/>

- [33]“Permissible Exposure Limits - Annotated Tables | Occupational Safety and Health Administration.” Accessed: Mar. 27, 2025. [Online]. Available: <https://www.osha.gov/annotated-pels>
- [34]J. R. Boldt, Jr. and P. Queneau, *The Winning of Nickel*. Toronto: Longmans, 1967.
- [35]J. Shu and L. Koehler, “The changing landscape of carbonyl iron and nickel powder production,” Inovar Communications Ltd., Review, 2017. Accessed: Mar. 31, 2025. [Online]. Available: <https://www.metal-powder.tech/powder-metallurgy-review-archive/powder-metallurgy-review-spring-2017-vol-6-no-1/>
- [36]F. Crundwell, M. S. Moats, V. Ramachandran, T. G. Robinson, and W. G. Davenport, “Carbonyl Refining of Impure Nickel Metal,” in *Extractive Metallurgy of Nickel, Cobalt and Platinum-Group Metals*, Amsterdam, Netherlands: Elsevier, 2011, pp. 269–280.
- [37]S. S. Naboychenko, I. B. Murashova, and O. D. Neikov, “Production of Nickel and Nickel-alloy Powders,” in *Handbook of Non-Ferrous Metal Powders*, Amsterdam, Netherlands: Elsevier, 2009, pp. 373–374.
- [38]“Our Process,” Westwin Elements. Accessed: Apr. 01, 2025. [Online]. Available: <https://www.westwinelements.com/our-process>
- [39]S. Pöyhtäri, J. Ruokoja, E.-P. Heikkinen, A. Heikkilä, T. Kokkonen, and P. Tynjälä, “Kinetic Analysis of Hydrogen Reduction of Nickel Compounds,” *Metall. Mater. Trans. B*, vol. 55, no. 1, pp. 251–265, Feb. 2024, doi: 10.1007/s11663-023-02955-6.
- [40]C. S. Carney, R. E. Chinn, Ö. N. Doğan, and M. C. Gao, “Isothermal decomposition kinetics of nickel (II) hydroxide powder,” *J. Alloys Compd.*, vol. 644, pp. 968–974, Sep. 2015, doi: 10.1016/j.jallcom.2015.03.256.
- [41]K. S. A. Halim *et al.*, “Reduction Behavior and Characteristics of Metal Oxides in the Nanoscale,” *Metals*, vol. 12, no. 12, Art. no. 12, Dec. 2022, doi: 10.3390/met12122182.
- [42]J. T. Richardson, R. Scates, and M. V. Twigg, “X-ray diffraction study of nickel oxide reduction by hydrogen,” *Appl. Catal. Gen.*, vol. 246, no. 1, pp. 137–150, Jun. 2003, doi: 10.1016/S0926-860X(02)00669-5.
- [43]K. V. Manukyan *et al.*, “Nickel Oxide Reduction by Hydrogen: Kinetics and Structural Transformations,” *J. Phys. Chem. C*, vol. 119, no. 28, pp. 16131–16138, Jul. 2015, doi: 10.1021/acs.jpcc.5b04313.

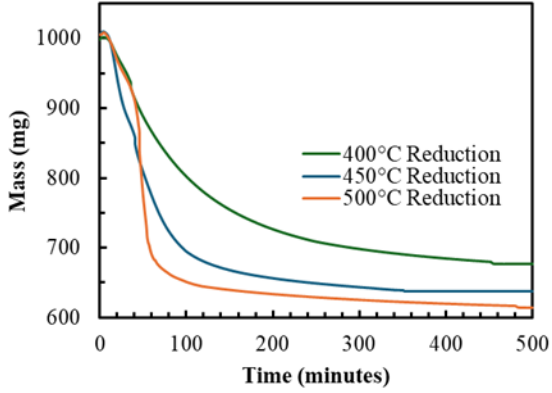
- [44]R. Chatterjee, S. Banerjee, S. Banerjee, and D. Ghosh, "Reduction of Nickel Oxide Powder and Pellet by Hydrogen," *Trans. Indian Inst. Met.*, vol. 65, no. 3, pp. 265–273, Jun. 2012, doi: 10.1007/s12666-012-0130-0.
- [45]J. A. Rodriguez, J. C. Hanson, A. I. Frenkel, J. Y. Kim, and M. Pérez, "Experimental and Theoretical Studies on the Reaction of H₂ with NiO: Role of O Vacancies and Mechanism for Oxide Reduction," *J. Am. Chem. Soc.*, vol. 124, no. 2, pp. 346–354, Jan. 2002, doi: 10.1021/ja0121080.
- [46]G. Foran, "Nickel Oxide Reduction and the Effect of Metal Sulfates," Master's Thesis, University of Guelph, 2014.
- [47]K. M. A. El-Salaam and E. A. Hassan, "A study of the effect of lithium and aluminium on the thermal decomposition of nickel hydroxide," *Surf. Technol.*, vol. 11, no. 1, pp. 55–60, Jul. 1980, doi: 10.1016/0376-4583(80)90018-7.
- [48]I. F. Hazell and R. J. Irving, "The thermal decomposition of iron(II), cobalt(II), and nickel(II) hydroxides," *J. Chem. Soc. Inorg. Phys. Theor.*, no. 0, pp. 669–673, Jan. 1966, doi: 10.1039/J19660000669.
- [49]R. Chatterjee, S. Banerjee, S. Banerjee, and D. Ghosh, "Reduction of Nickel Oxide Powder and Pellet by Hydrogen," *Trans. Indian Inst. Met.*, vol. 65, no. 3, pp. 265–273, Jun. 2012, doi: 10.1007/s12666-012-0130-0.
- [50]G. Plascencia and T. Utigard, "The reduction of Tokyo and Sinter 75 nickel oxides with hydrogen," *Chem. Eng. Sci.*, vol. 64, no. 17, pp. 3879–3888, Sep. 2009, doi: 10.1016/j.ces.2009.05.030.
- [51]W. M. Goldberger and D. F. Othmer, "Kinetics of Nickel Carbonyl Formation," *Ind. Eng. Chem. Process Des. Dev.*, vol. 2, no. 3, pp. 202–209, Jul. 1963, doi: 10.1021/i260007a006.
- [52]K. Lascelles and L. V. Renny, "The rate of formation of nickel carbonyl from carbon monoxide and nickel single crystals," *Surf. Sci.*, vol. 125, no. 2, pp. L67–L72, Feb. 1983, doi: 10.1016/0039-6028(83)90567-8.
- [53]G. Greiner and D. Menzel, "Promotion and inhibition of Ni(CO)₄ formation on Ni(100): A kinetic investigation coupled with ESCA measurements," *J. Catal.*, vol. 77, no. 2, pp. 382–396, Oct. 1982, doi: 10.1016/0021-9517(82)90180-4.
- [54]D. B. Liang, G. Abend, J. H. Block, and N. Kruse, "Formation of nickel subcarbonyls from nickel and carbon monoxide," *Surf. Sci.*, vol. 126, no. 1, pp. 392–396, Mar. 1983, doi: 10.1016/0039-6028(83)90733-1.
- [55]L. T. Redmon, "Kinetics of Ni(CO)₄ Formation," U.S. Air Force Office of Scientific Research, 1980.

- [56]H. Shi *et al.*, “Theoretical investigation of the reactivity of flat Ni (111) and stepped Ni (211) surfaces for acetic acid hydrogenation to ethanol,” *Int. J. Hydrog. Energy*, vol. 46, no. 29, pp. 15454–15470, Apr. 2021, doi: 10.1016/j.ijhydene.2021.02.045.
- [57]J. Engbæk, O. Lytken, J. H. Nielsen, and I. Chorkendorff, “CO dissociation on Ni: The effect of steps and of nickel carbonyl,” *Surf. Sci.*, vol. 602, no. 3, pp. 733–743, Feb. 2008, doi: 10.1016/j.susc.2007.12.008.
- [58]Z. P. Xu and H. C. Zeng, “Thermal evolution of cobalt hydroxides: a comparative study of their various structural phases,” *J. Mater. Chem.*, vol. 8, no. 11, pp. 2499–2506, Jan. 1998, doi: 10.1039/A804767G.
- [59]K. LILIUS, “ON THE EFFECT OF THE STRUCTURE OF THE METAL AND OXIDE PHASE ON THE KINETICS AND MECHANISM OF THE HYDROGEN REDUCTION OF COBALT OXIDE,” *Eff. Struct. Met. OXIDE PHASE Kinet. Mech. Hydrog. Reduct. COBALT OXIDE*, 1974.
- [60]E. A. Brocchi, F. J. Moura, and D. W. de Macedo, “Synthesis and characterisation of nanostructured Ni–Co alloy Part 2: Co₃O₄ reduction kinetics,” *Miner. Process. Extr. Metall.*, vol. 118, no. 1, pp. 40–43, Mar. 2009, doi: 10.1179/174328508X375377.
- [61]“(PDF) Carbothermal Solid State Reduction of Manganese Ores: 3. Phase Development,” *ResearchGate*, doi: 10.2355/isijinternational.49.1115.
- [62]E. O. Brimm, M. A. Jr. Lynch, and W. J. Sesny, “Preparation and Properties of Manganese Carbonyl,” *J. Am. Chem. Soc.*, vol. 76, no. 14, pp. 3831–3835, Jul. 1954, doi: 10.1021/ja01643a071.
- [63]N. Dzakaria *et al.*, “Effect of Cobalt on Nickel Oxide Toward Reduction Behaviour in Hydrogen and Carbon Monoxide Atmosphere,” *Mater. Sci. Forum*, vol. 1010, pp. 373–378, 2020, doi: 10.4028/www.scientific.net/MSF.1010.373.
- [64]B. A. Abd-El-Nabey, S. El-Housseiny, A. M. Abdel-Gaber, and M. E. Mohamed, “Kinetics of oxidation of metals in the air at room temperature using EDX,” *Results Chem.*, vol. 5, p. 100876, Jan. 2023, doi: 10.1016/j.rechem.2023.100876.
- [65]“Ni(CO)₄ and Fe(CO)₅: Molecular structures in the solid state | Request PDF,” *ResearchGate*, doi: 10.1002/chin.199331041.
- [66]D. Wang, A. Chen, Z. Zhao, and G. Huo, “Extraction of nickel from nickel alloy by carbonylation,” *Transit. Met. Chem.*, vol. 34, no. 3, pp. 313–316, Apr. 2009, doi: 10.1007/s11243-009-9196-x.

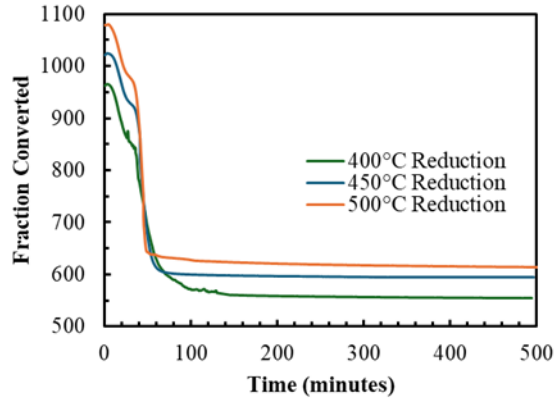
Appendix A

Raw Data and Sample Calculations

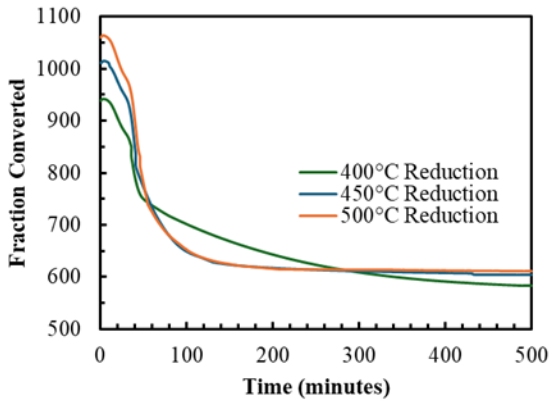
a) L1-MHP



b) L2-MHP



c) B1-MHP



d) B2-MHP

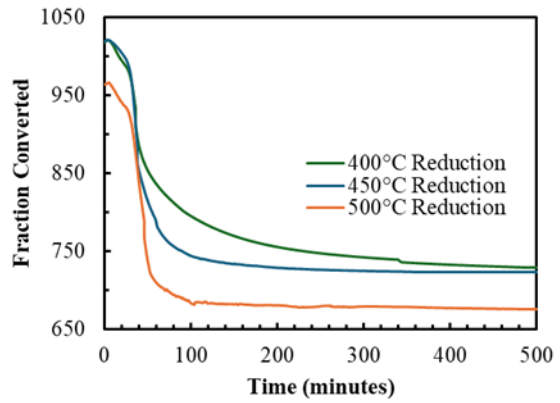


Figure A - 1: Mass profile during reduction under H₂ atmosphere at 6 psig and temperatures of 400°C, 450°C, and 500°C of a) L1-MHP, b) L2-MHP, c) B1-MHP, and d) B2-MHP.

A sample calculation of the error propagation of the Ni extraction efficiency, as presented earlier in Equation 3-5, is shown below in Equation A-1

$$\frac{\partial E_i}{E_i} (\%) = \left[\left(\frac{\partial m_o}{m_o} \right)^2 + \left(\frac{\partial x_{o,i}}{x_{o,i}} \right)^2 + \left(\frac{\partial m_c}{m_c} \right)^2 + \left(\frac{\partial x_{c,i}}{x_{c,i}} \right)^2 \right]^{\frac{1}{2}} \times 100 \quad \text{Equation A-1}$$

Where

$\frac{\partial E_i}{E_i} (\%)$ represents the relative uncertainty percentage of extraction efficiency.

∂m_o and ∂m_c represent the error associated with the OHAUS Analytical Plus mass balance, which was 0.0001 g.

m_o represents the actual mass of the fresh sample before the reduction experiment (measured by the table mass balance). A sample value of 1 g was taken for this calculation.

m_c represents the actual mass of the residue after carbonylation (measured by a table mass balance). A sample value of 0.25 g was taken for this calculation.

$\frac{\partial x_{o,i}}{x_{o,i}}$ and $\frac{\partial x_{c,i}}{x_{c,i}}$ represent the relative error in ICP concentration measurement (which is a combination of the error with the sample handling during digestion steps and variation of the ICP instrument). The relative ICP error is 0.0125, or 1.25%.

$$\frac{\partial E_i}{E_i} (\%) = \left[\left(\frac{0.0001 \text{ g}}{1 \text{ g}} \right)^2 + (0.0125)^2 + \left(\frac{0.0001 \text{ g}}{0.25 \text{ g}} \right)^2 + (0.0125)^2 \right]^{\frac{1}{2}} \times 100$$

$$\frac{\partial E_i}{E_i} (\%) = 1.8 \%$$

The relative error in extraction efficiency will be rounded to 2% when presenting ICP extraction results.